Università degli Studi di Padova

Dipartimento di Fisica e Astronomia "G. Galilei"

Master Thesis in Astronomy

Circumstellar Dust Distribution in Systems with Two Planets in Resonance

Supervisor
Prof. Francesco Marzari
Università di Padova

Co-supervisor
Dott. Silvano Desidera
Istituto Nazionale di Astrofisica

Master Candidate
Serena Banfi
1143938

Academic Year 2017/2018

Liquid eternity perpetuates our lives
But will it paralyze our minds?

— Ayreon, "The Human Compulsion"

Abstract

Protoplanetary discs are the fundamental channel to peer into both star formation and planet formation: their study through the combination of theory, observations and numerical simulations is essential to unveil still unanswered questions about their structure and the processes that rule them. ALMA and SPHERE are among the most powerful instrumentation for observations of the cold universe, which open up the opportunity of studying objects like dust discs surrounding young stars. This new generation of imaging has led to major changes in the understanding of protoplanetary discs, which are now acknowledged to have different, complex structures. The mutual interaction between gas, dust, planets and their surroundings leads to deviations from axisymmetric shapes, like gaps, spirals and warps.

In my thesis I investigated via numerical simulations the effects of two giant planets locked in resonance on the dust distribution of the circumstellar disc around a young star, in order to gather if such systems are able to leave peculiar features such as a common gap, which is an essential requirement for outward migration — invoked to explain the observed position of several giant exoplanets with respect to their host star (Walsh et al. 2011). In my work I tested the outcome of the variations of some parameters, i.e. the eccentricity of the planets, the scale height of the disc and the equation of state: in particular, I aimed to show the differences produced by the inclusion of viscous heating and radiative transfer. I used the tridimensional code PLUTO (Mignone et al. 2007) and tested its efficiency in simulating the gaseous and dusty components of the disc. The main results I obtained are that gaps in both gas and dust are more easily formed in a locally isothermal disc with a lower scale height and with planets on eccentric orbits: radiative transfer acts as an obstruction for gap forming and dust accretion.

I dischi protoplanetari sono il tramite fondamentale per lo studio della formazione di stelle e pianeti: combinando teoria, osservazioni e simulazioni numeriche è possibile trarre informazioni sulla loro struttura e i sui processi che li gonvernano. ALMA e SPHERE sono tra gli strumenti più potenti per le osservazioni di oggetti freddi nell'universo, come i dischi di polvere attorno a stelle giovani: questa nuova generazione di acquisizione di immagini ha condotto a grandi cambiamenti nell'interpretazione dei dischi protoplanetari, che ora sappiamo essere caratterizzati da strutture complesse e differenti fra loro. L'interazione reciproca tra gas, polvere, pianeti e i loro dintorni porta alla formazione di strutture come cavità, spirali e distorsioni, che deviano dal profilo assisimmetrico che si attribuiva precedentemente ai dischi.

Nella mia tesi ho effettuato simulazioni numeriche per investigare gli effetti di due pianeti giganti in risonanza sulla distribuzione della polvere di un disco circumstellare attorno a una stella giovane, con lo scopo di capire se sia possibile osservare delle caratteristiche riconoscibili, come una cavità comune, requisito necessario perché avvenga una migrazione verso l'esterno, che permetterebbe di motivare la distanza di alcuni esopianeti giganti dalla loro stella (Walsh et al. 2011). Nel mio lavoro ho analizzato

l'effetto della variazione di alcuni parametri: l'eccentricità dei pianeti, l'altezza di scala del disco e l'equazione di stato. In particolare mi sono occupata di esaminare le differenze dovute all'inserimento del riscaldamento viscoso e del trasporto radiativo. Ho utilizzato il codice tridimensionale PLUTO (Mignone et al. 2007) e ne ho collaudato l'efficienza nel simulare le componenti di gas e polvere nel disco. Il risultato principale che ho ottenuto consiste nel fatto che cavità in gas e polvere si formano più facilmente in dischi localmente isotermi con un'inferiore altezza di scala e con pianeti su orbite eccentriche: il trasporto radiativo risulta un deterrente per la formazione di cavità e per l'accrescimento di polvere sui pianeti.

Contents

1 Introduction

1.1 Protoplanetary Discs

Protoplanetary discs (PPDs) of gas and dust surrounding young stars are the cradle of planet formation. They originate from diffuse gas characterised by high angular momentum and are observed for the first few million years of a star's life. Eventually, PPDs are partially accreted onto the star and partially dissipated on timescales much longer than the orbital or dynamical ones.

Star formation processes in galaxies happen within relatively dense and cool molecular clouds which determine a PPD's initial mass, size and chemical composition. A cloud's inhomogeneity in terms of density and velocity fields due to turbulence (Larson 1981) causes its collapse to introduce nonzero angular momentum.

1.1.1 Structure of Accretion Discs

In most cases the disc flow is confined in the proximity of the orbital plane, so that a series of approximations can be made and we can now refer to them as *thin discs*. If we neglect the disc self-gravity and its internal pressure gradients, matter will move approximately with Keplerian angular velocity

$$\Omega_{\mathrm{K}}(R) = \sqrt{\frac{GM_*}{R^3}} \tag{1.1}$$

and thus circular velocity

$$v_\phi = R\Omega_{\mathrm{K}}(R). \tag{1.2}$$

In addition, the gas is assumed to possess a radial velocity v_R, which has to be negative near the central star to allow accretion. The disc is characterised by its *surface density*

$$\Sigma(R,t) = \int_{-\infty}^{+\infty} \rho(R,t,z)dz \tag{1.3}$$

i.e. the mass per unit surface area of the disc. With regard to the vertical structure, it is considered to be strongly decoupled to the radial structure, so it can be treated separately (Figure 1.1). For an

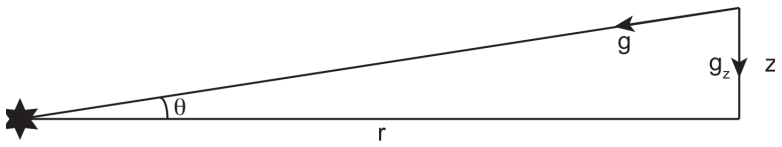

Figure 1.1: Vertical geometry of a PPD in hydrostatic equilibrium: the balancing forces are the vertical component of stellar gravity and the vertical pressure gradient. Credits: Armitage 2015.

isothermal z-structure with $z \ll R$, the hydrostatic equation leads to

$$\rho(R, z) = \rho_{\rm mid}(R)\, e^{-\frac{z^2}{2H^2}} \tag{1.4}$$

where $\rho_{\rm mid}(R)$ is the density on the midplane $z = 0$ and it can be expressed as

$$\rho_{\rm mid}(R) = \frac{1}{\sqrt{2\pi}} \frac{\Sigma}{H} \tag{1.5}$$

with $H = c_s/\Omega_{\rm K}$ being the thickness of the disc, or vertical *scale height*, and c_s the sound speed. For values of the mean molecular weight of a gas of cosmic composition, $\mu \approx 2.3$, the sound speed $c_s = \sqrt{{\rm k_B}T/(\mu m_{\rm H})} \approx 0.6\,{\rm km\,s^{-1}}$ gives an aspect ratio $H/R \approx 0.02$ at 1 AU around a Solar mass star, where the temperature is reasonably around 100 K.

The disc itself also contributes to the vertical component of gravity: approximating the disc as an infinite sheet with constant surface density Σ, according to Gauss' theorem the gravitational acceleration above the sheet is equal to $2\pi G\Sigma$ and dominates on the vertical component of the star's gravity if

$$\frac{M_{\rm disc}}{M_*} > \frac{1}{2}\left(\frac{H}{R}\right). \tag{1.6}$$

1.1.2 Viscosity

To accrete onto the star, gas in the disc must lose angular momentum, thus converting orbital kinetic energy into heat: the mechanism that governs this process is one of the unsolved problems of the physics of accretion discs. Unless the disc experiences the same Ω at each radial distance, the motion takes place through *differential rotation*, like in the case of Keplerian rotation, where adjacent rings of material generate viscous stresses due to chaotic thermal motions or turbulent motions. Thus, momentum is transferred orthogonally with respect to the gas motion (*shear viscosity*). The critical part is to determine the nature and magnitude of the viscosity. We can compare the intensity of inertial and viscous forces via the *Reynolds number* in the case of molecular transport:

$$Re = \frac{R v_\phi}{\lambda \widetilde{v}} \tag{1.7}$$

where λ and $\widetilde{v}$ are respectively the mean free path and the thermal speed of the molecules. For expected values of such quantities in accretion discs $Re_{\rm mol} > 10^{14}$ (Frank 1986), which means molecular viscosity is too weak to be effective as a dissipative force. Furthermore, at such elevated Reynolds numbers, turbulence sets in: hence it is currently believed that these chaotic motions are the source of the viscosity, characterised by spatial scale $\lambda_{\rm turb}$ and velocity of the eddies $v_{\rm turb}$. Assumptions can be made about the magnitude of these quantities: largest turbulent eddies cannot exceed the disc thickness H and the motion is likely subsonic, such that

$$\nu = \alpha c_{\rm s} H. \tag{1.8}$$

We then expect $\alpha \lesssim 1$: this is the so called Shakura & Sunyaev (Shakura and Sunyaev 1973) α-*prescription*.

1.1.2.1 Turbulence

The origin of turbulence in PDDs is still unknown but there are several candidates which could explain the occurrence of turbulent motions. The linear stability of a shear flow against axisymmetric perturbations is given by Rayleigh's criterion (Pringle and King 2007)

$$\frac{{\rm d}l}{{\rm d}R} = \frac{\rm d}{{\rm d}R}(R^2\Omega) > 0 \tag{1.9}$$

i.e. the flow is stable if the specific angular momentum increases with radius, as happens for a Keplerian disc in which $l \propto \sqrt{R}$.

Vertical Shear Instability

Vertical shear instability (VSI) (Nelson et al. 2013) is a so called *entropy-driven* instability, i.e. it relies on the existence of a non-trivial temperature structure. If a disc has a radial temperature gradient, then there is vertical shear (Takeuchi and Lin 2002). To access the free energy in the vertical shear requires vertical fluid displacements, which are strongly dependent on the radiative properties of the disc: under the right conditions, Nelson et al. 2013 and Stoll and Kley 2014 found that VSI can generate an α of a few 10^{-4}.

Self-Gravity

A disc is *self-gravitating* if it is unstable to the growth of surface density perturbations when the gravitational force between different fluid elements cannot be ignored. The Toomre parameter (Toomre 1964) is defined as

$$Q \equiv \frac{c_s \Omega}{\pi G \Sigma} : \tag{1.10}$$

a disc is self-gravitating if $Q < Q_{\rm crit} \sim 1$. For a stationary disc we can write

$$Q = \frac{3\alpha c_s^2}{G\dot{M}}, \tag{1.11}$$

where $\dot{M}$ is the mass accretion rate, so self-gravity is most likely to be important at lower c_s, i.e. at larger distances from the star, where the temperature is lower. The disc mass required for self-gravity is

$$\frac{M_{\rm disc}}{M_*} > \frac{H}{R}. \tag{1.12}$$

The outcomes of self-gravity in a disc can either be spiral overdensities which lead to gravitational torques transporting angular momentum outwards or fragmentation into bound objects due to pressure and tidal forces.

Magneto-Rotational Instability

In PPDs magnetic fields are mostly relevant in the thermally ionized region close to the star. The magneto-rotational instability (MRI) (Balbus and Hawley 1991) is due to cylindrical shear flows that contain a weak magnetic field. The condition for instability is that

$$\frac{\mathrm{d}\Omega^2}{\mathrm{d}R} < 0 \tag{1.13}$$

which is always satisfied in discs. What happens is that a vertical field is slightly perturbed radially, so that it links fluid elements in the disc at different radii: because of the shear in the disc, the fluid closer to the star orbits faster than the fluid further out, creating a toroidal field component. The tension in the magnetic field linking the two elements imparts azimuthal forces to both the inner fluid (opposite to its orbital motion) and the outer fluid (along its orbital motion). The tension force thus reduces the angular momentum of the inner fluid element and increases that of the outer element: the inner fluid then moves further inward and the outer fluid further outward, thus resulting in instability. Simulations show that the MRI saturates to a turbulent state with $\alpha \approx 0.02$.

1.1.3 Evolution of Accretion Discs

The equation governing the time evolution of surface density in a Keplerian disc was obtained by Pringle 1981:

$$\frac{\partial \Sigma}{\partial t} = \frac{3}{R}\frac{\partial}{\partial R}\left[\sqrt{R}\frac{\partial}{\partial R}\left(\nu\Sigma\sqrt{R}\right)\right], \tag{1.14}$$

which is a nonlinear diffusion equation. A simplified model which assumes a constant ν and an initial ring-like matter distribution (Figure 1.2) allows to infer that viscosity has the effect of spreading the

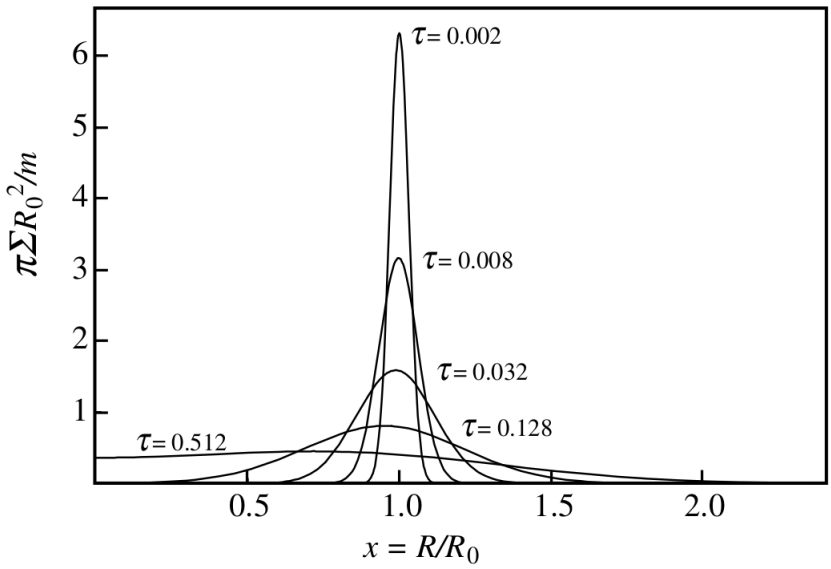

Figure 1.2: A ring of matter of mass m placed in a Keplerian orbit at $R = R_0$ spreads out under the action of viscous torques. The surface density Σ is shown as a function of $x = R/R_0$ and the dimensionless time variable $\tau = 12\nu t R_0^{-2}$ (Credits: Frank 1986).

original ring in radius on a typical viscous timescale

$$t_{\rm visc} \sim \frac{R^2}{\nu}. \tag{1.15}$$

The outer parts of the matter distribution move outwards, taking away the angular momentum of the inner parts, which move towards the accreting star and the radius at which v_R changes sign moves outwards itself:

$$v_R = -3\nu \frac{\partial}{\partial R} \log\left(R^{1/2}\Sigma\right). \tag{1.16}$$

Eventually, most of the original mass has accreted onto the central star and most of the original angular momentum has been carried to very large radii by a very small fraction of the mass.

1.1.4 Emission Spectra of Accretion Discs

1.1.4.1 Stellar Irradiation

A disc whose temperature is determined by stellar irradiation is called *passive* and can be considered as flat disc that absorbs all incoming stellar radiation and re-emits it locally as a blackbody. For a star with

effective temperature T_* and brightness $I_* = \sigma T_*^4/\pi$, where σ is the Stefan-Boltzmann constant,

$$\left(\frac{T_{\rm disc}}{T_*}\right)^4 = \frac{1}{\pi}\left[\arcsin\left(\frac{R_*}{R}\right) - \left(\frac{R_*}{R}\right)\sqrt{1-\left(\frac{R_*}{R}\right)^2}\right], \tag{1.17}$$

which can be approximated as $T_{\rm disc} \propto R^{-3/4}$.

1.1.4.2 Viscous Heating

If we ignore irradiation, the temperature profile of a PPD is dominated by the dissipation of gravitational potential energy associated with accretion. Assuming that the vertical energy transport mechanism is exclusively radiative and that the disc medium can be treated as plane-parallel, the flux of radiant energy through a surface $z = const$ is given by

$$F(z) = -\frac{16\sigma T^3}{3\kappa_{\rm R}\rho}\frac{\partial T}{\partial z} \tag{1.18}$$

where σ is the Stefan-Boltzmann constant and $\kappa_{\rm R}$ is the Rosseland mean opacity, thus assuming that the disc is optically thick in the z-direction. With these assumptions, each element of the disc face radiates as a blackbody with temperature

$$T_{\rm disc} = \left[\frac{3GM\dot{M}}{8\pi R^3\sigma}\left(1-\sqrt{\frac{R_*}{R}}\right)\right]^{1/4} = \left(\frac{9\nu\Sigma GM}{8R^3\sigma}\right)^{1/4} \tag{1.19}$$

where R_* is the stellar radius and $\dot{M}$ is the accretion rate

$$\dot{M} = \frac{3\pi\nu\Sigma}{1-\sqrt{\frac{R_*}{R}}}. \tag{1.20}$$

The specific intensity of each element can be approximated as

$$I_\nu = B_\nu[T(R)] = \frac{2h\nu^3}{c^2}\frac{1}{e^{\frac{h\nu}{KT(R)}}-1} \tag{1.21}$$

i.e. neglecting the atmosphere of the disc. The integral of this quantity gives the actual flux

$$F_\nu = \frac{2\pi\cos i}{D^2}\int_{R_*}^{R_{\rm out}} I_\nu R{\rm d}R, \tag{1.22}$$

where D is the observer's distance whose line of sight makes an angle i to the normal to the disc plane and $R_{\rm out}$ is the outer boundary of the disc. This results in a stretched-out blackbody with a flat $\propto \upsilon^{1/3}$

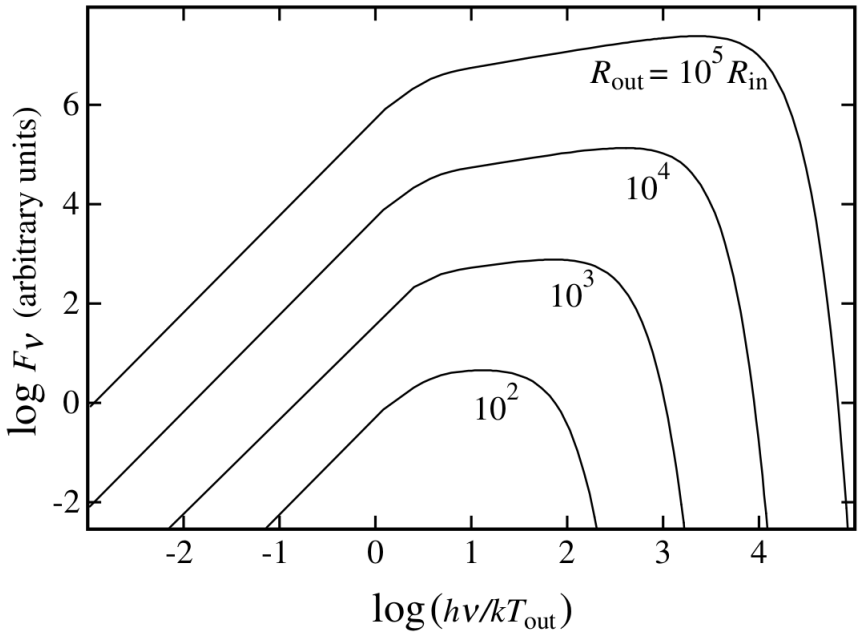

Figure 1.3: The continuum spectrum of a steady optically thick accretion disc radiating locally as a blackbody for discs with different ratios between the outer and inner radius (credits: Frank 1986).

part (Figure 1.3). For optical depths $\tau \gg 1$ the midplane temperature T_c is much larger than the photosphere temperature $T_{\rm disc}$:

$$\frac{T_c^4}{T_{\rm disc}^4} \simeq \frac{3}{4}\tau. \tag{1.23}$$

Usually both stellar irradiation and accretional heating are significant to the thermal balance of the disc. For $\tau \gg 1$:

$$T_c^4 \simeq \frac{3}{4}\tau T_{\rm visc}^4 + T_{\rm irr}^4. \tag{1.24}$$

1.2 Dust

Dust composes about 1% of a PPD and consists of the indispensable solid material needed for the formation of planets and minor bodies around a star. Dust is fundamental for the evolution of a PPD since it dominates the opacity and as a consequence the temperature by absorbing the stellar electromagnetic radiation and re-emitting it in the infrared. Circumstellar dust distribution also allows to obtain insights about the gas dynamics thanks to its dependence to changes in the gas disc. Dust evolves both via transport processes and via collisional processes, which will be analysed below.

1.2.1 Drag Forces

Because of pressure support, the gas is orbiting the star at speeds smaller than the Keplerian velocity: usually this difference is of $50 - 100\ \mathrm{m\,s^{-1}}$. The phenomenon of aerodynamic drag occurs when there is a difference in velocity between an object and the surrounding gas. Let us consider a particle of solid material of radius s and material density ρ_s which moves at a velocity v relative to the local velocity of the gas disc. It is necessary to distinguish between two different regimes based on the relative dimensions of s and the mean free path of gas molecules λ, given by:

$$\lambda = \frac{\mu m_\mathrm{H}}{\sqrt{2}\rho_\mathrm{g}\sigma_\mathrm{mol}} \tag{1.25}$$

where μ is the mean molecular weight, m_H is the proton mass, ρ_g is the gas density and $\sigma_\mathrm{mol} = \pi d_\mathrm{mol}^2$ is the molecular cross section, with d_mol effective molecular diameter, of the order of a few Å.

Epstein drag

If $s \lesssim \lambda$, the fluid on the scale of the particle is collisionless and its velocity distribution is Maxwellian with mean thermal speed

$$v_\mathrm{th} = \sqrt{\frac{8\mathrm{k_B}T}{\pi\mu m_\mathrm{H}}} \tag{1.26}$$

where $\mathrm{k_B}$ is the Boltzmann constant. The drag effect is due to the different frequency at which each dust particle is hit by a gas molecule from the 'front' or the 'back' side. The resulting net drag force is (Weidenschilling 1977)

$$\mathrm{F_{Ep}} = -\frac{4\pi}{3}\rho_\mathrm{g} s^2 v_\mathrm{th}\mathbf{v} \tag{1.27}$$

where ρ_g is the gas density. The key parameter describing the aerodynamic coupling between dust and gas is the *stopping time*:

$$t_\mathrm{stop} = \frac{mv}{F_\mathrm{Ep}} = \frac{\rho_\mathrm{s} s}{\rho_\mathrm{g} v_\mathrm{th}}, \tag{1.28}$$

or the *Stokes number*:

$$\mathrm{St} = t_\mathrm{stop}\Omega_\mathrm{K}. \tag{1.29}$$

Particles with the same Stokes number have the same aerodynamic behaviour. For a vertically isothermal gas disc with scale height $H = c_\mathrm{s}/\Omega_\mathrm{K}$ and gas surface density Σ_g, the Stokes number on the midplane is equal to (Birnstiel et al. 2009)

$$\mathrm{St} = \frac{\mathrm{s}\rho_\mathrm{s}}{\Sigma_\mathrm{g}}\frac{\pi}{2}, \tag{1.30}$$

assuming a gas midplane density of $\rho_\mathrm{g,mid} = \frac{\Sigma_\mathrm{g}}{\sqrt{2\pi}H_\mathrm{g}}$. Therefore the Stokes number is linearly dependent on the particle size: a small particle adapts to the gas velocity below an orbital timescale, while

for a bigger particle it may take several orbits.

Stokes drag

If $s \gtrsim \lambda$, the drag force scales with the ram pressure experienced by the particle:

$$\mathrm{F_D} = -\frac{C_\mathrm{D}}{2}\pi s^2 \rho_\mathrm{g} v \mathrm{v} \tag{1.31}$$

where C_D is the *drag coefficient* and depends on the shape of the particle and on the fluid's Reynolds number.

1.2.1.1 Dust Drift

Dust particles embedded in a gaseous disc migrate towards the star as a consequence of aerodynamic drag. Large bodies with $\mathrm{St} \gg 1$ have speeds close to the Keplerian one and experience gas drag as a 'headwind' by the sub-Keplerian disc. This leads to a change in the orbital energy $-GM_*m/2a$, with a radius of the orbit, of a quantity given by the work of the drag force

$$\dot{E} \simeq -|\mathbf{F}| v_\mathrm{K}, \tag{1.32}$$

which gives a radial velocity equal to

$$v_r = -\frac{2}{\mathrm{St}} v. \tag{1.33}$$

Bodies with $\mathrm{St} \ll 1$ are forced to orbit at the gas speed instead since they are strongly coupled to the gas: particles do not feel the pressure gradient, so their non-Keplerian orbital motion results in a net radial force

$$\frac{F_r}{m} = \frac{(v_\mathrm{K} - v)^2}{a} - \frac{GM_*}{a^2}, \tag{1.34}$$

which gives a radial velocity equal to

$$v_r = -2\mathrm{St} v. \tag{1.35}$$

To understand the regime of intermediate-sized particles we must consider the evolution of the velocities of dust and gas (Nakagawa et al. 1986)

$$\frac{\mathrm{d}\mathrm{u_d}}{\mathrm{d}t} = -\frac{1}{t_\mathrm{stop}}(\mathrm{u_d} - \mathrm{u_g}) - \frac{GM_*}{r^3}\mathrm{r} \tag{1.36}$$

$$\frac{\mathrm{d}\mathrm{u_g}}{\mathrm{d}t} = -\frac{\epsilon}{t_\mathrm{stop}}(\mathrm{u_g} - \mathrm{u_d}) - \frac{GM_*}{r^3}\mathrm{r} - \frac{\nabla P}{\rho_\mathrm{g}} \tag{1.37}$$

with $\epsilon = \rho_\mathrm{d}/\rho_\mathrm{g}$ and P gas pressure. Solving for the first deviation from the Keplerian velocity ($\mathrm{v} =$

$u - v_K$) in cylidrical coordinates leads to the dust drift speed

$$v_r \simeq -\frac{2}{\mathrm{St} + \mathrm{St}^{-1}} \eta v_K \tag{1.38}$$

$$v_\phi \simeq -\frac{1}{1 + \mathrm{St}^2} \eta v_K, \tag{1.39}$$

where

$$\eta = -\frac{1}{2} \left(\frac{H}{r} \right)^2 \frac{\partial \log P}{\partial \log r} \tag{1.40}$$

describes the factor by which the orbital gas velocity is smaller than the Keplerian one, i.e. $v_{\phi,g} = \eta v_K$. This holds as long as a low dust-to-gas ratio in assumed, i.e. there is no back reaction of the dust on the gas velocity. The consequences are that:

- particles with a Stokes number < 1 drift inward with a speed of $v_r \simeq -2\mathrm{St}\eta v_K$: small particles move slowly, larger particles move faster;
- for a typical disc η is of the order of a few per mille, which means the orbit of a dust particle decays on a timescale of a few hundred orbits;
- the drift speed of particles with $\mathrm{St} > 1$ tends to zero, so they move on Keplerian orbits;
- the direction of the radial drift is towards higher pressure, which means inwards in a disc denser and hotter closer to the star.

In addition to the drift motion, dust is also carried along with the radial gas flow as long as $\mathrm{St} < 1$ (Takeuchi and Lin 2002)

$$u_{r,\mathrm{dust}} = \frac{1}{1 + \mathrm{St}^2} u_{r,\mathrm{gas}}. \tag{1.41}$$

Solids that experience significant radial drift tend to pile up closer to the star: this concentration in the inner disc translates into a varying ratio between dust and gas surface densities as a function of radius. Assuming the surface density of solids has reached a steady state:

$$\frac{\Sigma_d}{\Sigma_g} \propto \left(\frac{H}{R} \right)^{-2} R^{-1/2}. \tag{1.42}$$

This trend can be more realistically estimated by considering the flaring [*] of the disc. Figure 1.4 shows the mechanism of radial drift and the dependence of the drift timescale on the Stokes number.

[*] a disc is described as *flared* if the ratio H/R is an increasing function of radius

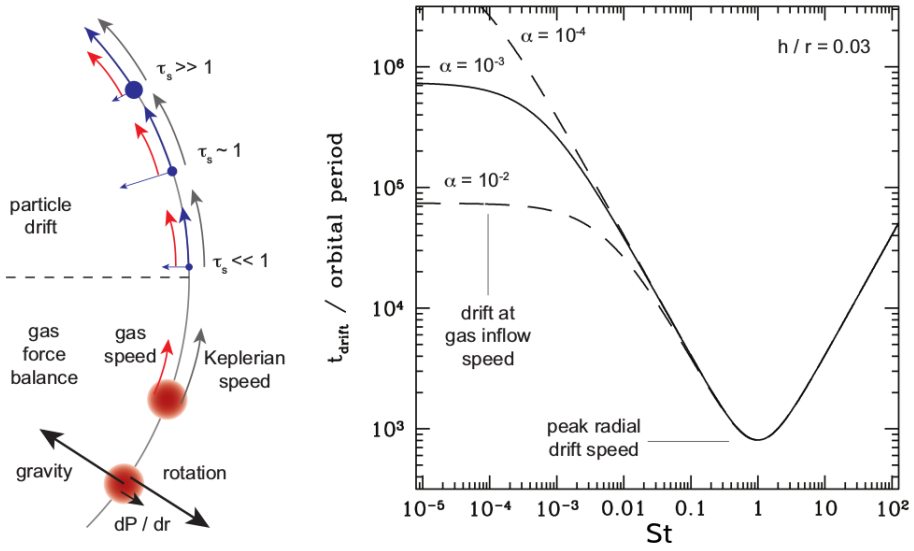

Figure 1.4: *Left*: particles drift inwards in a disc due to the imbalance between the radial forces. *Right*: the radial drift timescale is plotted in units of the local orbital period as a function of the Stokes number. The fastest drift occurs for $\mathrm{St} = 1$. The values are referred to a disc with $H/R = 0.03$. Credits: Armitage 2015.

1.2.2 Dust Growth

Dust grains need to grow several orders of magnitude from sub-micrometer to > km sizes, and they can eventually be called planetesimals, which are gravitationally bound. The collisional timescale for two particles with relative velocity Δv_{ij} is

$$\tau_{\mathrm{col}} = \frac{l}{\Delta v_{ij}} = \frac{1}{n_j \sigma_{ij} \Delta v_{ij}} \tag{1.43}$$

where l is the mean free path of a particle i, n_j is the number density of particles j and σ_{ij} is the cross section of particles i and j. Then the rate of collision between particles i and j, potentially forming a new species k, is

$$R_{ij} = n_i n_j \sigma_{ij} \Delta v_{ij}. \tag{1.44}$$

For example, for a process of pure sticking, $m_k = m_i + m_j$:

$$\dot{n}_k = \frac{1}{2} \sum_{i,j} R_{i,j} \delta_{i,j-k} - \sum_i R_{i,k}. \tag{1.45}$$

Collisional outcomes depend on impact velocities, dimensions of grains and compositional properties of grains, such as porosity and chemical composition. Possible outcomes are (Birnstiel et al. 2016):

- *sticking*: hit-and-stick collisions

- *bouncing*: particles bounce off each other without changing their mass
- *erosion*: a smaller projectile removes mass from a larger target
- *mass transfer*: a smaller projectile fragments upon collision with a target and deposits some fraction of its mass
- *fragmentation*: one or both particles are completely destroyed.

1.2.2.1 Streaming Instability

Figure 1.5 shows that collisions are unlikely to result in coagulation over a wide rage of sizes, from mm to km, since available binding energies (chemical or gravitational) are negligible comparable to kinetic energies (Chokshi et al. 1993, Youdin and Shu 2002), thus some alternative planetesimal formation scenarios have been suggested. Safronov and Zvjagina 1969, Goldreich and Ward 1973 proposed that in a laminar disc planetesimal formation can derive from gravitational instability of the dust as it settles towards the disc midplane: the dust would flatten in a thin layer until it gravitationally collapses and planetesimals are formed. Weidenschilling 1980 showed that this would cause the generation of turbulence due to Kelvin-Helmholtz instability, which would prevent dust overdensities needed for gravitational instability to occur. However, if the relative densities between gas and dust are similar, dust will exert a feedback on the gas (Youdin and Goodman 2005), that would translate into a *streaming instability* (Johansen et al. 2007) caused by drag effects, which could explain the formation of planetesimals from smaller solids with $\mathrm{St} \sim 1$ that concentrate into clumps which can gravitationally collapse. The streaming instability depends on the particle stopping time, the local solid-to-gas ratio, or metallicity Z, and the magnitude of the deviation from Keplerian velocity $\eta v_\mathrm{K}/c_s$. Using two-dimensional simulations Carrera et al. 2017, Yang et al. 2016 found that strong clumping occurs for $Z > Z_\mathrm{crit}$:

$$\begin{cases} Z_\mathrm{crit} = 0.10(\log \mathrm{St})^2 + 0.20 \log \mathrm{St} - 1.76 \ \text{ if } \ \mathrm{St} < 0.1 \\ Z_\mathrm{crit} = 0.30(\log \mathrm{St})^2 + 0.59 \log \mathrm{St} - 1.57 \ \text{ if } \ \mathrm{St} > 0.1. \end{cases} \tag{1.46}$$

1.2.3 Structure of Dust Discs

1.2.3.1 Vertical Structure

Particles sediment towards the midplane due to the vertical component of the star's gravitational force $|\mathbf{F}_\mathrm{grav}| = m\Omega_\mathrm{K}^2 z$ that cannot be counterbalanced by pressure gradients, as happens for the gas component. Thus particles move towards the midplane until the drag force balances gravity in the vertical direction and the settling time can be obtained as

$$t_\mathrm{sett} = \frac{z}{v_\mathrm{sett}} = (\Omega_\mathrm{K}\mathrm{St})^{-1}. \tag{1.47}$$

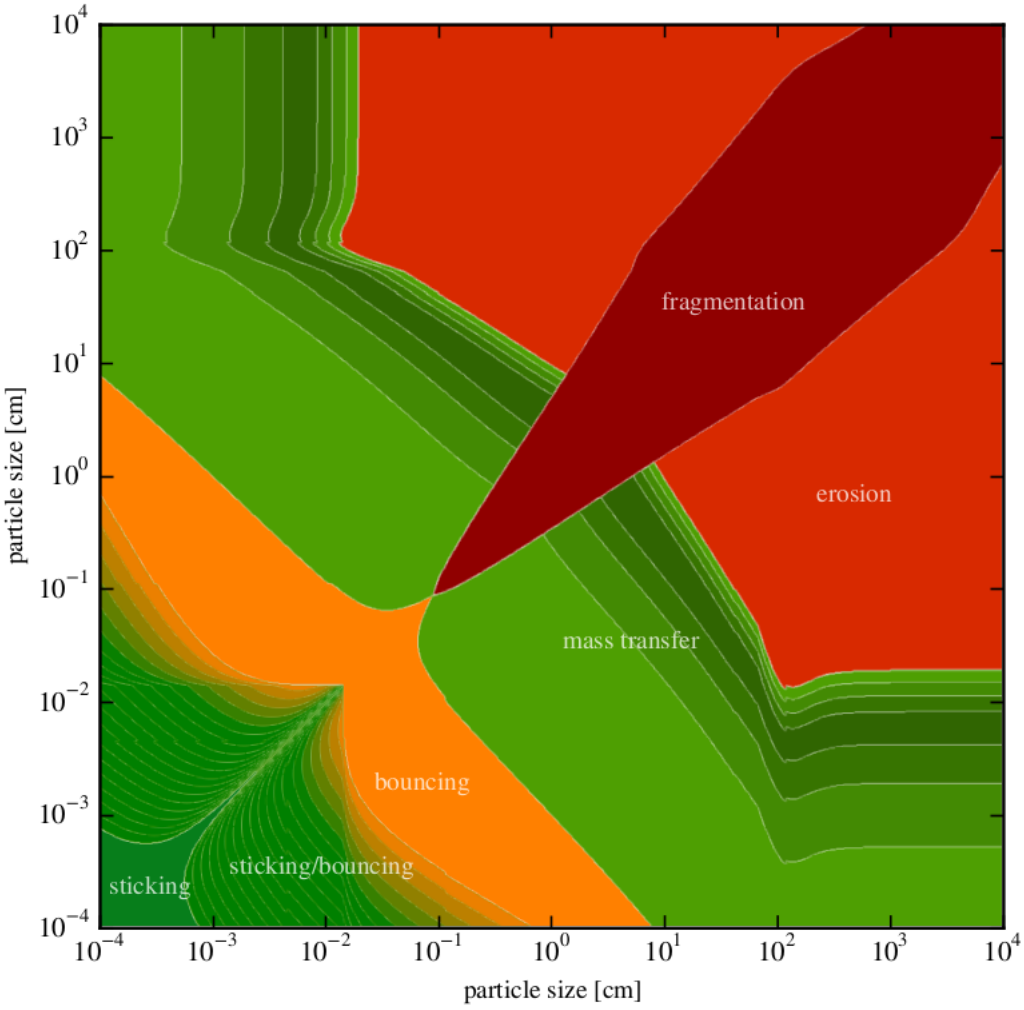

Figure 1.5: Collisional outcomes for silicate grains from Windmark et al. 2012. *Green* regions denote growth of the larger collision partner, *red* mass loss and *orange* mass-neutral bouncing collisions.

For large z this is usually a short timescale since the low density of the disc atmosphere implies a large Stokes number for most grain sizes: for a 1 μm particle at $z \sim H$ at 1 AU, reasonable assumptions give a settling time of about 10^5 years. If the particles do not grow, their Stokes number tends to decrease while approaching higher densities, thus slowing down their motion. On the other hand, if the particles constructively collide and grow in size, their Stokes number manages to stay large enough to allow them to keep settling towards the midplane, so they can continue to increase their dimensions up to macroscopic sizes.

1.2.3.2 Turbulent Mixing

Since it is believed that the gas experiences turbulent viscosity, it must also affect the dust motion. The random motion induced by the turbulence acts as a diffusivity on the dust and varies with the grain size. The ratio of the dust diffusivity to the gas diffusivity — the latter being usually assumed to be equal to the gas viscosity ν — is the *Schmidt number* (Youdin and Lithwick 2007)

$$\mathrm{Sc} = \frac{D_\mathrm{g}}{D_\mathrm{d}} \simeq 1 + \mathrm{St}^2. \tag{1.48}$$

The main effects of turbulent mixing are preventing the settling process of solid particles into a thin layer on the midplane and smoothing of concentrations of dust grains. In order to evaluate whether turbulence is able to counteract the vertical settling, we must compare the settling time to the turbulence timescale $t_\mathrm{diff} = z^2/D_\mathrm{d}$, where D_d is the turbulent diffusion coefficient of the particles. It is useful to define the *Péclet number*:

$$\mathrm{Pe} = \frac{t_\mathrm{diff}}{t_\mathrm{sett}} = \frac{\mathrm{St}}{\alpha}\left(\frac{z}{H_\mathrm{g}}\right)^2 \tag{1.49}$$

where H_g is the gas scale height. For $\mathrm{Pe} > 1$ the settling timescales are shorter than the diffusion timescales; approaching the midplane, $\mathrm{Pe} < 1$ and diffusion is dominating, so we can expect the vertical dust-to-gas ratio to drop significantly within a dust scale height given by

$$H_\mathrm{d} = H_\mathrm{g}\sqrt{\frac{\alpha}{\mathrm{St}+\alpha}}. \tag{1.50}$$

After a few settling timescales, the system reaches an equilibrium between the sedimentation and the diffusion fluxes: the dust density distribution can be calculated as

$$\rho_\mathrm{d}(z) = \rho_\mathrm{d,mid}(z)\exp\left\{-\frac{\mathrm{St}_\mathrm{mid}}{\alpha}\left[\exp\left(\frac{z^2}{2H_\mathrm{g}^2}\right)-1\right]-\frac{z^2}{2H_\mathrm{g}^2}\right\}. \tag{1.51}$$

1.2.3.3 Radial Structure

The mechanisms that need to be considered are dust drift, turbulent mixing and radial flow of the gas which transports dust particles. By comparing the timescales of growth and local drift, it is possible to define the drift size limit (Birnstiel et al. 2012) as

$$a_{\rm drift} \simeq 0.35 \frac{\Sigma_d}{\rho_s} \left| \frac{{\rm d}\log r}{{\rm d}\log P} \right| \left(\frac{H_g}{r} \right)^{-2}. \tag{1.52}$$

Particles below this curve will grow faster than they drift and vice versa. We must also consider that above a certain size particles increase their relative velocities and more easily fragment:

$$a_{\rm frag} \simeq 0.08 \frac{\Sigma_g}{\rho_s \alpha} \left(\frac{v_{\rm frag}}{c_{\rm s}} \right)^2. \tag{1.53}$$

Birnstiel et al. 2012 found that fragmentation dominates in the inner regions of the disc, while in regions with low dust-to-gas ratio radial drift has more relevant effects. This allows to derive the maximum particle size as a function of distance to the star. It is generally valid to assume that the whole mass of the dust component is contained in the largest grains, whose transport therefore dominates the mass flux. The dust mass accretion rate is

$$\dot{M}_{\rm d} = 2\pi r \Sigma_{\rm d} v(r) = const, \tag{1.54}$$

from which the dust density profile can be obtained. Depending on the maximum particle size present in each area of the disc, the profile can be expressed as a combination power-laws. For typical assumptions ($\Sigma_{\rm g} \propto r^{-1}$) this gives $\Sigma_{\rm d} \propto r^{-0.75}$ in the outer zones of the disc and $\Sigma_{\rm d} \propto r^{-1.5}$ in the inner zones where fragmentation dominates.

1.2.4 Opacity

Dust is the main opacity source in PPDs except for the innermost regions, where the high temperatures ($T \simeq 1500$ K) account for the destruction of dust particles and only molecular opacity is left. The cross section of a single dust grain to radiation of a certain wavelength depends on the particle size, structure and composition. The main dust constituents include amorphous pyroxene ($[{\rm Fe},\ {\rm Mg}]{\rm SiO_3}$), olivine ($[{\rm Fe},\ {\rm Mg}]_2{\rm SiO_4}$), volatile and refractory organics (CHON), amorphous water ice, troilite (FeS) and iron. Dust aggregates are usually of two kinds: *particle-cluster aggregation*, which are sphere-like particles with a compact core and a rarefied mantle, and *cluster-cluster aggregation*, which are filamentary grains. However, these can be modified by the evolution of the disc through chemical and physical processes. The total opacity κ_ν is therefore related to the chemical composition of the disc and the size distribution of the particles. As previously seen, the radiation

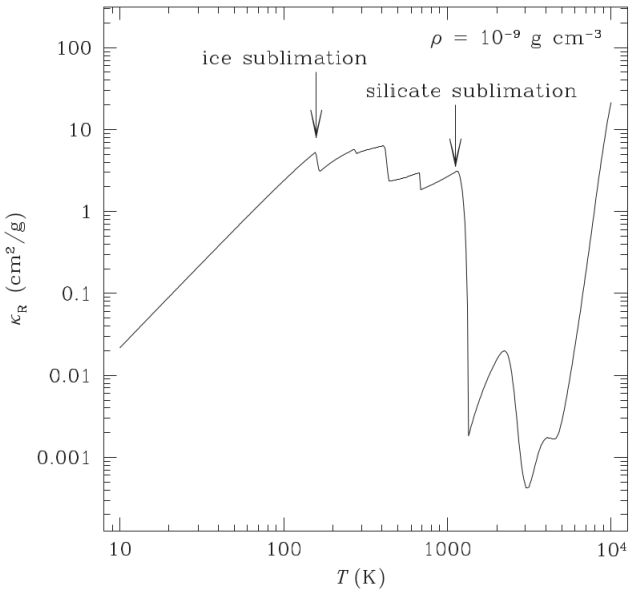

Figure 1.6: The Rosseland mean opacity for dusty gas in PPDs calculated by Semenov et al. 2003 for a gas density of 10^{-9} g cm^{-3}, assuming that the dust is composed of homogeneous spherical particles whose size distribution follows a modified Mathis et al. 1977 law. Credits: Armitage 2009.

field can be considered as a blackbody, hence the Rosseland mean opacity is:

$$\kappa_{\mathrm{R}} = \left(\frac{\int_0^{+\infty} \frac{1}{\kappa_\nu} \frac{\partial B_\nu}{\partial T} \mathrm{d}\nu}{\int_0^{+\infty} \frac{\partial B_\nu}{\partial T} \mathrm{d}\nu} \right)^{-1}, \tag{1.55}$$

where B_ν is the Planck function.

In the coldest regions beyond the snowline ($T \lesssim 150$ K) water ice and volatile organic materials dominate and the Rosseland mean opacity rises as T^2 towards smaller radii, where different kinds of materials gradually evaporate: first water ice, then organics, troilite, iron and silicates. Approaching the centre, opacity grows due to H^- scattering so bound-free and free-free absorption dominates, until electron scattering sets in (Figure 1.6).

1.3 Observations of PPDs

Discs around stars are rare to observe, since they last about $10^{-3} - 10^{-4}$ times the lifetime of a main sequence star. Most of these can be found in star forming regions, such as Orion, about 400 pc away from the Sun: assuming dimensions of the order of the Solar System, $\sim 10^2$AU, spatially resolved imaging of such objects requires sub-arcsecond resolution.

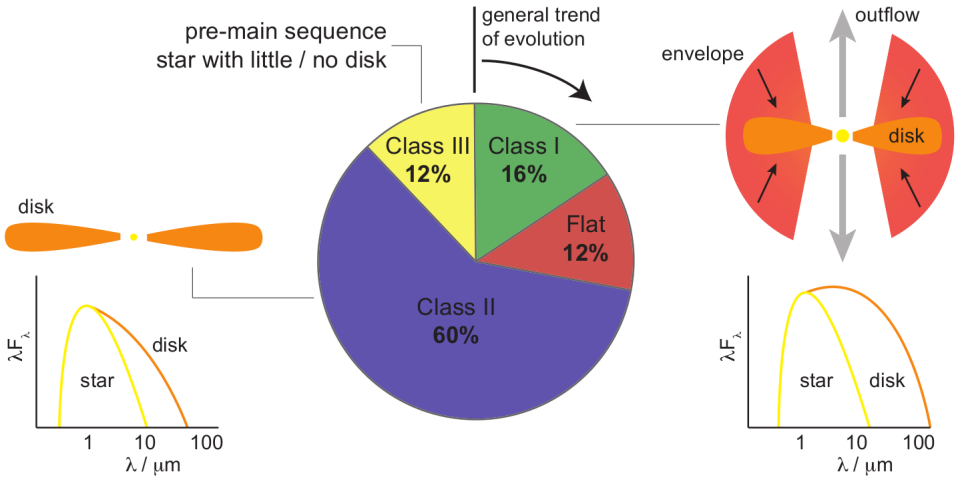

Figure 1.7: The figure shows the statistics from the *Spitzer* c2d Legacy survey for the fraction of sources falling into each class of YSO, which represent an evolutionary sequence. Credits: Armitage 2015.

1.3.1 Young Stellar Objects

The spectrum of a *young stellar object* (YSO) allows to infer the presence of dust in the vicinity of the star by showing more emission in the infrared (IR) than would be expected from a pre-main-sequence star's photosphere. In order to perform a classification of YSOs it is useful to define the slope of the *spectral energy distribution* (SED) between near-IR and mid-IR wavelengths (Armitage 2015)

$$\alpha_{\mathrm{IR}} \equiv \frac{\mathrm{d}\log \nu F_\nu}{\mathrm{d}\log \nu}. \tag{1.56}$$

Based on this parameter, different classes of YSOs are identified:

- *Class 0*: heavily obscured sources with no optical or near-IR emission
- *Class 1*: $\alpha_{\mathrm{IR}} > 0.3$, which corresponds to discs being fed by gas falling in from envelopes of the molecular cloud
- *Flat spectrum sources*: $-0.3 < \alpha_{\mathrm{IR}} < 0.3$
- *Class 2* or *T-Tauri*: $-1.6 < \alpha_{\mathrm{IR}} < -0.3$, which corresponds to pre-main-sequence stars with surrounding discs
- *Class 3*: $\alpha_{\mathrm{IR}} < -1.6$, which corresponds to pre-main-sequence stars with little or no primordial gas remaining.

Figure 1.7 shows graphic reproductions of the different classes and the appearance of their spectra.

1.3.2 Dust Content

1.3.2.1 SED

At disc temperatures $T < 1500$ K the opacity in PPDs is dominated by the contribution from dust composed of rocky or icy grains. Dust is a reliable indicator of the temperature distribution, the disc mass and the size of dust particles. For example, assuming a gas surface density distribution $\Sigma \propto R^{-p}$ and a dust temperature distribution $T_{\rm d} \propto R^{-q}$, with a frequency dependent opacity $\kappa_\nu = \kappa_0 \nu^\beta$, the optical depth through the disc is $\tau_\nu = \Sigma \kappa_\nu$. For a face-on disc the radiative transfer equation allows to estimate the flux density

$$F_\nu = \frac{1}{D^2} \int_{R_{\rm in}}^{R_{\rm out}} B_\nu(T_{\rm d})(1 - e^{-\tau_\nu}) 2\pi R {\rm d}R \tag{1.57}$$

with D distance to the source, $R_{\rm in}$ and $R_{\rm out}$ inner and outer radii of the disc and B_ν Planck function. At wavelengths where the disc is optically thick, $\tau_\nu \gg 1$, i.e. near- and mid-IR, the previous equation, assuming $e^{-\tau_\nu} = 0$, gives

$$\nu F_\nu \propto \nu^{4-2/q} \tag{1.58}$$

which provides a constraint on the radial variation of the dust temperature.

In the mm/sub-mm region of the spectrum most of the emission comes from optically thin regions of the disc, since the bulk of dust particles are smaller. The information obtained from this range of wavelengths can be used as a proxy for the total amount of material in discs because it allows to probe the dust content at lower temperatures. The radiative transfer equation, setting $1 - e^{-\tau_\nu} \approx \tau_\nu$, gives

$$F_\nu = \frac{B_\nu(\overline{T}_{\rm d})\kappa_\nu}{D^2} \int_{R_{\rm in}}^{R_{\rm out}} 2\pi R \Sigma {\rm d}R, \tag{1.59}$$

where $\overline{T}_{\rm d}$ is the weighted average of the temperature of the emitting material. The quantity identified by the integral is the disc mass, that can be inferred once the distance, the opacity and the disc temperature are known. The Rayleigh-Jeans approximation leads to

$$\nu F_\nu \propto \nu^{\beta+3} \tag{1.60}$$

and thus allows to determine the frequency dependence of the opacity.

1.3.2.2 Resolved Imaging

Direct imaging of PPDs shows a multitude of structures which may be the imprint of planet formation, presence of a binary, disc dissipation and instabilities. Resolved images of dust may be obtained by observation of different wavelength ranges: dust emits light as a blackbody in the mm/sub-mm and reflects optical and near-IR light from the star. Images taken at different wavelengths probe a variety of dust components and therefore may show different shapes of the disc, like gaps, holes and spiral density waves. The scattered light images probe the disc surface which directly receives the star

light, so it is dominated by small grains that have not yet settled on the midplane. This technique relies on the fact that scattered light has a recognisable polarisation as opposed to the light coming from the central star. The spatial and wavelength dependence of the intensity distribution allows to derive information about the surface density distribution of the gas disc and about the size distribution of the grains and their albedo.

ALMA and SPHERE

ALMA and SPHERE are the most promising instruments for the study of planet formation via resolved imaging of PPDs. ALMA (Atacama Large Millimeter/ submillimeter Array) is a ground-based facility for observations in the millimitre/submillimitre regime composed of an array of fifty $12\,\mathrm{m}$ antennas on a baseline up to $16\,\mathrm{km}$. This instrument allows to study the coldest matter in the universe like dust: its main achievements include imaging of PPDs like HL Tau, which represents a new starting point for planetary science (ALMA Partnership 2015).
SPHERE (Spectro-Polarimetric High-contrast Exoplanet REsearch) is an adaptive optics system at the VLT (Very Large Telescope array) capable of performing imaging and low-resolution spectroscopy of extra-solar planetary systems at optical and near-IR wavelengths.

Polarimetric differential imaging with SPHERE is sensitive to micron-sized dust grains at the disc surface, which are usually very well coupled to the gas, while ALMA observations probe mm/sub-mm wavelengths: images with comparable angular resolution can potentially reveal the different morphologies of different disc components (Figure 1.8), since many disc processes are expected to differentiate the distribution of different grain sizes.

1.3.3 Gas Content

Spectra of PPDs revealed the presence of several molecules and molecular ions that show lines in the mm/sub-mm range, such as carbon monoxide (CO) (and its isotopologues[†] ^{13}CO and $C^{18}O$), carbon monosulfide (CS), hydrogen cyanide (HCN) and diazenylium (N_2H^+) (Semenov et al. 2018). The bulk of the mass of a PPD is observationally inaccessible since H_2 does not produce rotational or vibrational lines in dipole approximation. Therefore CO is the most used molecule to estimate gas masses, by observationally constraining processes such as photo-dissociation and freezing of gaseous CO (Qi et al. 2015). Molecular line observations also provide a wealth of kinematic information, like the measurement of the rotation profile of the disc gas and thus the central star mass. Thermal and turbulent broadening of a line profile may provide important information about the disc viscosity.

[†]molecules that differ only in their isotopic composition: the isotopologue of a chemical species has at least one atom with a different number of neutrons than the parent

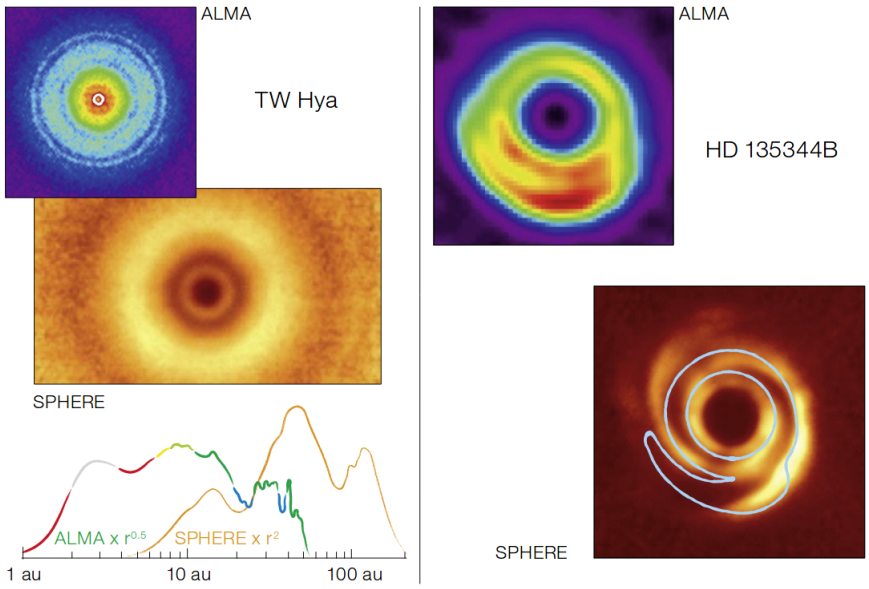

Figure 1.8: Comparison of ALMA and SPHERE images for two discs shown at the same spatial scale. For TW Hya, the ALMA image is from Andrews et al. 2016 and the SPHERE image and radial profiles from Van Boekel et al. 2017. For HD 135344B, the ALMA image is from Van der Marel et al. 2016 and the SPHERE image is from Stolker et al. 2016. Credits: Garufi et al. 2017.

1.4 Orbital Dynamics

1.4.1 Two-Body Problem

The two-body problem is an integrable problem that studies the interaction of two point masses subject to mutual gravitational attraction according to Newton's universal law of gravitation, for example the motion of a single planet around a star. If m_0 and m_1 are the two masses with position vectors r_0 and r_1, $\mathrm{r} = \mathrm{r}_1 - \mathrm{r}_0$ indicates the relative position of m_1 with respect to m_0. The forces experienced by the two masses are

$$\mathrm{F}_0 = G\frac{m_0 m_1}{r^3}\mathrm{r} = m_0\ddot{\mathrm{r}}_0 \text{ and } \mathrm{F}_1 = -G\frac{m_0 m_1}{r^3}\mathrm{r} = m_1\ddot{\mathrm{r}}_1 \tag{1.61}$$

so:

$$m_0\ddot{\mathrm{r}}_0 + m_1\ddot{\mathrm{r}}_1 = 0. \tag{1.62}$$

We can write the *equation of relative motion*

$$\frac{\mathrm{d}^2\mathrm{r}}{\mathrm{d}t^2} + \mu\frac{\mathrm{r}}{r^3} = 0 \tag{1.63}$$

where $\mu = G(m_0 + m_1)$. A constant of motion can be found by taking the vector product and

integrating:

$$\mathrm{r} \wedge \dot{\mathrm{r}} = \mathrm{h} \tag{1.64}$$

which is referred as the *angular momentum integral*. Since r and ṙ lie on the same plane, we can use a polar coordinate system in the *orbit plane* and obtain a scalar equation for the relative motion:

$$\ddot{r} - r\dot{\theta}^2 = -\frac{\mu}{r^2} \tag{1.65}$$

which gives

$$r = \frac{p}{1 + e\cos(\theta - \varpi)} \tag{1.66}$$

with e *eccentricity*, ϖ *longitude of pericentre* and $p = h^2/\mu$. For the case considered, assuming that a is the *semi-major axis*, $e = 0$ and $p = a$ for a circle, while $0 < e < 1$ and $p = a(1 - e^2)$ for an ellipse. In the latter case the semi-major axis and eccentricity are related by:

$$b^2 = a^2(1 - e^2) \tag{1.67}$$

where b is the *semi-minor axis* of the ellipse. It is usually more useful to work with the *true anomaly* $f = \theta - \varpi$. Therefore for an ellipse:

$$r = \frac{a(1 - e^2)}{1 + e\cos f}. \tag{1.68}$$

If T is the orbital period, we can define the average angular velocity as

$$n = \frac{2\pi}{T} \tag{1.69}$$

also called *mean motion*. We can write $\mu = n^2a^3$ and $h = \sqrt{\mu a(1 - e^2)}$.

We can also define an angle which is both 2π-periodic and a linear function of the time: that is the *mean anomaly*

$$M = n(t - \tau) \tag{1.70}$$

where τ is the time of pericentre passage. M has no actual geometrical equivalent, but can be related to an angle that does, the *eccentric anomaly* E, i.e. the angle between the major axis of the ellipse and the radius from the centre of the intersection point on the circumscribed circle. With some algebra we obtain *Kepler's equation*

$$M = E - e\sin E \tag{1.71}$$

whose solution is fundamental to establish the orbital position of a body at a given time. Another parameter that can be introduced is the *mean longitude* $\lambda = M + \varpi$. If we want to treat the general case of an orbit in three dimensions, we need to consider the *inclination* I of the orbital plane, which intersects the reference plane in the *line of nodes*: this allows to define the *ascending node* (point where

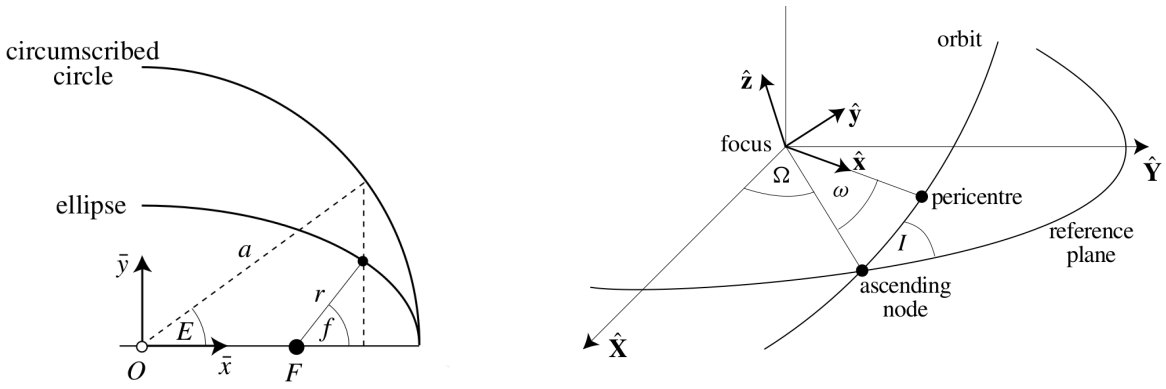

Figure 1.9: *Left*: relation between the true anomaly f and the eccentric anomaly E. *Right*: orbital motion with respect to the reference plane in three-dimensional space. Credits: Murray and Dermott 2000.

the orbit crosses the reference plane moving 'upwards'), the *longitude of the node* Ω (angle between the reference line and the radius vector to the ascending node) and the *argument of the pericentre* ω (angle between this same radius vector and the pericentre of the orbit). We now have defined the full set of *orbital elements*: $a, e, I, \Omega, \omega, f$ (Figure 1.9).

1.4.2 Restricted Three-Body Problem

A special case of the three-body problem is the configuration in which an infinitesimally small particle moves in a plane under the influence of the gravitational attraction of two finite particles of masses $m_1 > m_2$ that revolve around each other in a circular orbit with mean motion n. In the case of interest for my thesis, the most massive body is a star, the secondary body is a planet and the massless body is a dust particle. A proper derivation of the equations of motion can be found in Murray and Dermott 2000, where the unit of mass are chosen such that $\mu = G(m_1 + m_2) = 1$, $\mu_1 = Gm_1 = 1 - m_2/(m_1 + m_2)$ and $\mu_2 = Gm_2 = m_2/(m_1 + m_2)$. Considering the rotating coordinate system referred to the centre of mass, where the x axis is chosen such that the two masses always lie along it with coordinates $(x_1, y_1, z_1) = (-\mu_2, 0, 0)$ and $(x_2, y_2, z_2) = (\mu_1, 0, 0)$, the potential (Figure 1.10) can be expressed as

$$U = \frac{n^2}{2}(x^2 + y^2) + \frac{\mu_1}{r_1} + \frac{\mu_2}{r_2} \tag{1.72}$$

where the term in $x^2 + y^2$ is the centrifugal potential and the term in $1/r_1$ and $1/r_2$ is the gravitational potential.

The only conserved quantity for the circular restricted three-body problem is the *Jacobi constant* defined as

$$C_J = 2U - v^2 \tag{1.73}$$

with $v^2 = \dot{x}^2 + \dot{y}^2 + \dot{z}^2$ square of the velocity of the particle in the rotating frame. It is possible to

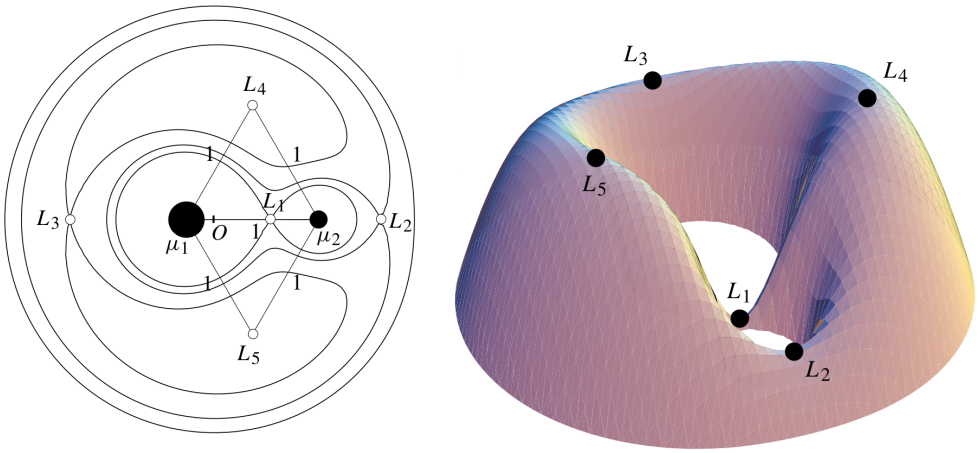

Figure 1.10: *Left*: location of the Lagrangian equilibrium points and associated zero-velocity curves. *Right*: Three-dimensional surface defined by $C_J = 2U$ and location of the Lagrangian equilibrium points. Credits: Murray and Dermott 2000.

construct curves in the plane on which the velocity vanishes: if a *zero-velocity curve* is closed, then the particle cannot escape from inside the curve, unless an external force operates. The equilibrium points of the potential are represented in Figure 1.10: these are the points where the particle has zero velocity and zero acceleration in the rotating frame, also known as *Lagrangian points*. The solutions of the equations for perturbed motion around L_4 and L_5 in the vicinity of these points are represented by *tadpole orbits*; if we increase the initial radial separation from these equilibria, the particle will follow *horseshoe orbits* (Figure 1.11). It is possible to define an area surrounding the secondary mass, called *Hill sphere*, with an approximately circular shape above which L_1 and L_2 lie (Figure 1.11). Bodies in the proximity of the secondary mass are under the influence of its gravity field and cannot escape if their distance is less than

$$R_{\text{Hill}} = a(1-e)\left(\frac{m_2}{3m_1}\right)^{1/3}. \tag{1.74}$$

1.4.3 N-Body Systems

For multiple planets m_i around a star m_0, the overall potential has contribution from all the n masses present. The motion of the i-th body is subjected to the attraction of the other $n-1$ bodies:

$$\ddot{\mathbf{r}}_i = -G(m_0+m_i)\frac{\mathbf{r}_i}{r_i^3} + \sum_{j=1,j\neq i}^{n} Gm_j\left(\frac{\mathbf{r}_j-\mathbf{r}_i}{|\mathbf{r}_j-\mathbf{r}_i|^3} - \frac{\mathbf{r}_j}{|\mathbf{r}_j^3|}\right) \tag{1.75}$$

where the first is the Keplerian term, the second term contains the *direct* contribution, due to planet-planet interaction, and *indirect* contribution, due to the fact that the system of coordinates is centered in the star and not in the centre of mass, so the reference frame is not inertial.

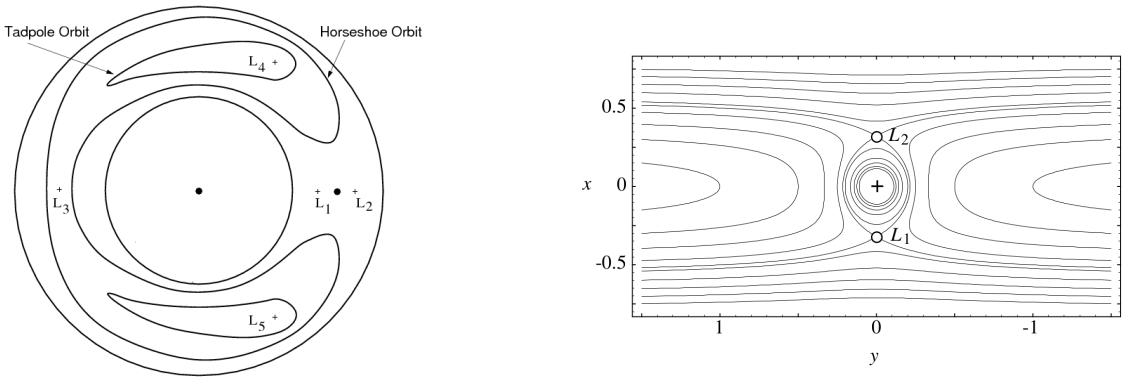

Figure 1.11: *Left*: examples of tadpole and horseshoe orbits around L_4 and L_5. *Right*: zero-velocity curves in the vicinity of L_1 and L_2. Credits: Murray and Dermott 2000.

1.4.4 Mean Motion Resonances

A *mean motion resonance* (MMR) occurs when the orbital periods of two planets are close to a ratio of small integers. A significant number of exoplanets are close to low-order resonances, like the $2:1$ or $3:2$, for example HD 45364 (Rein et al. 2010), KOI 55 (Charpinet et al. 2011), Gliese 876, HD 82943 and HD 37124 (Wright et al. 2011). A resonant configuration may be either the outcome of planetary formation or a consequence of trapping during a migration process. Resonances can be the source of both stability and instability, and play an important role in shaping the configuration of a planetary system.

Two planets are in a mean motion resonance when the ratio of their mean motions n_1 and n_2 is close to

$$\frac{n_1}{n_2} = \frac{p+q}{p} \tag{1.76}$$

where $p \neq 0$ and $q \geq 0$ are small integers and q is the order of the resonance. When this occurs, the planets periodically line up at the same points in their orbits, which introduces a repetitive force that cannot be assumed to average to zero over long timescales. The geometry is described by the libration of a *resonant angle*, which is a linear combination of the angular variables:

$$\phi_1 = (p+q)\lambda_2 - p\lambda_1 - q\varpi_1, \quad \phi_2 = (p+q)\lambda_2 - p\lambda_1 - q\varpi_2. \tag{1.77}$$

For the full Hamiltonian formulation see appendix A.

In order to consider a planet pair resonant, the range of mean motion values allowed is about (Malhotra 2012)

$$\frac{\Delta n}{n} \simeq \mu^{\frac{q+1}{3}} \tag{1.78}$$

for nearly circular orbits, where μ is the planet-star mass ratio and $0 \leq q \leq 2$. In Keplerian orbits the resonant condition for two planets implies a ratio of their semi-major axes of $a_2/a_1 = (n_1/n_2)^{2/3}$. For a $2:1$ resonance, if both angles ϕ_1 and ϕ_2 librate, then the system is said to be in a state of *apsidal*

corotation resonance, where the two lines of periapse rotate with the same average speed; if only one of the angles librates and the other circulates, the system is still in resonance but it is less tight. The formation of resonant planetary systems is generally the outcome of a differential migration process (see Section 1.5) when the drift speeds of the planets are not identical. Whenever the location of a resonance is crossed, the mutual interaction becomes stronger due to the periodic perturbations and the planets can be trapped in a resonance for the rest of their migration.

1.5 Migration

To justify most currently known exoplanets' orbits it has become imperative to adjust the classical theory of planet formation which predicts circular orbits with radii of a few AU or beyond (Armitage and Rice 2005). The extremely short orbital periods of many hot Jupiters pose a problem for planet formation, since such systems are significantly different to the Solar System: furthermore, high temperatures expected at such small radii would prevent the possibility of *in situ* formation by destroying ices and dust. Therefore, the cores of these hot Jupiters must have formed elsewhere before being moved inward. There are certain physical mechanisms which allow to reconcile observation and theory: the most important is migration in the early stages of a gaseous disc, which enables planets to lose angular momentum by means of three kinds of processes.

1.5.1 Type I Migration

The presence of a planet in a PPD generates a non-axisymmetric time varying gravitational potential: the gas reacts to this perturbation by forming density waves that in turn affect the planet by changing its angular momentum (Figure 1.12). Type I migration involves the interaction between the planet and the gas in the PPD and is efficient for planet masses $M_p \lesssim 0.1\ M_J$ which are not able to carve a gap.

Given a planet orbiting a star with rotation frequency Ω_p equal to the Keplerian frequency, we can identify zones in the disc where the gas and the planet are in a resonant relation. These correspond to

- *Corotation resonances* at $\Omega = \Omega_\mathrm{p}$: if the disc is Keplerian the corotation resonance is found at the planet's orbital radius;
- *Lindblad resonances* at $m(\Omega - \Omega_\mathrm{p}) = \pm\kappa$, where m is an integer and the epicyclic frequency[‡] κ is such that

$$\kappa^2 = \left(R\frac{\mathrm{d}\Omega^2}{\mathrm{d}R} + 4\Omega^2 \right). \tag{1.79}$$

  For a Keplerian potential $\kappa = \Omega$. The positions of these resonances are given by

$$r_\mathrm{ILR} = r_\mathrm{p} \left(\frac{m}{m-1} \right)^{-2/3} \tag{1.80}$$

[‡]frequency at which a radially displaced fluid parcel will oscillate

for the inner Lindblad resonance (faster than the planet) and

$$r_{\rm OLR} = r_{\rm p}\left(\frac{m}{m+1}\right)^{-2/3} \tag{1.81}$$

for the outer Lindblad resonance (slower than the planet).

A circular Keplerian disc therefore has a single corotation resonance and a series of Lindblad resonances piling up close to the planet. The rate of migration is controlled by the sum of the torques arising from the inner and outer Lindblad and corotation resonances. Generally, for Lindblad resonances, the dominant torque arises from wavenumbers $m \simeq \frac{r_p}{H}$, with H disc scale height (Korycansky and Pollack 1993). Corotation torques arise from the exchange of angular momentum at the horseshoe orbit and may be dominant when the region is not saturated[§], thus reversing the sign of the torque.

The torques at non-resonant locations in the disc do not interfere constructively and therefore cancel out when averaged. According to the study of Tanaka et al. 2002 the net torque scales with the planet mass as $\Gamma_{\rm tot} \propto m_p^2$, so that the migration timescale at a given radius scales as $\tau_{\rm I} \propto m_p^{-1}$, i.e. the migration becomes increasingly important as the planet mass increases, and is fastest just prior to gap opening. The conservation of angular momentum implies

$$\frac{{\rm d}J_{\rm p}}{{\rm d}t} = \Gamma_{\rm tot} \tag{1.82}$$

where the angular momentum of the planet is $J_{\rm p} = m_{\rm p}(GM_* r_{\rm p})^{1/2}$. The migration velocity can be obtained as

$$\frac{{\rm d}r_{\rm p}}{{\rm d}t} = -2r_{\rm p}\frac{\Gamma_{\rm tot}}{J_{\rm p}} \tag{1.83}$$

Depending on the sign of the torque, the migration can proceed inwards or outwards: for most PPD models, migration is inwards and rapid, with timescales of $\sim 10^4$ years. These results seem to indicate that the planet falls quickly into the host star, so some changes to the current theory are required to conciliate observations. Some processes that are believed to be crucial for more reliable estimates are, for example, turbulence and non-isothermal migration.

1.5.2 Type II Migration

At higher masses, $M_p \gtrsim 0.1\ M_J$, the angular momentum removal/deposition at the planet's inner/outer Lindblad resonances is strong enough to repel gas from an annular region surrounding the planet's orbit, forming a gap in which the surface density is reduced (Figure 1.12).

The conditions for a planet to be able to open a gap are of two kinds:

[§]the material gets mixed and the torques decline on timescales of the libration time $\tau_{\rm lib} = 4a_{\rm p}P_{\rm p}/(3x_{\rm s})$ with, $x_{\rm s}$ half-width of the horseshoe region (Kley et al. 2009)

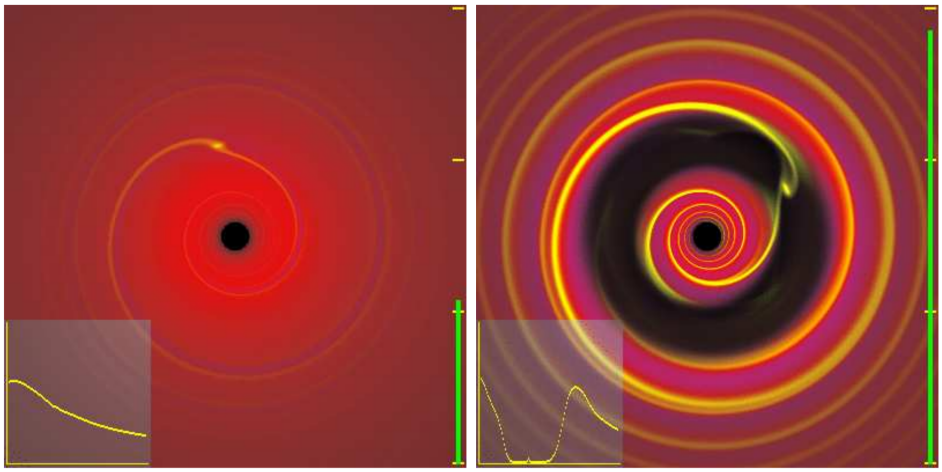

Figure 1.12: Interaction between a planet on a fixed circular orbit with a laminar PPD computed from a two-dimensional hydrodynamic simulation with a locally isothermal equation of state. *Left*: example of type I migration in which a low mass planet excites a wave in the disc gas but does not significantly perturb the surface density profile (shown in the lower left corner). *Right*: example of a massive planet which clears an annular gap in the disc within which the surface density is a small fraction of its unperturbed value. Credits: Armitage and Rice 2005.

- *Thermal condition*: the Hill sphere of a planet must be comparable to the disc scale height, or else the gas will fill the gap away from the midplane. For circular orbits:

$$R_{\rm Hill} = r_{\rm p}\left(\frac{m_{\rm p}}{3M_*}\right)^{1/3} \geq H_{\rm p} \tag{1.84}$$

or

$$q = m_{\rm p}/M_* \geq 3\left(\frac{H_{\rm p}}{r_{\rm p}}\right)^3, \tag{1.85}$$

with $\frac{H_{\rm p}}{r_{\rm p}}$ aspect ratio at the planet radius.

- *Viscous condition*: the boundaries of the gap are determined by the balance between angular momentum exchange with the planet, which tends to widen the gap, and internal viscous stresses in the PPD, which tend to close it. By equating the timescale for type I torques to open a gap to the timescale for viscous diffusion to fill it in we obtain:

$$q \geq \frac{243\pi}{8}\alpha\left(\frac{H_{\rm p}}{r_{\rm p}}\right)^2. \tag{1.86}$$

Once the planet is massive enough to open a gap, the gas is being pushed away from the planet and the torques diminish, so that the planet remains locked into the long term viscous evolution of the

disc and migrates on a timescale of

$$\tau_{\mathrm{II}} = \frac{r_{\mathrm{p}}^2}{\nu} = \frac{1}{\alpha}\left(\frac{r_{\mathrm{p}}}{H_{\mathrm{p}}}\right)^2 \Omega_{\mathrm{p}}^{-1}. \tag{1.87}$$

This means the rate of migration is independent of the planet mass: however this is only valid if the planet is not too massive. This condition can be parametrised by the value (Syer and Clarke 1995)

$$B = \frac{3\pi\Sigma r_{\mathrm{p}}^2}{m_{\mathrm{p}}}. \tag{1.88}$$

For $B \ll 1$, the timescale previously obtained must be multiplied by this quantity, i.e. migration slows down for very large masses.

1.5.3 Type III Migration

An additional migration mechanism was introduced by Masset and Papaloizou 2003 known as type III or *runaway migration*. This process is associated to coorbital torques acting on a partially opened gap: this results in very fast migration for Saturn-like planets embedded in massive discs. However, this type of mechanism is still just hypothesized.

2
State of the Art and Aims

PPDs are the key to understand the process of planet formation. The mechanisms that lead to the birth of planetary systems are still quite obscure and their insight requires extensive work by combining theory, observations and numerical simulations. The new frontier for investigation of planet formation is the study of the dust distribution, since instruments like ALMA and SPHERE allow to observe the coldest objects of the universe. On the other hand, it is necessary to combine reliable numerical simulations able to put constraints on theoretical quantities.

2.1 State of the Art

There is observational evidence that imposes to revise the assumption of axisymmetric distribution of gas and dust in PPDs with smooth radial profiles. A variety of structures has been observed, such as rings, gaps, spirals and warps, like the examples in Figure 2.1. Some of these structures are believed to be either a consequence or a precursor to planet formation: embedding a planet into the disc leads to disturbances in the density of the disc, like spiral waves or, if the planet is massive enough, a gap. However, the disc does not simply undergo structural changes due to the planets, but the opposite is also true, and in fact its effects on the planetary orbits play a fundamental role in the final configuration of the system. The observed semi-major axes distribution of extrasolar planets does not match the one of the Solar System, potentially consistent with the *in situ* formation scenario: a large amount of planets — like the first one to be discovered, 51 Peg (Mayor and Queloz 1995) — are too close to the star to have been formed with the solids available at such distance. This has led to the conclusion that planetary migration (Section 1.5) must have taken part for most currently observable systems.

This explanation still does not lack of inconsistencies, even in our own Solar System: masses such as the ones of Jupiter and Saturn would have been able to open a gap in the disc and trigger inner type II migration on timescale of ~ 100 Kyr, so why are they currently so far away from the Sun? That is where the *Grand Tack* theory (Walsh et al. 2011) comes to the aid: this model proposes that the inner Solar System was sculpted by the giant planets' orbital migration in the PPD. Jupiter first migrated inward then Jupiter and Saturn migrated back outward together within about 10^5 years through the following steps:

1. the cores of Jupiter and Saturn formed by accretion of planetesimals and migrated due to type I interaction with the disc;

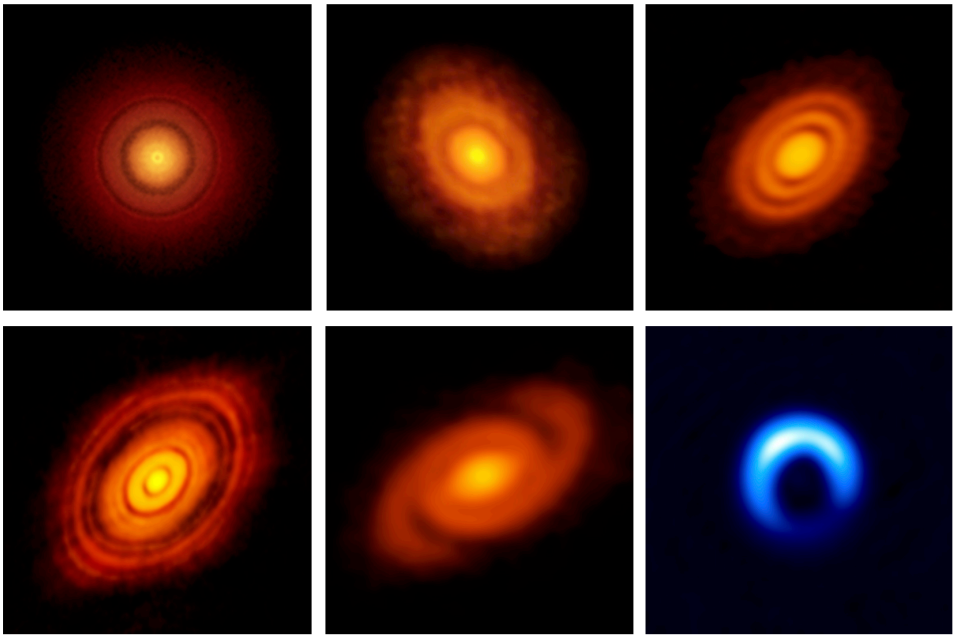

Figure 2.1: Gallery of high angular resolution continuum observations of planet forming discs obtained with ALMA. From *left* to *right* and from *top* to *bottom*: TW Hya (Andrews et al. 2016), V883 Ori (Cieza et al. 2016), HD 163296 (Isella et al. 2016), HL Tau (ALMA Partnership 2015), Elias 2-27 (Pérez et al. 2016), and HD 142527 (Kataoka et al. 2016).

2. Jupiter and Saturn's cores accreted gas, at first slowly, then more rapidly: this began to stop when the planets opened annular gaps in the disc and transitioned to type II migration;

3. once fully formed, Saturn migrated faster, caught up to Jupiter and was trapped in a $2:1$ or $3:2$ resonance;

4. the gaps carved by the two planets overlapped and the torque balance caused Jupiter and Saturn to migrate outwards while remaining trapped in resonance, until the disc dissipated.

Since a significant number of exoplanets are close to low-order resonances (Wright et al. 2011) it is believed that this mechanism might be recurring in planetary systems potentially observable with ALMA and SPHERE via dust blackbody or scattered emission. The shape of the common gap strongly depends on the disc and planet parameters (e.g. D'Angelo and Marzari 2012, Masset and Snellgrove 2001), thus allowing to compare observational and numerical data. Recent 2D simulations by Marzari et al. 2018 of gas and dust discs including radiative transfer show that outward migration happens both for $3:2$ and $2:1$ resonant configurations, where the latter leads to high orbital eccentricities (Figure 2.2). The setups result in the formation of a common gap (Figure 2.2) in the dust distribution for all grain sizes considered (from $10\ \mu\mathrm{m}$ to $1\ \mathrm{cm}$), with the exception of some particles trapped in the coorbital regions. The gap in the dust progressively broadens as the planets migrate outward while that of the gas remains approximately constant (Figure 2.3).

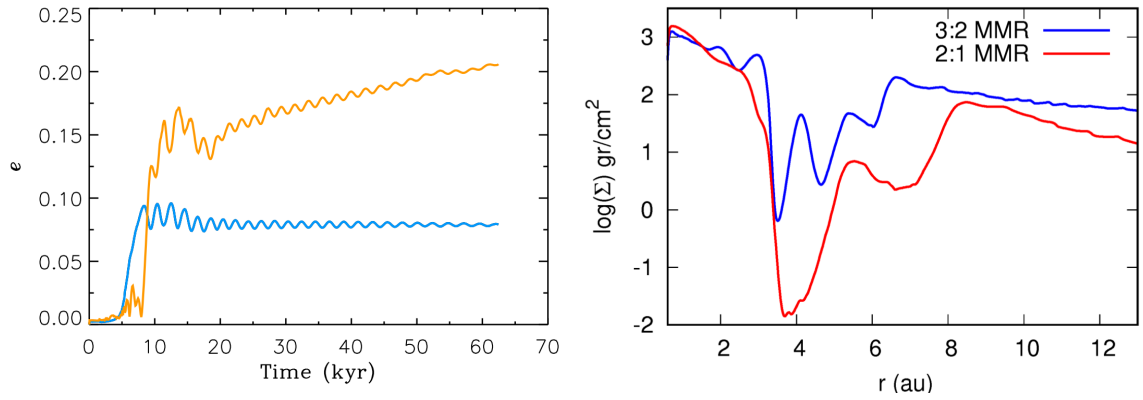

Figure 2.2: *Left*: orbital eccentricity evolution of a Jupiter-Saturn mass pair converging into the $2:1$ MMR and then migrating outwards. *Right*: common dust gap for the planet pair locked in the $3:2$ and $2:1$ MMR. Credits: Marzari et al. 2018.

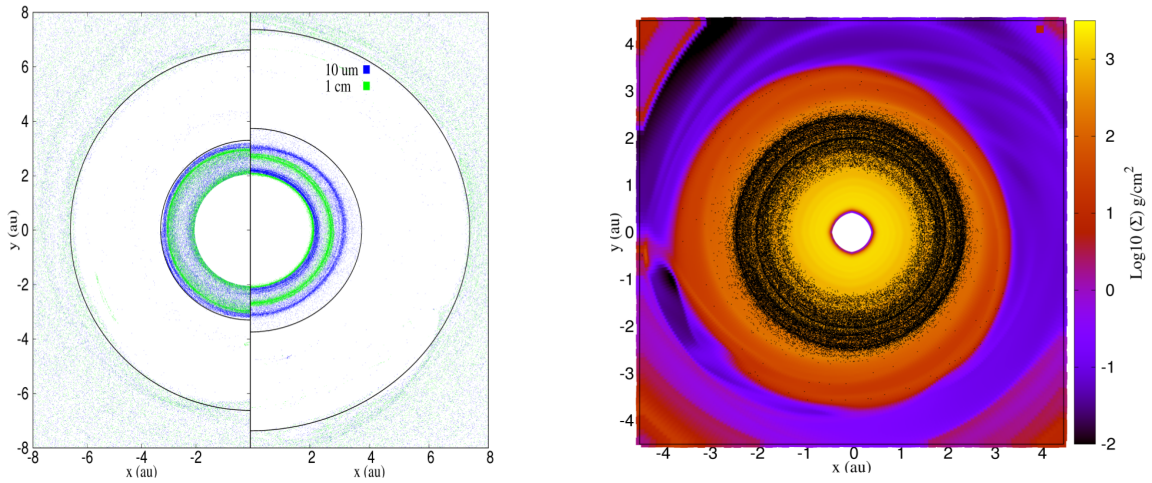

Figure 2.3: *Left*: Dust distribution of $10\ \mu\mathrm{m}$ and $10\ \mathrm{cm}$ at two different evolutionary times for the $3:2$ MMR. The edges of the common gas gap are shown in black. The larger grains also drift inward increasing the extent of the dust gap. *Right*: gas density distribution and dust particles ($10\ \mu\mathrm{m}$) in the inner region of the disc after $30\ \mathrm{Kyr}$ of the $2:1$ MMR. Credits: Marzari et al. 2018.

2.2 Aims

The purpose of my thesis is to investigate the effects of two planets locked in resonance on the dust distribution of a PPD via a set of numerical simulations. What my work aims to offer additionally to previous results is a tridimensional approach to the numerical simulations to check whether this kind of setup will lead to major changes compared to the results of a bidimensional configuration. The relevance of the third dimension has not been properly investigated in recent literature: given the increasing quantity of scientific data provided by powerful instrumentation like ALMA and SPHERE it has become crucial to develop more realistic simulations to accurately interpret the process of planet

formation that we are able to observe through these images. The code I used, PLUTO (Mignone et al. 2007), is very promising for the modelling of PPDs and is being currently updated to properly simulate a large variety of scenarios: in particular, my simulations include a freshly implemented module for the reproduction of dust particles which is still being tested in different environments. My simulations, albeit limited in space and time due to the massive computational time required for a 3D setup, aim to provide a 'snapshot' of the long process of resonant migration in order to closely analyse the early formation of a gap in both gas and dust.

My thesis is going to be structured this way: Chapter 3 will introduce PLUTO code and show the initial conditions of my simulations; Chapter 4 will explain the results obtained with the simulations; Chapter 5 will summarise the work done, highlight the main inferences and present how I aim going to improve and expand this thesis in the future.

3
Numerical Simulations

3.1 Computational Fluid Dynamics

Computational fluid dynamics is the analysis of systems involving fluid flow, heat transfer and associated phenomena by means of computer-based simulations.
The first steps for approaching a flow problem are the definition of the geometry of the region of interest — the computational *domain* —, the *grid* or *mesh* generation — the sub-division of the domain into a number of smaller sub-domains, *cells* —, followed by the selection of the physical phenomena that need to be modelled, the definition of fluid properties and the specification of boundary conditions at cells which coincide with the domain boundary. The solution to a flow problem is defined at *nodes* inside each cell. The number of cells in the grid affect both the accuracy of a solution and its cost in terms of necessary computer hardware and calculation time. Once determined the settings and the initial conditions of the problem, the code must now use a *solver*. The *finite volume* method is structured into the following steps: integration of the governing equations of fluid flow over the finite volumes of the domain, dicretisation — i.e. conversion of the resulting integral equations into a system of algebraic equations — and solution of the algebraic equations by an *iterative method*.

3.2 PLUTO Code

PLUTO (Mignone et al. 2007) is a tridimensional Eulerian code designed to integrate a system of conservation laws

$$\frac{\partial \mathbf{U}}{\partial t} = -\nabla \cdot \mathbf{T}(\mathbf{U}) + \mathbf{S}(\mathbf{U}) \tag{3.1}$$

where $\mathbf{U}$ is a vector of conservative quantities, $\mathbf{T}(\mathbf{U})$ is a rank-2 tensor, whose rows are the fluxes of each component of $\mathbf{U}$, and $\mathbf{S}(\mathbf{U})$ is the source term. Although the components of $\mathbf{U}$ are the primary variables being updated, fluxes are more conveniently computed using a different set of physical quantities, the primitive vector $\mathbf{V}$. The *finite volume* formalism is composed of an interpolation routine followed by the solution of Riemann problems at zone edges and a final evolution stage. The standard two-points difference one-dimensional operator is

$$\mathcal{L}^d = -\frac{1}{\Delta \mathcal{V}^d}(A^d_+ \mathbf{F}^d_+ - A^d_- \mathbf{F}^d_-) + \mathbf{S}^d \tag{3.2}$$

where $d = 1, 2, 3$ is a given direction, $A^d_\pm$ and $\mathcal{V}^d$ are respectively the cell's right and left interface areas and cell volume in that direction. The numerical flux functions $\mathbf{F}_\pm = \mathcal{R}(\mathbf{V}_{+,\mathrm{L}}, \mathbf{V}_{+,\mathrm{R}})$ follow the solution of 1D Riemann problems at cell interfaces, where $\mathcal{R}$ is the Riemann solver and $\mathbf{V}_{+,\mathrm{L}}$, $\mathbf{V}_{+,\mathrm{R}}$ are left and right states at the zone edges.

3.2.1 Reconstruction

Interpolation routines are designed to reconstruct a piecewise polynomial approximation $\mathcal{P}(\mathbf{x})$ to $\mathbf{V}$ inside each cell starting from its cell averages:

$$\mathbf{V}_{\pm,S} = \mathcal{I}(\mathcal{P}, \mathbf{V}) \tag{3.3}$$

where S=L (S=R) at $\mathbf{x} = \mathbf{x}_+$ ($\mathbf{x} = \mathbf{x}_-$). $\mathcal{I}$ is an interpolation routine designated to provide left and right edge interpolated values inside each cell:

$$\mathbf{V}_{+,\mathrm{L}} = \lim_{\mathbf{x}\to\mathbf{x}_+} \mathcal{P}(\mathbf{x}) \tag{3.4}$$

$$\mathbf{V}_{-,\mathrm{R}} = \lim_{\mathbf{x}\to\mathbf{x}_-} \mathcal{P}(\mathbf{x}). \tag{3.5}$$

3.2.2 Riemann Solver

Computation of the numerical flux function $\mathbf{F}_+$ at a zone edge (x_+) requires the solution $\mathbf{U}(x, t)$, for $t > t_0$, to the initial value problem

$$\mathbf{U}(x, t_0) = \begin{cases} \mathbf{U}_{+,\mathrm{L}} & \text{if } x < x_+ \\ \mathbf{U}_{+,\mathrm{R}} & \text{if } x > x_+. \end{cases} \tag{3.6}$$

The solution to the Riemann problem, known as *Godunov scheme*, can be obtained analytically but generally different levels of approximations are introduced in order to reduce the computational time required.

3.2.3 Temporal Evolution

In the simplest case of forward Euler dicretisation

$$\frac{\mathbf{U}^{n+1} - \mathbf{U}^n}{\Delta t} = \mathcal{L}^2. \tag{3.7}$$

The time step Δt is limited by the Courant-Friedrichs-Lewy (Courant et al. 1928) condition:

$$\Delta t = C_a \min_d \left(\frac{\Delta l^d_{\min}}{|\lambda^d_{\max}|} \right), \tag{3.8}$$

with $\Delta l^d_{\min}$ and $\lambda^d_{\max}$ respectively the smallest cell length and largest signal velocity in the d direction, while C_a is the Courant number.
The time-marching schemes provided by PLUTO are of two kinds: zone-edge extrapolated and semi-discrete. Zone-edge extrapolated methods are based on a single step:

$$\mathbf{U}^{n+1} = \mathbf{U}^n + \Delta t \mathcal{L}^{n+\frac{1}{2}}. \tag{3.9}$$

Examples of semi-discrete method are the *total variation diminishing* Runge-Kutta schemes: the second-order method advances the system of conservation laws as

$$\mathbf{U}^* = \mathbf{U}^n + \Delta t \mathcal{L}^n \tag{3.10}$$

$$\mathbf{U}^{n+1} = \frac{1}{2} \left[\mathbf{U}^n + \mathbf{U}^* + \Delta t \mathcal{L}^* \right]. \tag{3.11}$$

3.2.4 Hydrodynamics Module

In this work I used the hydrodynamics module, which means I neglected relativistic corrections and magnetohydrodynamics. This module solves the Euler or Navier-Stokes equations of gas dynamics:

$$\frac{\partial}{\partial t} \begin{pmatrix} \rho \\ \mathbf{m} \\ E + \rho\Phi \end{pmatrix} + \begin{pmatrix} \rho\mathbf{v} \\ \mathbf{m} \cdot \mathbf{v} + p\mathbf{I} \\ (E + p + \rho\Phi)\mathbf{v} \end{pmatrix}^{\mathrm{T}} = \begin{pmatrix} 0 \\ -\rho\nabla\Phi + \rho\mathbf{g} \\ \mathbf{m} \cdot \mathbf{g} \end{pmatrix}, \tag{3.12}$$

where $\mathbf{m} = \rho\mathbf{v}$ is the momentum density, $\mathbf{v}$ is the velocity and $\mathbf{I}$ is the unit 3×3 tensor. The total energy density E is related to the thermal pressure p:

$$E = \frac{p}{\Gamma - 1} + \frac{|\mathbf{m}|^2}{2\rho}. \tag{3.13}$$

The source term on the right includes contributions from body forces and depends on the gravitational potential Φ and the acceleration vector $\mathbf{g}$. The vector of primitive quantities $\mathbf{V} = (\rho, \mathbf{v}, p)^T$ follows the equations:

$$\frac{\partial \rho}{\partial t} + \mathbf{v} \cdot \nabla\rho + \rho\nabla \cdot \mathbf{v} = 0 \tag{3.14}$$

$$\frac{\partial \mathbf{v}}{\partial t} + \mathbf{v} \cdot \nabla \mathbf{v} + \frac{\nabla p}{\rho} = -\nabla \Phi + \mathbf{g} \tag{3.15}$$

$$\frac{\partial p}{\partial t} + \mathbf{v} \cdot \nabla \rho + \rho c_s^2 \nabla \cdot \mathbf{v} = 0. \tag{3.16}$$

Where $c_s = \sqrt{\Gamma p/\rho}$ is the adiabatic speed of sound for an ideal equation of state.

3.2.4.1 Viscosity

The presence of viscosity requires to add the viscous stress tensor $\mathbf{\Pi}$ to the original conservation law:

$$\frac{\partial \mathbf{U}}{\partial t} + \nabla \cdot \mathbf{T} = \nabla \cdot \mathbf{\Pi} + \mathbf{S}. \tag{3.17}$$

$$(\mathbf{\Pi})_{ij} = 2\frac{\nu_1}{h_i h_j}\left(\frac{v_{i;j} + v_{j;j}}{2}\right) + \left(\nu_2 - \frac{2}{3}\nu_1\right)\nabla \cdot \mathbf{v}\delta_{ij}. \tag{3.18}$$

Coefficients ν_1 and ν_2 are the *shear* and *bulk* parameters of viscosity, $v_{i;j}$ and $v_{j;j}$ denote the covariant derivatives and h_i, h_j are the geometrical elements of the respective direction.

3.2.5 Radiation Module

Radiative effects play a very important role in most astrophysical fluid flows. The complete set of equations for the evolution of the gas is (Kolb et al. 2013):

$$\frac{\partial \rho}{\partial t} + \nabla \cdot (\rho \mathbf{v}) = 0 \tag{3.19}$$

$$\frac{\partial \rho}{\partial t}\mathbf{v} + \nabla \cdot (\rho \mathbf{v} \times \mathbf{v}) + \nabla p = \rho(\mathbf{a}_{\rm ext} + \mathbf{a}_{\rm rad}) \tag{3.20}$$

$$\frac{\partial e}{\partial t} + \nabla \cdot [(e + p)\mathbf{v}] = \rho \mathbf{v} \cdot (\mathbf{a}_{\rm ext} + \mathbf{a}_{\rm rad}) - \kappa_{\rm P}\rho c(a_{\rm R}T^4 - E) \tag{3.21}$$

with $e = \rho\epsilon + 1/2\rho v^2$ total energy density of the gas without radiation, $\mathbf{a}_{\rm ext}$ acceleration caused by external forces and $\mathbf{a}_{\rm rad}$ acceleration induced by the radiation field. Finally, the ideal gas relation imposes

$$p = (\gamma - 1)\rho\epsilon = \rho\frac{{\rm k_B}T}{\mu m_{\rm H}} \tag{3.22}$$

where γ is the ratio of specific heats, T the gas temperature, ${\rm k_B}$ the Boltzmann constant, μ the mean molecular weight and $m_{\rm H}$ the mass of hydrogen. The specific internal energy can be written as $\epsilon = c_{\rm V}T$, with the specific heat capacity $c_{\rm V} = {\rm k_B}/[(\gamma - 1)\mu m_{\rm H}]$. The evolution of the radiation energy

density E is given by

$$\frac{\partial E}{\partial t} + \nabla \cdot \mathbf{F} = \kappa_{\mathrm{P}} \rho c (a_{\mathrm{R}} T^4 - E) \tag{3.23}$$

where $\mathbf{F}$ denotes the radiative flux, κ_{P} the Planck mean opacity, c the speed of light and a_{R} the radiation constant. The radiation affects the fluid in two ways: first, the radiation may be absorbed or emitted by the fluid, leading to variation of its energy density; the second effect is radiation pressure, which acts as an additional acceleration to the momentum equation, $\mathbf{a}_{\mathrm{rad}} = \frac{\kappa_{\mathrm{P}}}{c}\mathbf{F}$. Further assumptions must be made for the radiative flux $\mathbf{F}$ in order to solve the system of equations: the flux-limited diffusion approximation is used, where

$$\mathbf{F} = -\lambda \frac{c}{\kappa_{\mathrm{R}} \rho} \nabla E \tag{3.24}$$

with κ_{R} Rosseland mean opacity. The flux-limiter λ describes the transition from optically thick to thin regions. We must define

$$R = \frac{|\nabla E|}{\kappa_{\mathrm{R}} \rho E} \tag{3.25}$$

such that

$$\lambda(R) = \begin{cases} \frac{1}{3}, & R \to 0 \\ \frac{1}{R}, & R \to \infty. \end{cases} \tag{3.26}$$

3.2.5.1 Opacity

For the calculation of the opacities the code is based on Semenov et al. 2003. It is assumed that in the temperature range $0 < T < 1500\,\mathrm{K}$ the opacity is dominated by dust grains, whereas for higher temperatures gas is the only source of opacity. The solar composition of the elements is adopted from Anders and Grevesse 1989. Dust grains are supposed to consist of silicates, iron, troilite, organics and ice (Pollack et al. 1994, Henning and Stognienko 1996). The size distribution adopted is a modified version of Mathis et al. 1977:

$$\begin{cases} \frac{\mathrm{d}n}{\mathrm{d}s} \propto s^{-3.5} \text{ for } 5\,\mathrm{nm} < s < 1\,\mu\mathrm{m} \\ \frac{\mathrm{d}n}{\mathrm{d}s} \propto s^{-5.5} \text{ for } 1\,\mu\mathrm{m} < s < 5\,\mu\mathrm{m} \end{cases} \tag{3.27}$$

The silicates are considered to be three various types, depending on their iron content. However, the absolute amount of solid metallic iron in the model is kept unchanged:

- *iron-poor* silicates, $\mathrm{Fe}/(\mathrm{Fe} + \mathrm{Mg}) = 0.0$
- *iron-rich* silicates, $\mathrm{Fe}/(\mathrm{Fe} + \mathrm{Mg}) = 0.4$
- *normal* silicates, $\mathrm{Fe}/(\mathrm{Fe} + \mathrm{Mg}) = 0.3$

The dust grains are modelled as aggregates or spherical particles with different distribution of the dust constituents:

- homogeneous dust particles, where each particle consists of the only one dust material
- composite particles, where each particle includes all dust materials according to their mass fraction
- porous composite particles, where half of the particle volume consists of all dust materials according their mass fraction the other half is vacuum.

For gas temperatures between 1500 and 10000 K, where all the dust grains have evaporated, the gas opacity is computed according to Helling et al. 2000.

3.2.6 Dust Dynamics

Dust particles are treated as Lagrangian particles immersed in the gaseous disc (Picogna et al. 2018). The forces acting on dust grains are of different kinds:

- gravitational force of the central star and the planets
- drag force due to the difference between the particles' Keplerian velocity and the gas' sub-Keplerian velocity
- gas turbulent motion that spreads particles.

Other effects include photophoretic [*] gas pressure, radiation pressure and growth/fragmentation due to collisions between grains, but they will be neglected.

3.2.6.1 Drag Force

The particles are considered of spherical shapes. The drag force experienced can be described by three parameters:

- the *Knudsen number* $K = \lambda/(2s)$: ratio of the mean free path of the gas molecules and the particle's diameter
- the *Mach number* $M = v_r/c_s$: ratio of the relative velocity between dust and gas and the sound speed

[*] photophoresis is a physical phenomenon consisting in the motion of microscopic particles suspended in gas when illuminated by an intense beam of light

- the *Reynolds number* $Re = 2v_r s/\nu_m$, where the gas molecular viscosity is defined as

$$\nu_m = \frac{1}{3}\left(\frac{m_0 \overline{v}_{\rm th}}{\sigma_{\rm mol}}\right), \tag{3.28}$$

with m_0 and $\overline{v}_{\rm th} = \sqrt{\pi/8}c_s$ mass and mean thermal velocity of the gas molecules and $\sigma_{\rm mol}$ their collisional cross section.

To be able to represent a broad range of Knudsen numbers, the intermediate regime between Epstein and Stokes drag has been taken into account as well and it is modelled with the approach of Woitke and Helling 2003, which uses a quadratic interpolation between the two regimes:

$$\mathbf{F}_{\rm drag} = \left(\frac{3K}{3K+1}\right)^2 \mathbf{F}_{\rm drag,E} + \left(\frac{1}{3K+1}\right)^2 \mathbf{F}_{\rm drag,S}. \tag{3.29}$$

3.2.6.2 Turbulence

While the gas is treated as if in a laminar regime, thus neglecting the origin of the turbulence, turbulent transport has been simulated on dust with a stochastic term in the equation of dust motion to account for the kicks induced by the turbulent gas velocity field. The kick is modelled as a random Gaussian variable $\delta r_{\rm d,T}$ with mean $\langle \delta r_{\rm d,T} \rangle$ and variance $\sigma^2_{\rm d,r}$ depending on the dust diffusion coefficient:

$$\delta r_{\rm d,T} = \begin{cases} \langle \delta r_{\rm d,T} \rangle = \frac{D_{\rm d}}{\rho_{\rm g}} \frac{\partial \rho_g}{\partial x} {\rm d}t \\ \sigma^2_{\rm d,r} = 2 D_{\rm d} {\rm d}t \end{cases} \tag{3.30}$$

where ${\rm d}t$ is the time step and $\partial/\partial x$ is the spatial derivative along the considered direction.

3.2.6.3 Integrators

The particles are evolved with two different integrators depending on their Stokes numbers: a semi-implicit *leapfrog*-like integrator for larger particles and a fully implicit integrator for particles well coupled to the gas. If the particles have stopping times much smaller than the numerical timestep, the drag term can dominate the gravitational force term, causing the integrator to become numerically unstable, so a fully implicit integrator is used (Bai and Stone 2010, Zhu et al. 2014).

3.3 Simulations Setup

For my simulations I employed the hydrodynamics module to solve the Navier-Stokes equations of a tridimensional gaseous PPD and I inserted Lagrangian particles using the module developed by Picogna et al. 2018 to simulate the dust component. The aim is to model a system with two planets in a $2:1$ resonance and study the formation of gaps in the PPD. The analysis will be performed

Table 3.1: Identifiers of the four simulations characterised by different settings. The values underlined are the ones that differ from the reference simulation A.

Simulation	*Radiation*	*Orbits*	*Aspect Ratio*
A	No	Elliptical	0.02
B	No	Circular	0.02
C	No	Elliptical	0.05
D	Yes	Elliptical	0.02

on a set of simulations characterised by different setups and initial conditions. The first simulations are reduced in complexity by considering a locally isothermal equation of state, which does not require the solution of the equations of energy. The parameters changed were the scale height and the eccentricity of the planets. Then, I introduced viscous heating and radiative cooling to understand their effect on the dust distribution, by employing the radiation module previously described. The aforementioned simulations are going to be identified throughout this work by the letters indicated in table 3.1.

For these simulations I chose the *piecewise parabolic method* implemented by Mignone 2014 for reconstruction, since it is the fittest for non-uniform grid spacing and curvilinear coordinates. The time stepping chosen is a *Runge-Kutta* 2^{nd} order *total variation diminishing* algorithm:

$$\begin{cases} \mathbf{U}^* = \mathbf{U}^n + \Delta t^n \mathcal{L}^n \\ \mathbf{U}^{n+1} = \frac{1}{2}\left(\mathbf{U}^n + \mathbf{U}^* + \Delta t^n \mathcal{L}^*\right). \end{cases} \tag{3.31}$$

The Riemann solver used for flux computation is the *Harten Lax Van Leer Contact* solver (Harten et al. 1983, Toro et al. 1994).

3.3.1 Domain

The three spatial coordinates are arranged in spherical geometry, such that $\{x_1, x_2, x_3\} = \{r, \theta, \phi\}$, where r is the distance to the centre of the coordinate system, θ is the polar angle and ϕ is the azimuthal angle. The mesh is composed of 128 cells in the r direction, from 0.5 to 8 AU, 42 in the θ direction, from 82° to 90°[†], and 360 in the ϕ direction, from 0° to 360°. The domain is therefore limited in the radial and vertical direction to reduce the computational time required: this is an acceptable compromise since I deal with thin discs and the main focus of the system is in the inner area. For this reason, the grid was set to logarithmic along the r axis, i.e. the mesh size increases with the coordinate. During the following discussion I will also refer to a set of Cartesian coordinates $\{x, y, z\}$ obtained

[†]meaning that only half the disc is simulated and symmetry with respect to the midplane is assumed, for a total θ amplitude of 16°

Table 3.2: Boundary conditions at the edge of the domain.

	r	θ	ϕ
Beginning	reflective	reflective	periodic
End	reflective	eqtsymmetric	periodic

according to the transformation

$$\begin{cases} x = r\sin\theta\cos\phi \\ y = r\sin\theta\sin\phi \\ z = r\cos\theta \end{cases} \tag{3.32}$$

and to the cylidrical radius $R = r\sin\theta$. The boundary conditions applied in the 'ghost zones' of the computational domain are listed in Table 3.2. A *reflective* boundary consists of a 'rigid wall' at the edge of the domain, where variables are symmetrised across the boundary and normal components of vectors fields flip signs; an *eqtsymmetric* boundary sets equatorial symmetry with respect to a given plane; *periodic* boundaries imply that variables passing through one side of the domain reappear on the opposite side with the same components.

3.3.2 Gravitational Potential

The system considered is a PPD surrounding a star with mass $M_* = 1\,\mathrm{M}_\odot$ placed at the centre of the reference frame, so the body force inserted into the momentum and energy equations is derived from a scalar potential $\rho\mathbf{a} = -\rho\nabla\Phi$. The expression of the global potential $\Phi = \Phi(r,\theta,\phi)$ is the sum of the contribution due to the star, the planets and the non-inertial frame, since the system is centered in the star and not in the centre of mass. This gives:

$$\Phi = -\frac{G\cdot M_*}{|\mathbf{r}|} - \frac{G\cdot m_1}{|\mathbf{r}-\mathbf{r}_1|} - \frac{G\cdot m_2}{|\mathbf{r}-\mathbf{r}_2|} + \frac{G\cdot m_1}{|\mathbf{r}_1|^3}(x\cdot x_1 + y\cdot y_1) + \frac{G\cdot m_2}{|\mathbf{r}_2|^3}(x\cdot x_2 + y\cdot y_2) \tag{3.33}$$

3.3.3 Gas Component

The initial disc profile is axisymmetric and the gas moves with azimuthal velocity given by the Keplerian speed around the central star. We assume no initial radial motion of the gas. The density distribution, deriving from the force equilibrium, is given by Nelson et al. 2013

$$\rho_g = \rho_{g,0}\left(\frac{R}{R_0}\right)^p \exp\left[\frac{GM_*}{c_s^2}\left(\frac{1}{r}-\frac{1}{R}\right)\right] \tag{3.34}$$

where in this case $p = -1$ and $R_0 = 1$ AU. R is the cylindrical coordinate and $\rho_{g,0} = 10^{-9}\ \mathrm{g\ cm^{-3}}$ (Figure 3.1). Integrating over the domain, this gives a gas mass of $M_{\mathrm{disc}} \approx 0.008\ M_\odot$ and $M_{\mathrm{disc}} \approx 0.020\ M_\odot$ for a disc with $H/R = 0.02$ and $H/R = 0.05$ respectively. These values need to be

multiplied by two to obtain the actual mass of the disc, since the domain is limited to positive values of the z coordinate. These mass values allow to neglect self-gravity, which starts to become relevant for

$$\frac{M_{\rm disc}}{M_*} > \frac{H}{R}. \tag{3.35}$$

The surface density is obtained by vertically integrating the density distribution: for the chosen profiles, $\rho_{g,\rm mid} = \rho_{g,0}\left[R/(1\ \rm AU)\right]^{-1} \propto R^{-1}$ and $H \propto R$, the resulting surface density Σ is a constant:

$$\Sigma = \sqrt{2\pi} H \rho_{g,\rm mid} = const \tag{3.36}$$

which gives approximately $750\ \rm g\ cm^{-2}$ for $H = 0.02$ and $1875\ \rm g\ cm^{-2}$ for $H = 0.05$, considering the whole disc.

The initial temperature profile is

$$T = T_0 \left(\frac{R}{R_0}\right)^q \tag{3.37}$$

where in this case $q = -1$ and $R_0 = 1$ AU. T_0 is the temperature corresponding to the distance of 1 AU and is obtained from the scale height

$$H(R) = \sqrt{\frac{R^3 \rm k_B T(R)}{G M_* \mu m_H}} \tag{3.38}$$

assuming that the disc is vertically isothermal. In these simulations I have worked with constant aspect ratios H/R of 0.02 and 0.05 (Figure 3.2), which correspond to T_0 of 100 K and 640 K respectively (Figure 3.3). The mean molecular weight assumed is $\mu = 2.35$ and the viscosity is parametrised by Shakura & Sunyaev's $\alpha = 0.01$. The mean free path is obtained as

$$\lambda = \frac{\mu m_{\rm H}}{\sqrt{2}\rho_{\rm g}\sigma_{\rm mol}} \tag{3.39}$$

where $\sigma_{\rm mol} = 2 \cdot 10^{-15}\ \rm cm^{-2}$ (Chapman and Cowling 1970): this gives a lower limit of $\lambda \approx 0.7$ cm in the densest regions, i.e. the inner midplane.

The angular velocity throughout the domain is obtained from the force balance equations as well:

$$\Omega = \Omega_{\rm K}\left[(p+q)\left(\frac{H}{R}\right)^2 + (1+q) - \frac{qR}{r}\right]^{1/2} \tag{3.40}$$

with p and q indices of the density and temperature distribution.

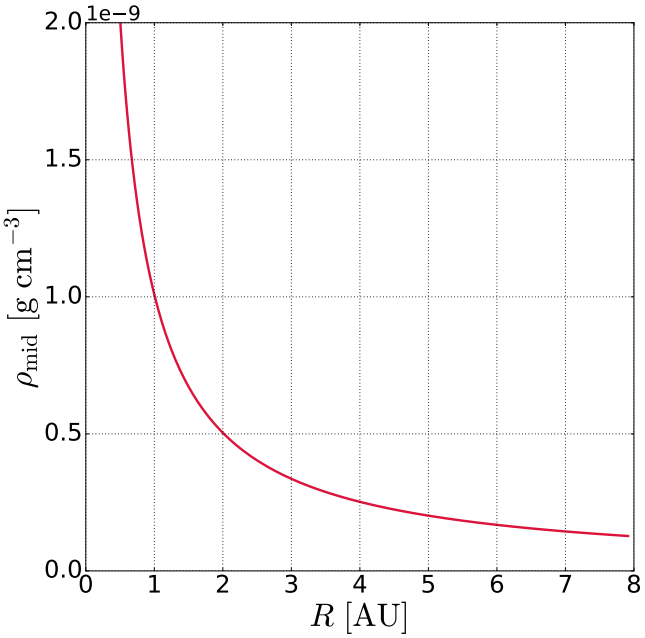

Figure 3.1: Initial gas midplane density distribution.

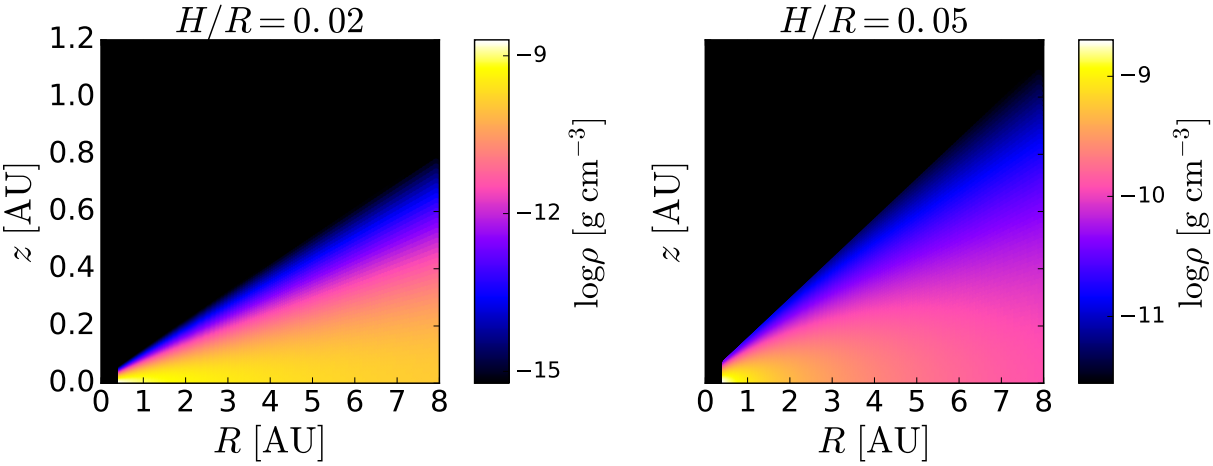

Figure 3.2: Gas density of a slice of gas at $\phi = 0$ for the different values of the aspect ratio: $H/R = 0.02$ for runs A, B and D; $H/R = 0.05$ for run C.

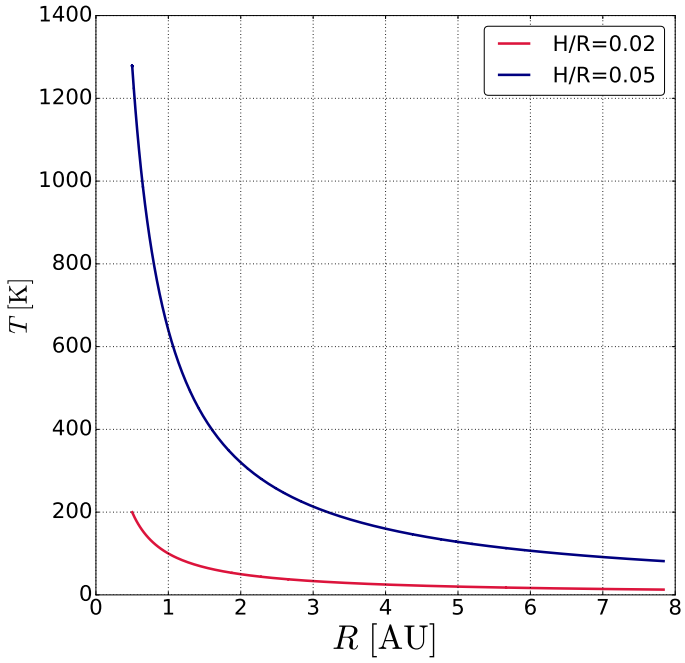

Figure 3.3: Initial gas temperature distribution for the two aspect ratios used in the simulations.

3.3.4 Dust Component

The dust component of the disc is modelled with $4 \cdot 10^5$ Lagrangian particles divided into four size bins, from 10 μm to 1 cm, with internal density $\rho_\mathrm{s} = 1\ \mathrm{g\ cm^{-3}}$. The Stokes number identifies the aerodynamic behaviour of a dust particle in the disc as explained in Section 1.2.1:

$$\mathrm{St} = \frac{\rho_\mathrm{s} s}{\rho_\mathrm{g} v_\mathrm{th}} \Omega_\mathrm{K}. \tag{3.41}$$

Particles are injected randomly in equal number per each radial ring, so the initial surface density profile of the dust particles follows (Figure 3.4)

$$\Sigma_d(r) \propto R^{-1}. \tag{3.42}$$

The vertical distribution of the particles is obtained by computing the dust scale height for each grain size's midplane Stokes number as a function of the gas scale height:

$$H_\mathrm{d} = H_\mathrm{g} \sqrt{\frac{\alpha}{\mathrm{St} + \alpha}}, \tag{3.43}$$

where α, the viscous coefficient, approximates the vertical diffusion of the gas (Youdin and Lithwick 2007): this means that for small St the particles are well coupled to the gas and the two scale heights

Table 3.3: Conversion factors for dust: each Lagrangian particle represents a certain number of dust grains.

	$10\ \mu\mathrm{m}$	$100\ \mu\mathrm{m}$	$0.1\ \mathrm{cm}$	$1\ \mathrm{cm}$
$H/R = 0.02$	$2 \cdot 10^{31}$	$2 \cdot 10^{28}$	$2 \cdot 10^{25}$	$2 \cdot 10^{22}$
$H/R = 0.05$	$6 \cdot 10^{31}$	$6 \cdot 10^{28}$	$6 \cdot 10^{25}$	$6 \cdot 10^{22}$

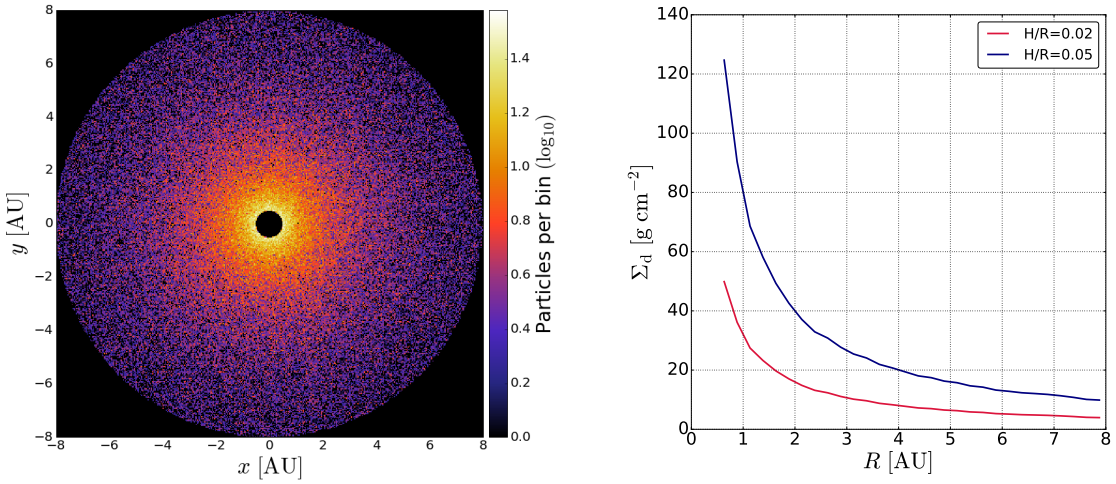

Figure 3.4: *Left*: initial dust particles distribution projected on the x-y plane. The colorbar indicates the decimal logarithm of the number of particles in each bin. A bin corresponds to $0.04\ \mathrm{AU}$. *Right*: initial dust surface density radial profile converted into physical units.

agree.

To have an idea of the number of grains of dust that each Lagrangian particle actually represents in the disc, I considered that the dust mass equals about 1% of the gas mass. Assuming that to each size range corresponds the same amount of mass, I estimated conversion factors for a disc of aspect ratios $H/R = 0.02$ and $H/R = 0.05$ (Table 3.3). This gives the dust profile in Figure 3.4, where I already accounted for the fact that my domain is representative of half a disc.

In Figure 3.5 I plotted the Stokes number distribution at the beginning of the simulations for different grain sizes for each aspect ratio: smaller particles are strongly coupled to the gas in the whole domain, while cm-size particles approach larger values at higher z, especially for the lowest aspect ratio, where the disc is less dense. On the midplane, St remains a constant for each grain size, since in this setup $\rho_{\mathrm{mid}} \propto R^{-1}$, $v_{\mathrm{th}} \propto \sqrt{T} \propto R^{-0.5}$ and $\Omega_{\mathrm{K}} \propto R^{-1.5}$. Dust particles are merely investigated under the dynamical aspect: they are subject to the gravitational potential of the star and planets, to the drag force of the gas and to the turbulent kicks, but they do not exert a back reaction on the gas and do not interact with each other.

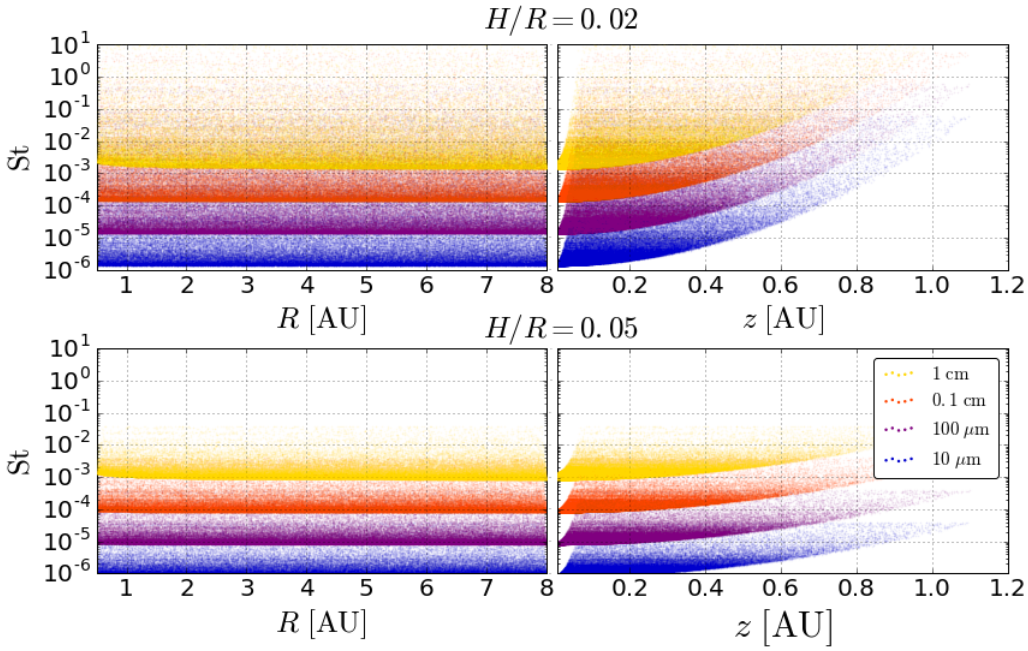

Figure 3.5: Initial Stokes number of the dust particles for the two aspect ratios.

3.3.5 Planets

The planets embedded have masses of $m_1 = 10^{-3} M_\odot$ and $m_2 = 2.99 \times 10^{-4} M_\odot$, in analogy with the masses of Jupiter and Saturn. They are put on $2:1$ resonant orbits, such that

$$\frac{n_2}{n_1} = \frac{1}{2} \rightarrow \frac{a_1}{a_2} = \left(\frac{n_2}{n_1}\right)^{\frac{2}{3}} \simeq 0.63. \tag{3.44}$$

Their semi-major axes are $a_1 = 3$ AU and $a_2 = 4.76$ AU, which correspond to orbital periods of about 5 and 10 years. In run B these orbits are circular, while they have eccentricities of $e_1 = 0.1$ and $e_2 = 0.18$ in the other runs (Figure 3.6): these values are the outcome of long term simulations obtained considering the effect of gas, dust and the planets' mutual interaction on the orbits (Marzari et al. 2018).
In my simulations these orbits are fixed, meaning planets do not migrate and do not modify their orbital elements as an effect of gas, dust or mutual interaction. The gravitational potential due to the planets needs to be treated differently close to the planet location to prevent a singularity: the potential is smoothed with a cubic expansion inside a sphere centered on the planet location with a radius given by the smoothing length $r_g = \epsilon R_{\rm Hill}$ (Klahr and Kley 2006, Stoll et al. 2017), where $R_{\rm Hill}$

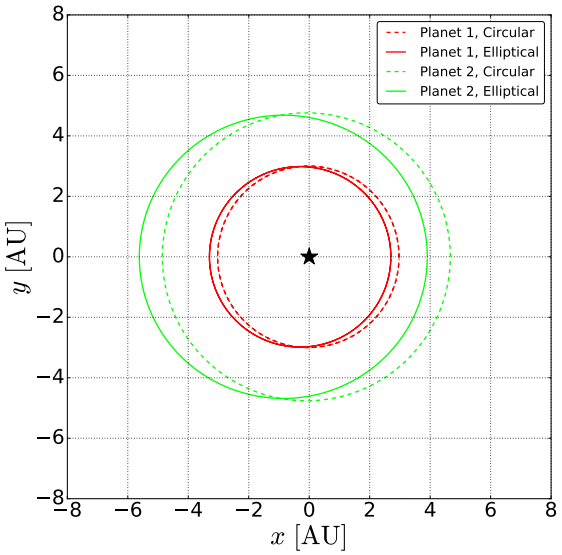

Figure 3.6: Orbits of the planets for the different choices of eccentricities.

is the radius of the Hill sphere

$$R_{\text{Hill}} = a(1-e)\left(\frac{m}{3M_*}\right)^{\frac{1}{3}}. \tag{3.45}$$

The critical distance chosen is half the Hill radius, $\epsilon = 0.5$, such that inside this area each planet's potential is multiplied by

$$\beta = \frac{|\mathbf{r}-\mathbf{r}_\text{p}|}{r_\text{g}}\left[\left(\frac{|\mathbf{r}-\mathbf{r}_\text{p}|}{r_\text{g}}\right)^3 - 2\left(\frac{|\mathbf{r}-\mathbf{r}_\text{p}|}{r_\text{g}}\right)^2 + 2\right]. \tag{3.46}$$

Also, the planets are not inserted abruptly into the system, but their masses are modulated to increase smoothly during the first 20 years of evolution, after which the planets are assigned their actual masses. The factor by which the planet masses have to be multiplied prior to $t = 20$ yr is

$$\gamma = \sin\left(\frac{2\pi \cdot t[\text{yr}]}{80}\right). \tag{3.47}$$

3.3.5.1 Planet Positions

Given the value of the eccentric anomaly E as defined in Section 1.4.1, we can obtain the projections of r, i.e. the coordinates

$$x = a(\cos E - e) \quad \text{and} \quad y = a\sqrt{1-e^2}\sin E. \tag{3.48}$$

To find the value for E we must solve *Kepler's equation*, starting from the value of the mean anomaly M:

$$M = E - e\sin E \tag{3.49}$$

which is a transcendental equation, so it requires iterative techniques. Taking $E_0 = M$ as the first approximation, we get

$$E_i + 1 = M + e\sin E_i \quad i = 0, 1, ... \tag{3.50}$$

This process is repeated until the difference between two steps is sufficiently small. In these simulations, the tolerance value was set to 10^{-10}.

3.3.6 Equation of State

In runs A, B and C the equation of state is isothermal: the temperature is locally constant and the pressure is obtained as $p = \rho c_{\text{iso}}^2$, where the sound speed was chosen according to $c_{\text{iso}}^2 = c_{\text{iso},0}^2/R$ with $c_{\text{iso},0} = \sqrt{\frac{k_B T}{\mu m_H}}$ isothermal sound speed at 1 AU.
In run D the equation of state is ideal and the ratio of specific heats $\Gamma = c_P/c_V$ is constant and equal to 1.4. The sound speed is locally calculated as $c_s^2 = \Gamma p/\rho$. While previously the temperature distribution could be neglected, in run D it is necessary to introduce an ideal equation of state since radiative effects significantly change the internal energy of the system.

4
Results

The following analysis will include the study of the behaviour of both gas and dust in the PPD. In particular, I want to understand how different initial conditions affect the formation of a gap in both components of the disc and whether it is likely that a common gap may open. Given the massive computational time required, I was able to run the simulations up to 600 years, or $\sim$ 120 orbits of the inner planet.
The data obtained from the simulations have been analysed through Python and C++ scripts.

4.1 Gas Component

4.1.1 Gas Gap

Disc and planet interact through the exchange of angular momentum caused by the tidal toque exerted by the planet's gravitational field of the circumstellar material, which alters the disc surface density. In the simplest case of a single planet on a circular orbit, a circular gap is opened in the gas, whose shape carries information about both the planet's and disc's properties. According to the criteria explained in Section 1.5, a planet is able to carve a gap if

$$\begin{cases} q \geq 3 \left(\frac{H_\mathrm{p}}{r_\mathrm{p}}\right)^3 \\ q \geq \frac{243\pi}{8} \alpha \left(\frac{H_\mathrm{p}}{r_\mathrm{p}}\right)^2 . \end{cases} \tag{4.1}$$

In the simulations considered, this is true for the two planets ($q_1 = 0.001$ and $q_2 = 0.000299$) for both values of the aspect ratio. The *depth* of the gap is defined as the ratio between the surface densities at the bottom of the gap and at the edge $\Sigma_\mathrm{min}/\Sigma_0$. The *width* of the gap is defined as the distance between the outer and the inner edge of the gap. The relation between the gap depth and the planetary mass is (Duffell and MacFadyen 2013):

$$\frac{\Sigma_\mathrm{min}}{\Sigma_0} = \frac{1}{1 + 0.04\, K} \tag{4.2}$$

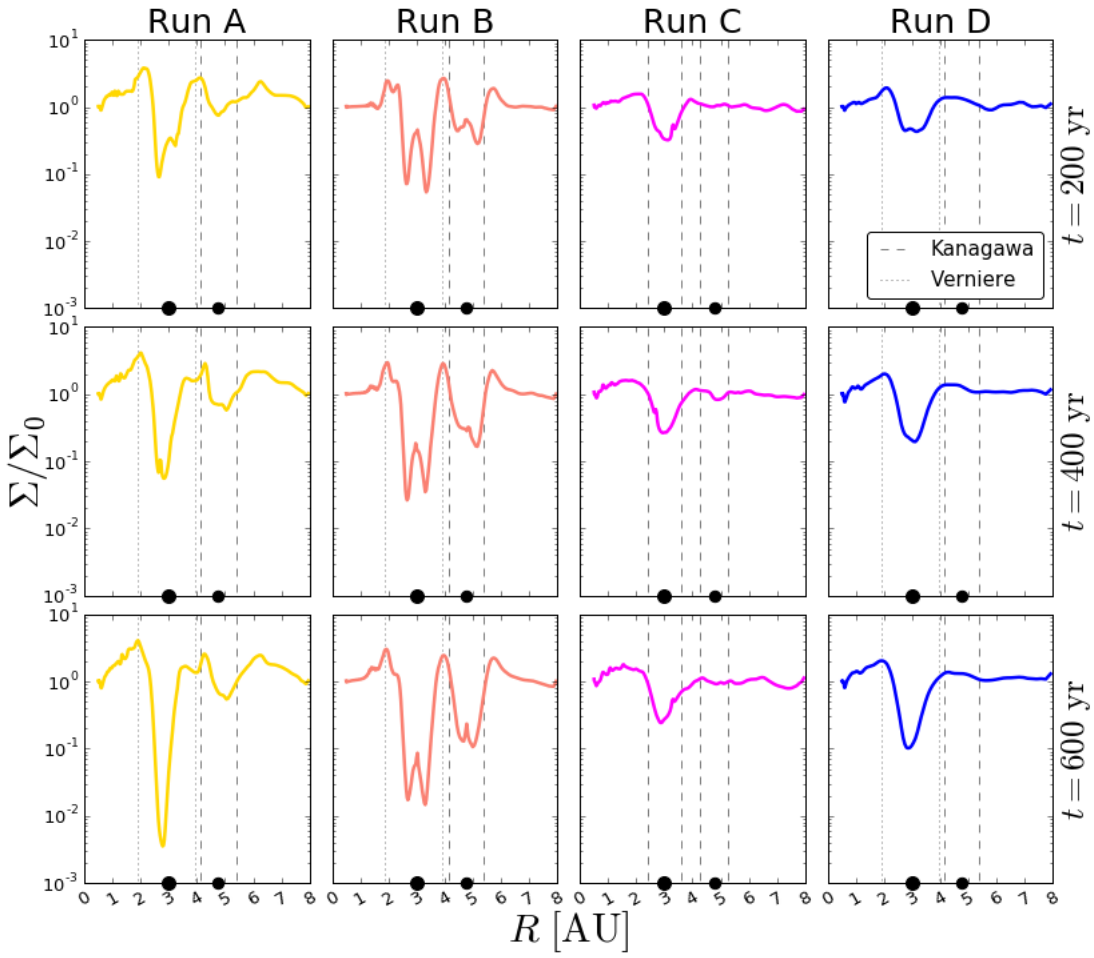

Figure 4.1: Gas surface density profile normalised to the initial value. The density is plotted as a function of the cylindrical radius R. The black dots represent the semi-major axes of the planets. The vertical lines represent the gap boundaries according to Varnière et al. 2004 or Kanagawa et al. 2016 , depending on the value of $(m_\mathrm{p}/M_*)^2 (H_\mathrm{p}/r_\mathrm{p})^{-2} \alpha^{-1}$. From *left* to *right*: run A, B, C, D. From *top* to *bottom*: $t = 200, 400$ and 600 years.

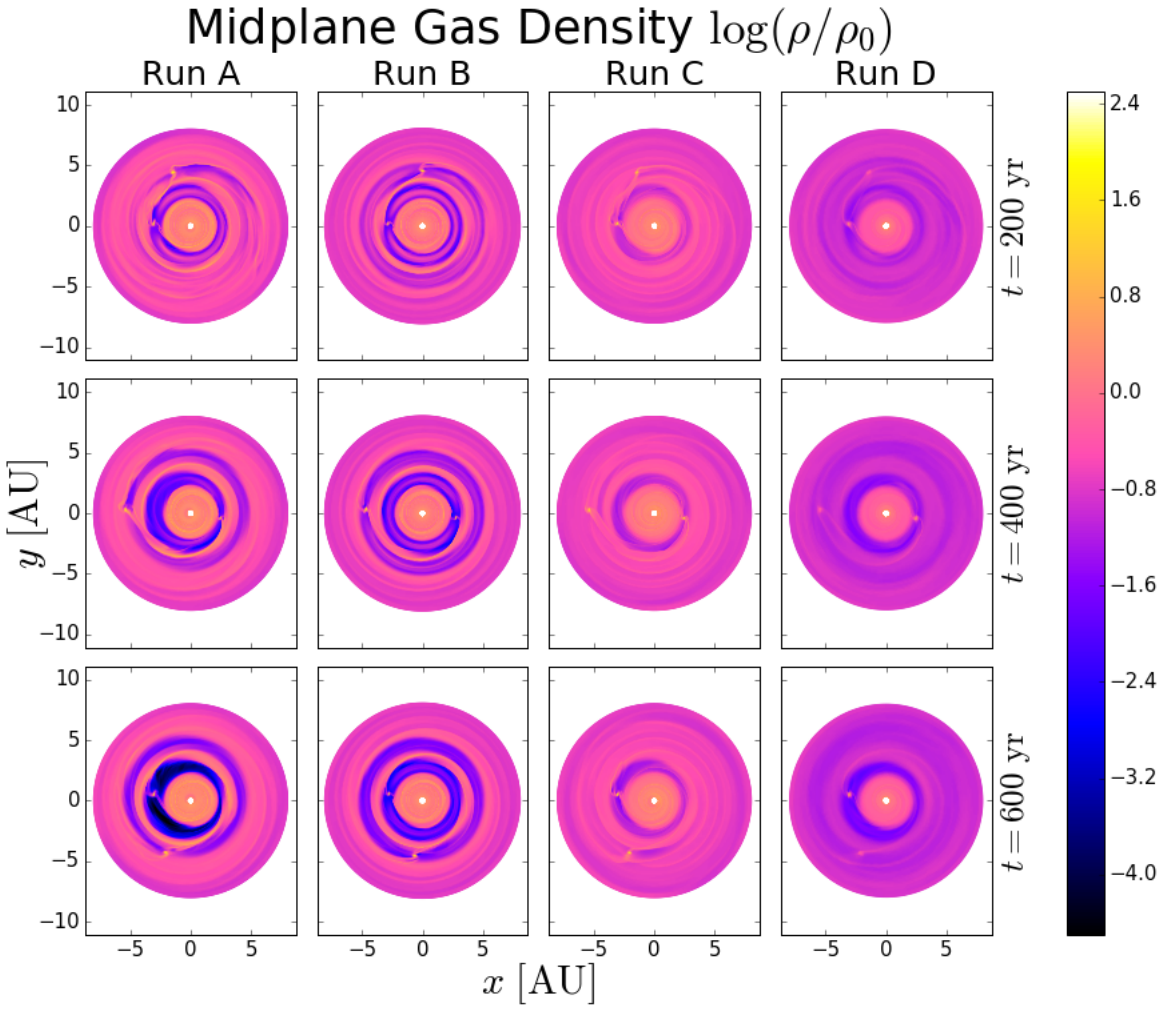

Figure 4.2: Midplane gas density normalised to the initial value in a decimal logarithmic scale. The density is represented by the colormap as a function of the x and y coordinates. From *left* to *right*: run A, B, C, D. From *top* to *bottom*: $t = 200, 400$ and 600 years.

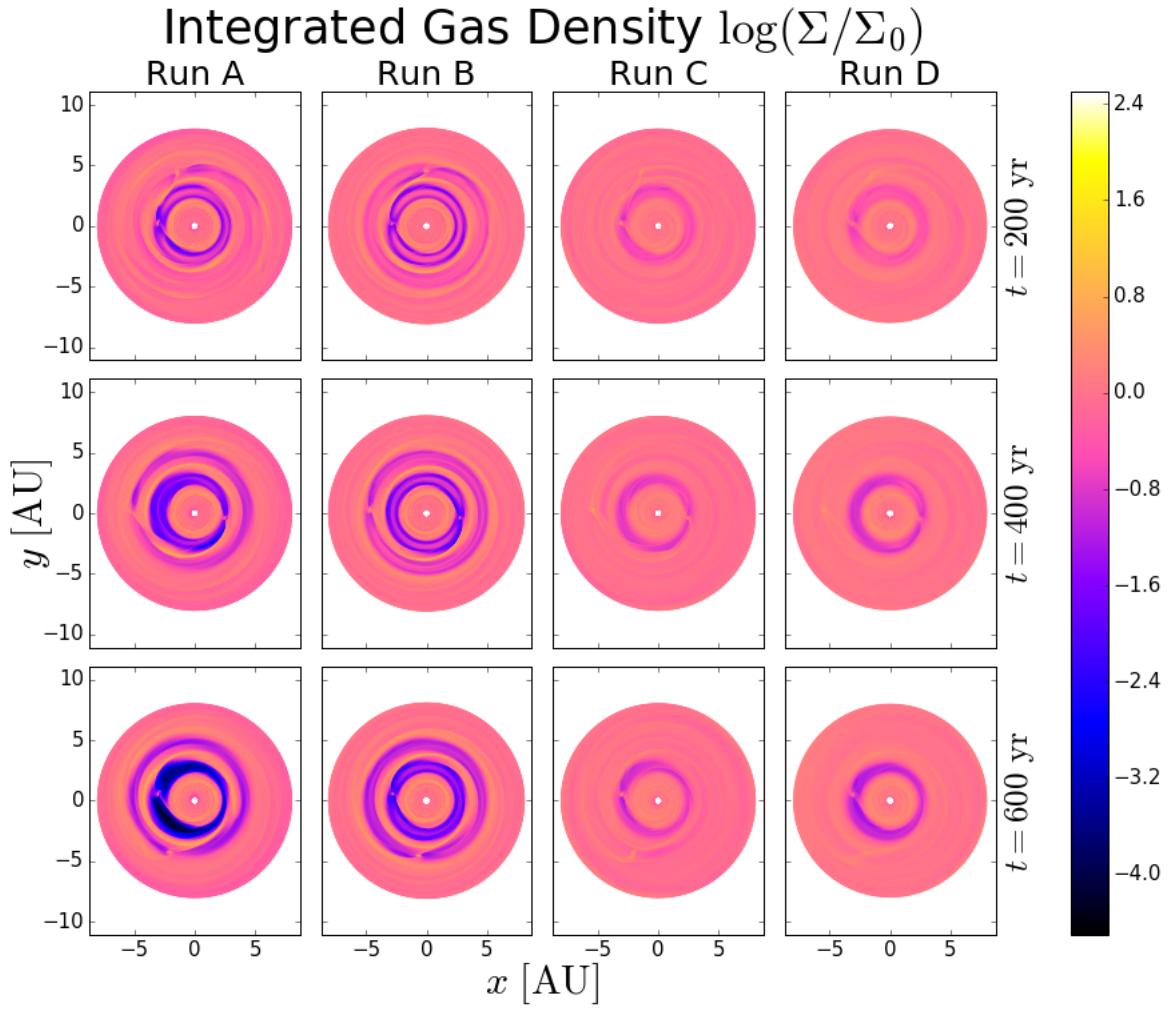

Figure 4.3: Surface gas density integrated along the z-axis normalised to the initial value in a decimal logarithmic scale. The density is represented by the colormap as a function of the x and y coordinates. From *left* to *right*: run A, B, C, D. From *top* to *bottom*: $t = 200, 400$ and 600 years.

where K is a dimensionless parameter defined by

$$K \equiv \left(\frac{m_\mathrm{p}}{M_*}\right)^2 \left(\frac{H_\mathrm{p}}{r_\mathrm{p}}\right)^{-5} \alpha^{-1}, \tag{4.3}$$

where m_p, M_*, r_p, H_p and α are the masses of the planet and the central star, the orbital radius of the planet, the scale height at the location of the planet and the viscous parameter. Varnière et al. 2004 found that for values of

$$\left(\frac{m_\mathrm{p}}{M_*}\right)^2 \left(\frac{H_\mathrm{p}}{r_\mathrm{p}}\right)^{-2} \alpha^{-1} \gtrsim 0.3 \tag{4.4}$$

the gap edges roughly correspond to the locations of the $m = 2$ Lindblad resonances. For smaller values, Kanagawa et al. 2016 found a relation for the gas width:

$$\frac{\Delta_\mathrm{gap}}{r_\mathrm{p}} = 0.41 K'^{1/4} \tag{4.5}$$

where K' is another dimensionless parameter

$$K' \equiv \left(\frac{m_\mathrm{p}}{M_*}\right)^2 \left(\frac{H_\mathrm{p}}{r_\mathrm{p}}\right)^{-3} \alpha^{-1}. \tag{4.6}$$

The only case where the gap width must be computed with Equation 4.4 is relative to the gap formed by the most massive planet in the discs where $H/R = 0.02$. According to Kanagawa et al. 2016 the time required to obtain a steady gap is of the order of $\sim 10^4$ planetary orbits, so these simulations are not adequate for a proper estimate of these parameters. However, the different shapes of gaps obtained in the four runs allow to have an idea of the behaviour of these quantities as a function of the different initial conditions. The challenges for the gap evaluation in my simulations include the fact that the aforementioned estimates refer to single planets on circular orbits: this means the effects of the presence of another planet and of their orbits' eccentricities are neglected, therefore the possibility of the formation of a common gap is not considered. Furthermore, the values from literature are referred to simulations run in two dimensions: the addition of a third dimension surely affects these estimates. From what can be seen in the plots, it is clear that the four setups lead to very different outcomes in terms of the shape of the gaps (Figure 4.1). Run B, the setup with the circular orbits, shows quite regular gaps that maintain their initial shape and width and increase their depth with time: in the middle of the gap there is some material that cannot be swept away by the planet at the location of the horseshoe orbits. Run A's gaps do not have a classical 'U' shape in the surface density profile due to the eccentricities of the planets that break the axis-symmetry of the disc: the inner planet carves a gap that is deeper and wider near the planets' apocentres (Figures 4.2, 4.3) and the horseshoe gas is no longer present. Run C, with the higher aspect ratio, shows that the gap for the inner planet is less easily formed, both in the midplane density and in the integrated surface density, while the outer planet hardly shows signs of gap formation. In run D, where radiative effects were considered, the gaps are

visible in the midplane: however, it can be noticed that the whole disc tends to move towards higher z, since the midplane has mostly negative values of $\log \rho/\rho_0$, while the integrated density distribution remains globally constant. The inner planet's gap is much less deep compared to the surface density profile of the isothermal case, while the outer planet does not show any recognisable feature at all. The values found for the gap width are compatible with the ones found in literature. In particular, run B is the most easily comparable to the predictions, since the orbits are circular and the interaction between the gaps is reduced. As for the depths, some of the ones obtained in the simulations (Figure 4.4) are significantly less prominent than the predicted values: as previously mentioned, those are referred to a steady gap, which would require $\sim 10^5$ years for this planetary system. The formation of a common gap needs the peaked density in-between the two gaps to lower: considering the simulations where the two gaps are well defined, A and B, the eccentric system shows a central peak that is gradually lowering faster than the circular system.

4.1.2 Gas Temperature

While run A, B and C are locally isothermal during the simulation, in run D it is possible to study the temperature evolution. PLUTO solves radiative transport inside the disc as a function of the radiation energy density, i.e. the radiant energy per unit volume $[\mathrm{erg\ cm^{-3}}]$. This quantity is related to the temperature through the equation

$$E = a_{\mathrm{R}} T^4 \tag{4.7}$$

with

$$a_{\mathrm{R}} = \frac{4\sigma}{c} = \frac{8\pi^5 {\mathrm{k_B}}^4}{15c^3h^3} = 7.5657 \cdot 10^{-15}\ \mathrm{erg\ cm^{-3}\ K^{-4}} \tag{4.8}$$

where σ is the Stefan–Boltzmann constant, $\mathrm{k_B}$ is the Boltzmann constant and h is the Planck constant. The initial $\propto R^{-1}$ profile with $T_0 = 100$ K at 1 AU is heavily modified by the viscous heating inside the disc. This is mostly evident in the area affected by the orbital motion of the planets. The disc reaches ~ 400 K in the midplane and ~ 200 K in the top layer: in the very proximity of the planets, the midplane gas temperature reaches ~ 700 K (Figure 4.5), while the gap zones remain cooler with averages of ~ 150 K. As it is shown by Figure 4.6, after 200 years the temperature has almost stabilised and shows a profile consistent with the theoretical midplane temperature obtained by

$$T_{\mathrm{mid}} = \left[\frac{9GM_*\dot{M}\tau}{32\pi\sigma R^3} \left(1 - \sqrt{\frac{R_*}{R}} \right) \right]^{1/4}. \tag{4.9}$$

The accretion rate for a stationary disc is

$$\dot{M} = \frac{3\pi\nu\Sigma}{1 - \sqrt{\frac{R_*}{R}}} \tag{4.10}$$

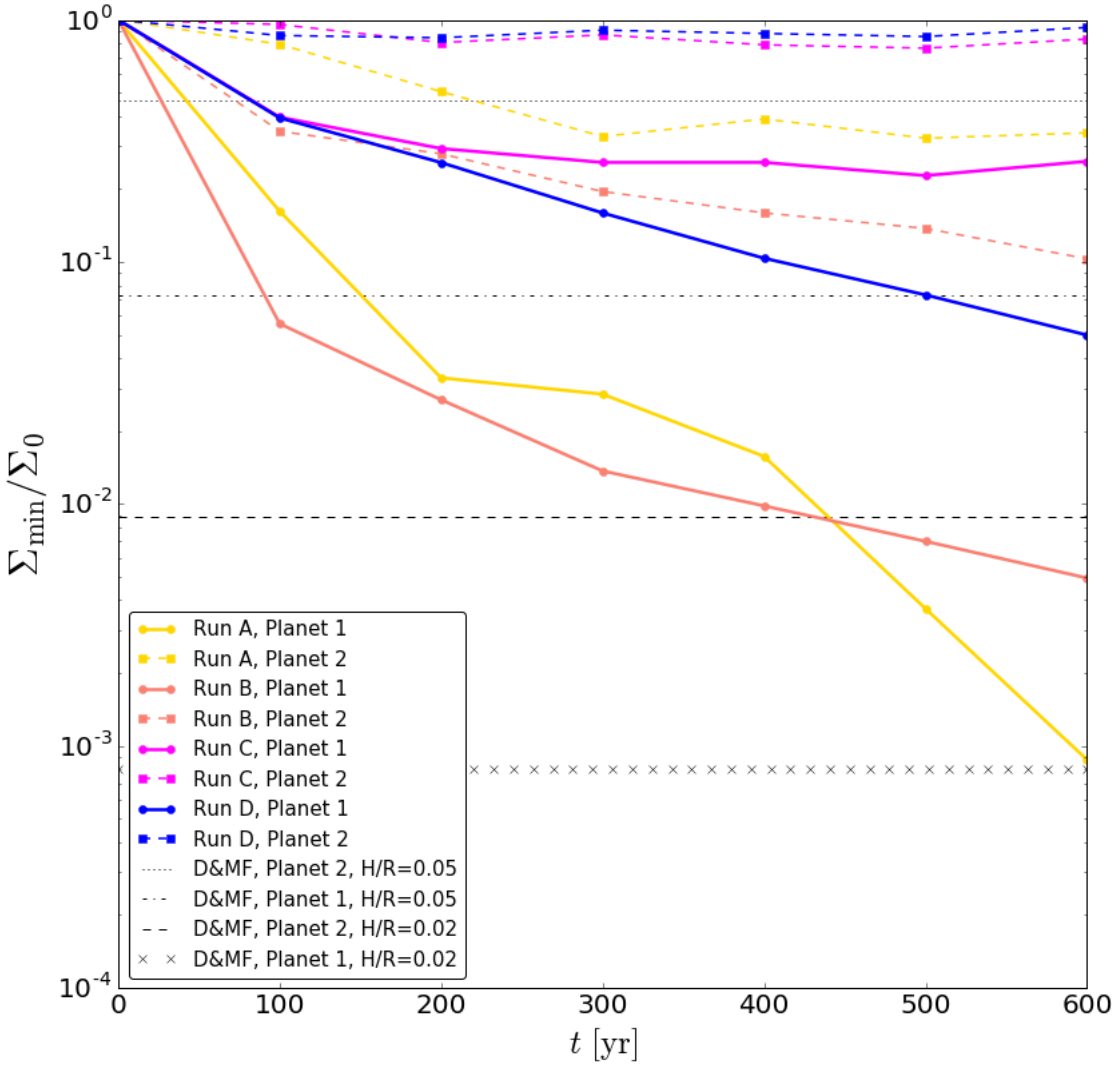

Figure 4.4: Depth of the gaseous gap for each planet in the four runs. The horizontal black lines indicate the values predicted for a steady gap by Duffell and MacFadyen 2013 for the two planet masses and the two values of the aspect ratio.

with $\nu = \alpha H^2 \Omega_{\mathrm{K}}$ viscosity, which gives a value of the order of $10^{-7}\ \mathrm{M}_\odot\ \mathrm{yr}^{-1}$ at 1 AU. The optical depth on the midplane τ depends on the Rosseland mean opacity: I chose a value of $\kappa_{\mathrm{R}} = 1\ \mathrm{cm}^2\ \mathrm{g}^{-1}$, in agreement with the results of Semenov et al. 2003, which gives $\tau = \Sigma\kappa_{\mathrm{R}} = 750$. This is consistent with the assumption of an optically thick disc for $z = 0$. The figure shows that the profile obtained is partially compatible with the theoretical temperature: the deviations are attributed to the presence of the planets and to the boundary conditions which impose cooling at the edge of the domain.

4.1.3 Scale Height

The scale height of a PPD is a parameter which describes the vertical geometric structure of a disc as a function of radius: solving the vertical hydrostatic balance equation leads to

$$\rho(R, z) = \rho_{\mathrm{mid}}(R) \exp\left(-\frac{z^2}{2H^2}\right) \tag{4.11}$$

with $H(R) = c_s/\Omega_{\mathrm{K}}$. This means that the scale height corresponds to the value of z at which the density decreases by a factor $\exp(-0.5) \approx 0.6$ with respect to the midplane density at a certain radius. This quantity is also related to the thermal structure of the disc, considering that the sound speed is a function of the temperature $c_s \propto T^{1/2}$. The initial conditions of my simulations imposed $H \propto R$, which translates into a constant aspect ratio H/R at $t = 0$. Since temperature and scale height are strictly related, it is interesting to study the aspect ratio trend in run D, where radiative transport is included. On the other hand, I expect the scale height to remain unchanged in run A, which has a locally isothermal profile and the same initial aspect ratio as D. By comparing Figures 4.2 and 4.3 it was already possible to realise that in run D the midplane layer gets gradually depleted so the material must have moved upwards to maintain the surface density constant. Figure 4.7 confirms that in run D the aspect ratio increases as a function of time especially where the planets orbit, between 3 and 5 AU, consistently to the temperature rise. In run A the aspect ratio slightly deviates from the initial value but oscillates about 0.02. As a consequence, it is possible to see that the top layer becomes significantly denser in run D (Figure 4.8).

4.1.4 Gas Velocity

In Figure 4.9 I represented the velocity components of the gas on the midplane at the end of the simulation. The radial component v_r has values very close to zero for run B, with the circular planet orbits, while for the rest of the simulations the gas acquires a non-zero eccentricity for most of the radial extent (Figure 4.10) and thus the gas shows motion along r. In the polar direction, the velocities v_θ are almost null for all simulations. The azimuthal component v_ϕ is faithful to the Keplerian velocity (Equation 1.2).

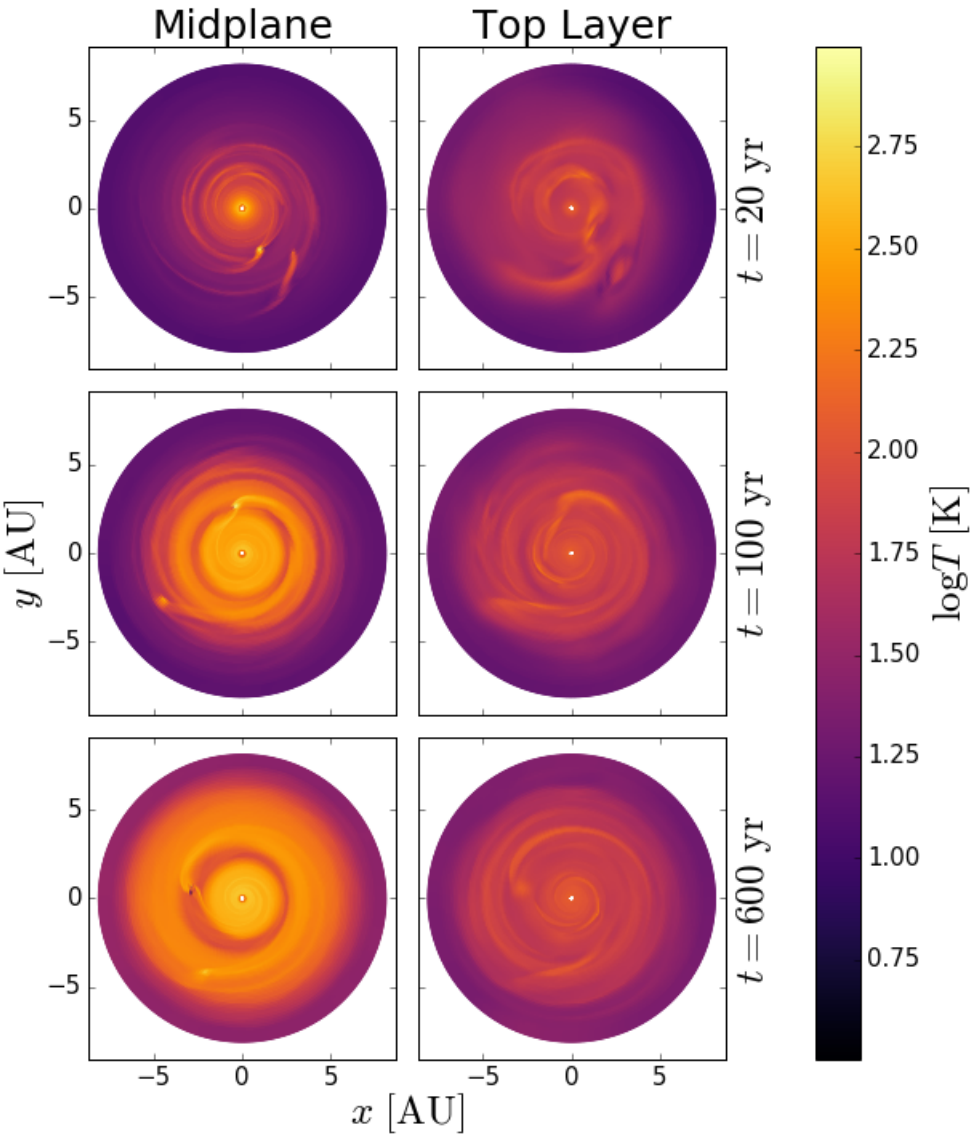

Figure 4.5: Gas temperature distribution for the radiative run D represented by the colormap as a function of the x and y coordinates in a decimal logarithmic scale. *Left* panels: temperature distribution on the midplane. *Right* panels: temperature distribution on the top layer ($\theta = 82°$). From *top* to *bottom*: $t = 20, 100$ and 600 years.

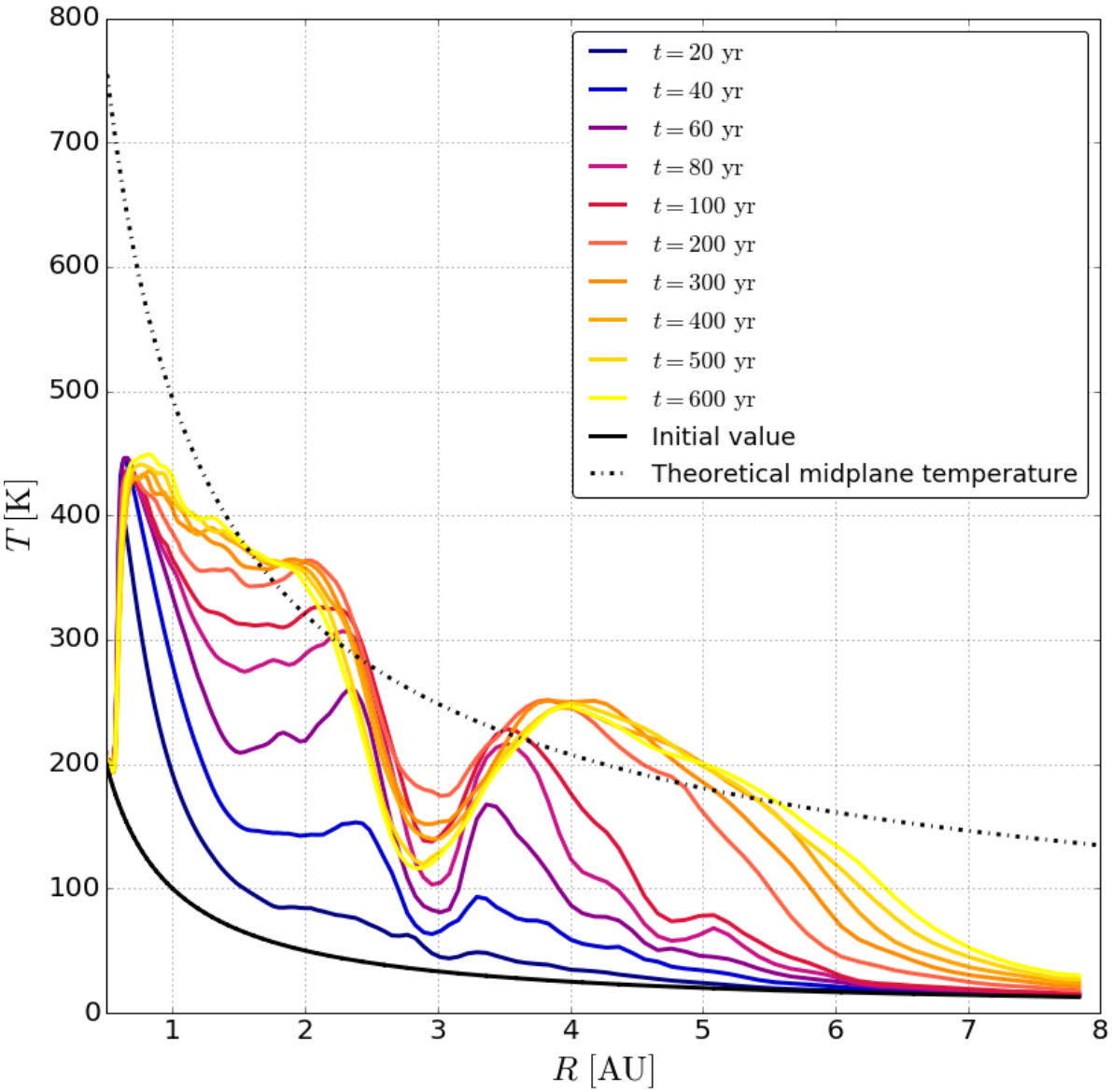

Figure 4.6: Gas temperature profile of the midplane for the radiative run D as a function of R, averaged on the ϕ coordinate. The continuous black line represents the initial profile, while different colors represent different ages. The dash-dotted line indicates the theoretical value of the midplane temperature.

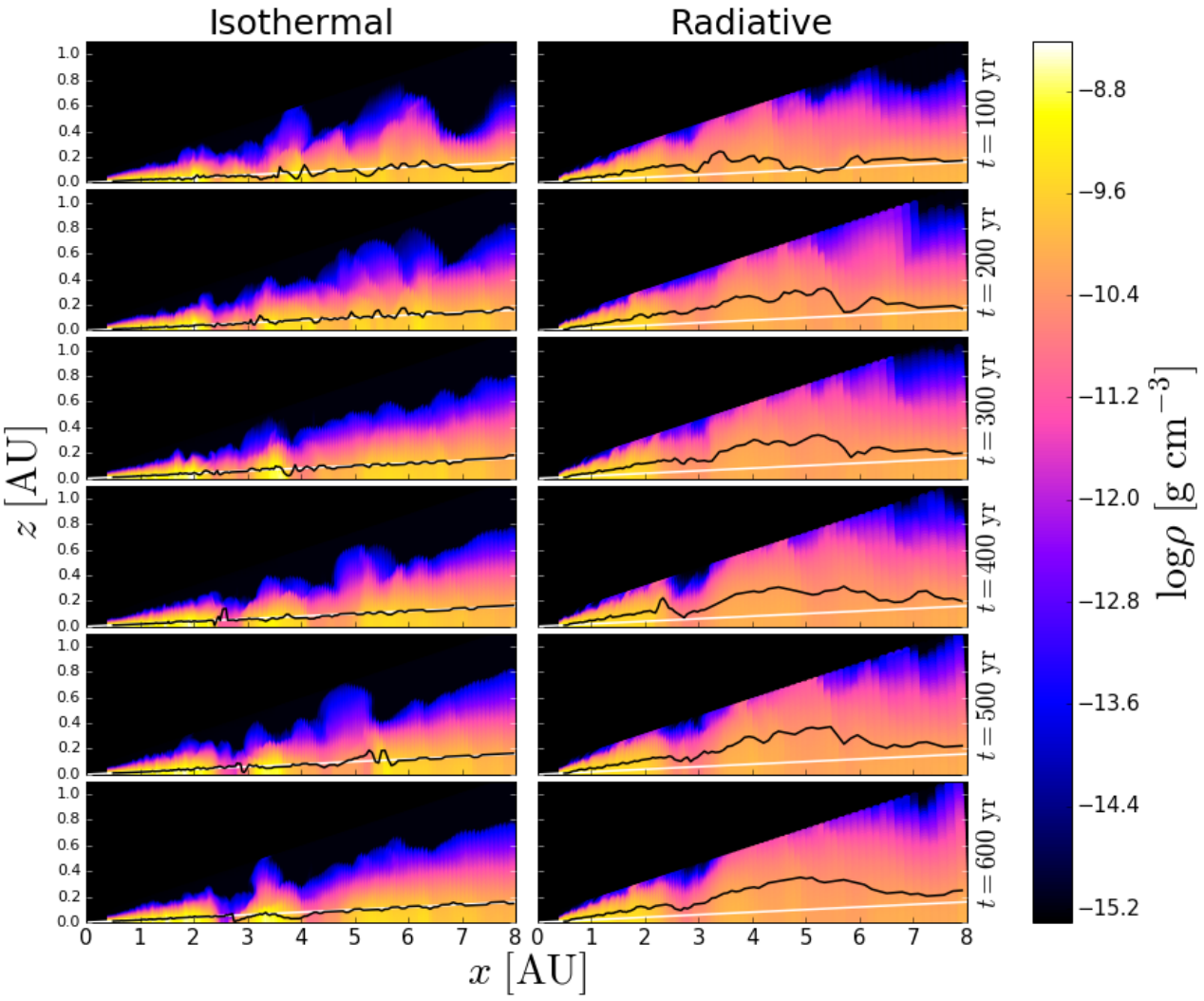

Figure 4.7: Scale height evolution in a slice of gas for the radiative run D. The density is represented by the colormap as a function of the radius and the z coordinate at $\phi = 0$ in a decimal logarithmic scale. The white line corresponds to the initial scale height, i.e. it is the line of equation $z = 0.02R$. The black line connects the points for each R where $\rho(R, z) = \rho(R)_{\mathrm{mid}} \exp(-1/2)$. *Left* panels: run A; *right* panels: run D. From *top* to *bottom*: $t = 100, 200, 300, 400, 500$ and 600 years.

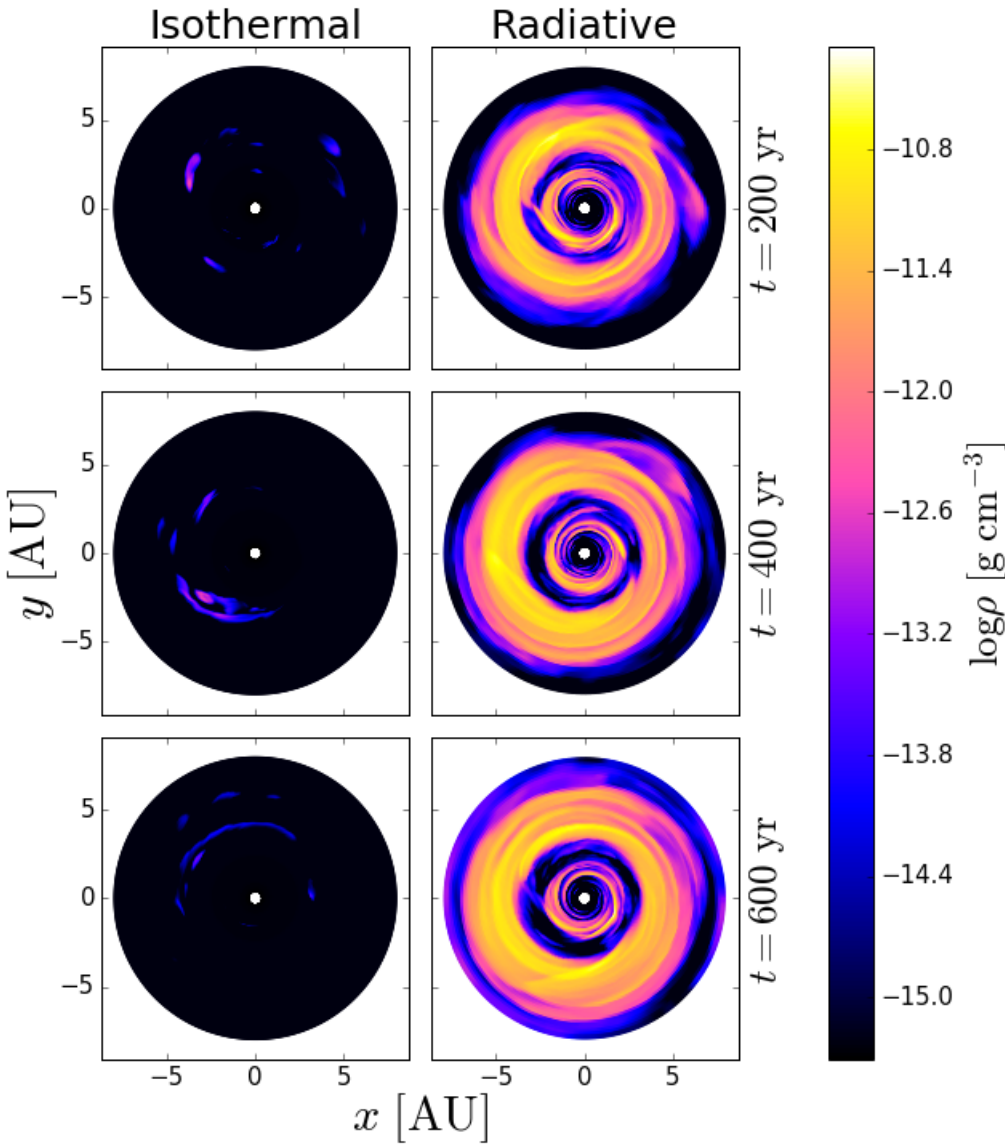

Figure 4.8: Gas density distribution on the top layer ($\theta = 82°$) represented by the colormap as a function of the x and y coordinates in a decimal logarithmic scale. *Left* panels: run A; *right* panels: run D. From *top* to *bottom*: $t = 200, 400$ and 600 years.

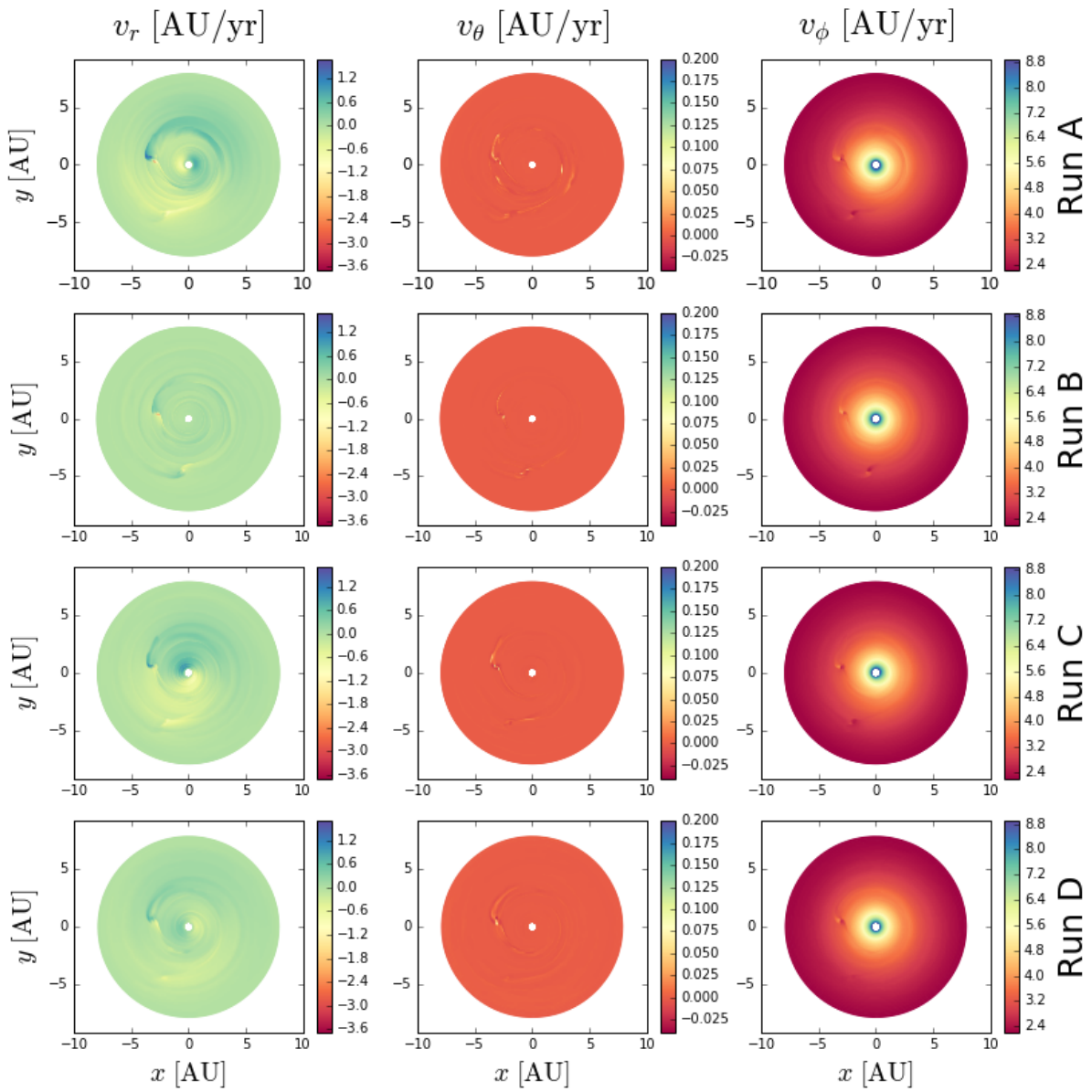

Figure 4.9: Midplane velocity distribution in r, θ and ϕ directions after 600 years. From *left* to *right*: v_r, v_θ and v_ϕ. From *top* to *bottom*: runs A, B, C and D.

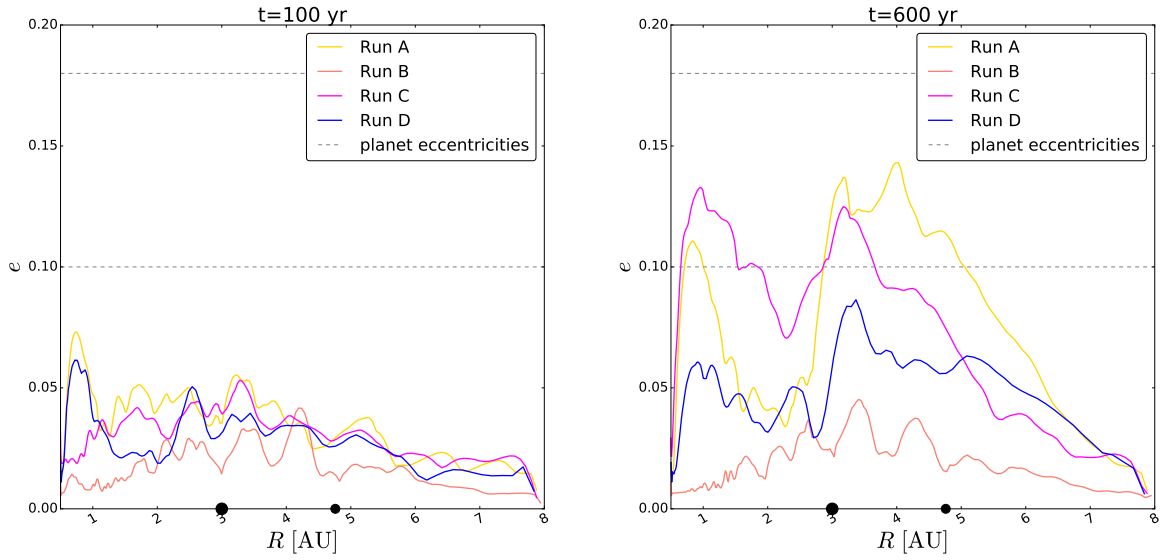

Figure 4.10: Midplane gas eccentricity distribution averaged over all ϕ for the four simulations after 100 (*left*) and 600 (*right*) years as a function of R. The dashed lines indicate the eccentricity of the planets.

4.2 Dust Component

Observations of PPDs probe mostly the dust content of the disc, instead of the gas: the two phases are not necessarily coupled and may show different features in their distribution. The primary effect which may introduce differences in gas and dust evolution is the drag between the two fluids due to the fact that gas is partially supported against gravity by the pressure gradient and rotates more slowly than the Keplerian value.

4.2.1 Dust Gap

A planet can open a gap in the dust disc even if the gas gap is not fully shaped yet (e.g. Paardekooper and Mellema 2004, Fouchet et al. 2010, Zhu et al. 2014, Picogna and Kley 2015, Dipierro et al. 2015). Gap opening is more effective in the dust since it is considered to be an almost collisionless fluid and there are no intrinsic pressure and viscosity able to close the gap. In Figure 4.11 I plotted the dust density profiles at different times, while Figure 4.12 shows the distribution at the end of the simulation for the different gran sizes. In Figure 4.11 I removed the particles inside the Hill sphere of the planet since they would interfere with the profile of the gap by showing a peaked feature at the planets' positions. Analogously to the gas gap, runs A to D show very different features. The gaps are more easily carved in the isothermal runs with $H/R = 0.02$ (A and B): the gap of the inner planet is clearer for the elliptical case while the opposite happens for the less massive planet; the eccentric orbit in run A facilitates the removal of dust material inside the primary gap but perturbs the formation of the outer gap which remains rather irregular. The barrier between the two gaps is less high in run A and

is more likely to lower towards the formation of a common gap. In runs C and D there is no trace of a second gap forming, as noticed for the gas. There is no obvious difference in the behaviour of the particles of different dimension, except for a slight increase in the depth of the gap for larger grain radii: although the Stokes numbers span several orders of magnitude, the quite elevated value of the viscosity parameter $\alpha = 0.01$ has a smoothing action and the majority of the particles with $\mathrm{St} < 1$ are well coupled to the gas and thus show analogous dynamics. Some of the $1\ \mathrm{cm}$ particles, with the highest Stokes number, deviate from the global trend and tend to carve a deeper gap in the low density zones, since they are less coupled to the gas and more 'free' to pile up at the pressure maxima.

4.2.2 Dust Eccentricity

The shape of the dust disc, hence the particles' eccentricities, may have a crucial role in the early stages of planetary formation, where planetesimals are potentially prone to collide.

To obtain the orbital elements I have performed a transformation starting from the Cartesian state vectors, assuming that the motion of each dust particle is purely Keplerian, so I treated the system as a two-body problem. Knowing that $\mathbf{v} = \dot{r}\hat{\mathbf{r}} + r\dot{\theta}\hat{\boldsymbol{\theta}} + r\sin\theta\dot{\phi}\hat{\boldsymbol{\phi}}$ and $\mathbf{h} = \mathbf{r} \wedge \mathbf{v}$, the conservation of energy and angular momentum leads to

$$\frac{1}{2}v^2 - \frac{\mu}{r} = -\frac{\mu}{2a} \tag{4.12}$$

and

$$h = \sqrt{\mu a(1-e^2)}, \tag{4.13}$$

which allow to calculate the semi-major axis a and the eccentricity e of each particle.

The eccentricity of the dust grains is affected by the planetary orbits (Figure 4.13): run B has values of e closer to zero since the planets are on circular orbits. In runs A, C and D the eccentricities approach the ones of the planets between approximately 3 and $5\ \mathrm{AU}$, more clearly for dust rather than gas. The radiative disc in run D shows less prominent eccentricities in both gas and dust, as was found by Marzari et al. 2012. There are no noticeable differences between the eccentricity distribution for the various grain size.

In the zones surrounding the planets, dust particles get scattered on orbits of higher eccentricities (Figure 4.14) following trajectories that respect the conservation of the *Tisserand parameter* for each particle (Tisserand 1896), which is obtained starting from the integrals of motion of the restricted circular planar three body problem:

$$T = \frac{a_\mathrm{p}}{a} + 2\sqrt{\frac{(1-e^2)a}{a_\mathrm{p}}}\cos i \tag{4.14}$$

where a, e and i are the particle's semi-major axis, eccentricity and inclination and a_p is the planet's semi-major axis. It is possible to neglect the inclination of the particle, which must be below 0.14 due to the limits imposed on the domain, giving values of $0.99 \lesssim \cos i \leq 1$.

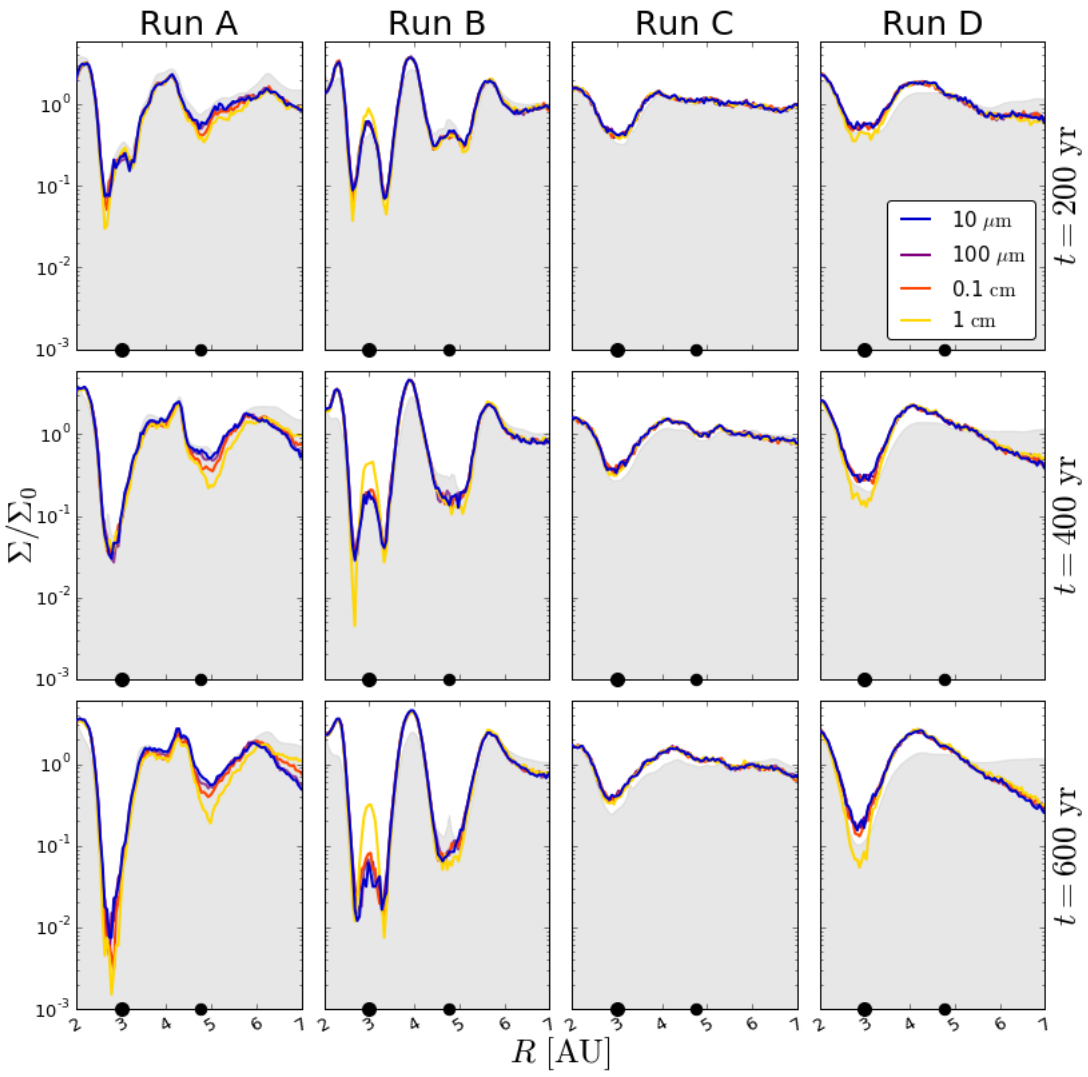

Figure 4.11: Surface density profile of the gas and dust particles at different times as a function of R in the proximity of the planets normalised to the initial profile. Particles inside the Hill sphere of the planets were removed from the plot. Different colors indicate particles of different size, while the gray fill represents the gas profile. From *left* to *right*: runs A, B, C and D. From *top* to *bottom*: $t = 200, 400, 600$ years.

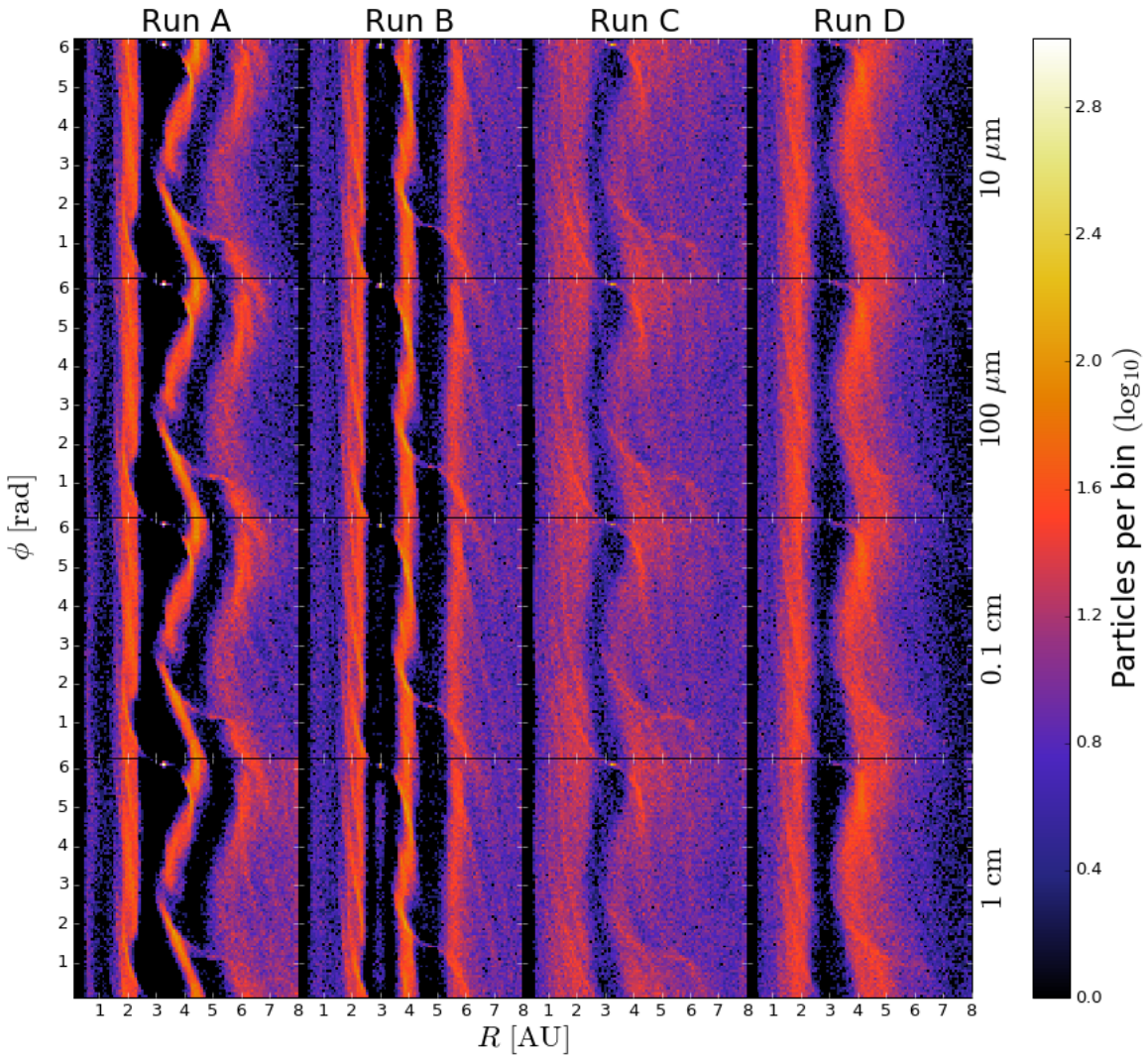

Figure 4.12: Surface density distribution of the dust particles after 600 years for the different grain sizes and setups as a function of the azimuthal angle ϕ and the cylindrical radius R. Each radial bin corresponds to 0.08 AU, while each azimuthal bin corresponds to $2\pi/100$ rad. From *left* to *right*: runs A, B, C and D. From *top* to *bottom*: particles with radii of 10 μm, 100 μm, 0.1 cm and 1 cm.

In runs C and D, this effect is reduced, compatibly with the fact that a less deep gap is carved and gas has a damping action on the eccentricities; planets in run D scatter particles even less, due to the fact that the bulk of the gas rises in height and less particles are in the influence zone of the planets, as will be shown in Section 4.2.5.

4.2.3 Radial Drift

A consequence of aerodynamic drag is the phenomenon of radial drift, which acts on a wide range of Stokes numbers. Large bodies with $\mathrm{St} \gg 1$ orbit at Keplerian speed and the gas flow acts as a 'headwind' and therefore introduces a radial motion that causes the orbit to decay at lower radii. Small particles with $\mathrm{St} \ll 1$ are aerodynamically coupled to the gas and forced to orbit at the gas speed: since the particles do not experience the pressure gradient, their non-Keplerian orbital motion translates into a net radial force. The final expression for the radial velocity is given by (see Section 1.2.1.1)

$$v_{\mathrm{drift},r} \simeq -\frac{2}{\mathrm{St} + \mathrm{St}^{-1}} \eta v_{\mathrm{K}}. \tag{4.15}$$

In Figure 4.15 I plotted the Stokes numbers of each grain size after 600 years: the distribution follows the gas surface density profile as in Figure 4.1. For the isothermal run, where the density drops quickly after a few scale heights, the distribution of St shows a cutoff around $z = 0.5$ that is not present for the radiative run in which the gas rises (Figure 4.7) and maintains quite high values even at large z, so St remains below unity for the great majority of the particles. In Figure 4.16 I plotted the theoretical drift velocities of each grain size obtained from Equation 4.15 with the Stokes numbers in Figure 4.15 after 600 years: for the same reasons as before, drift velocities are globally very modest, but increase for the isothermal run at larger z and R. Since these values are estimated for a system in equilibrium and unperturbed by planets, it was not possible to obtain a match with the simulated dust: particles are subject to non-stationary motions induced by the planets and their semi-major axis and eccentricity undergo major changes which conceal the effect of the radial drift (Figure 4.17). Furthermore, the simulated discs are limited in radial extent which prevents to analyse an area unaffected by the planets. The variation of the particles' semi-major axes is displayed in figure 4.18: in the first hundred years the dust is largely rearranged, while the distribution becomes more stationary towards the end of the simulation.

4.2.4 Dust Settling

The gas component above the midplane is supported against the vertical component of stellar gravity by the vertical pressure gradient. Solid particles however accelerate towards the midplane until the stellar force is balanced by drag. The dust settling velocity is given by

$$v_{\mathrm{settle}} = \frac{\rho_{\mathrm{s}}}{\rho_g} \frac{s}{v_{\mathrm{th}}} \Omega_{\mathrm{K}}^2 z \tag{4.16}$$

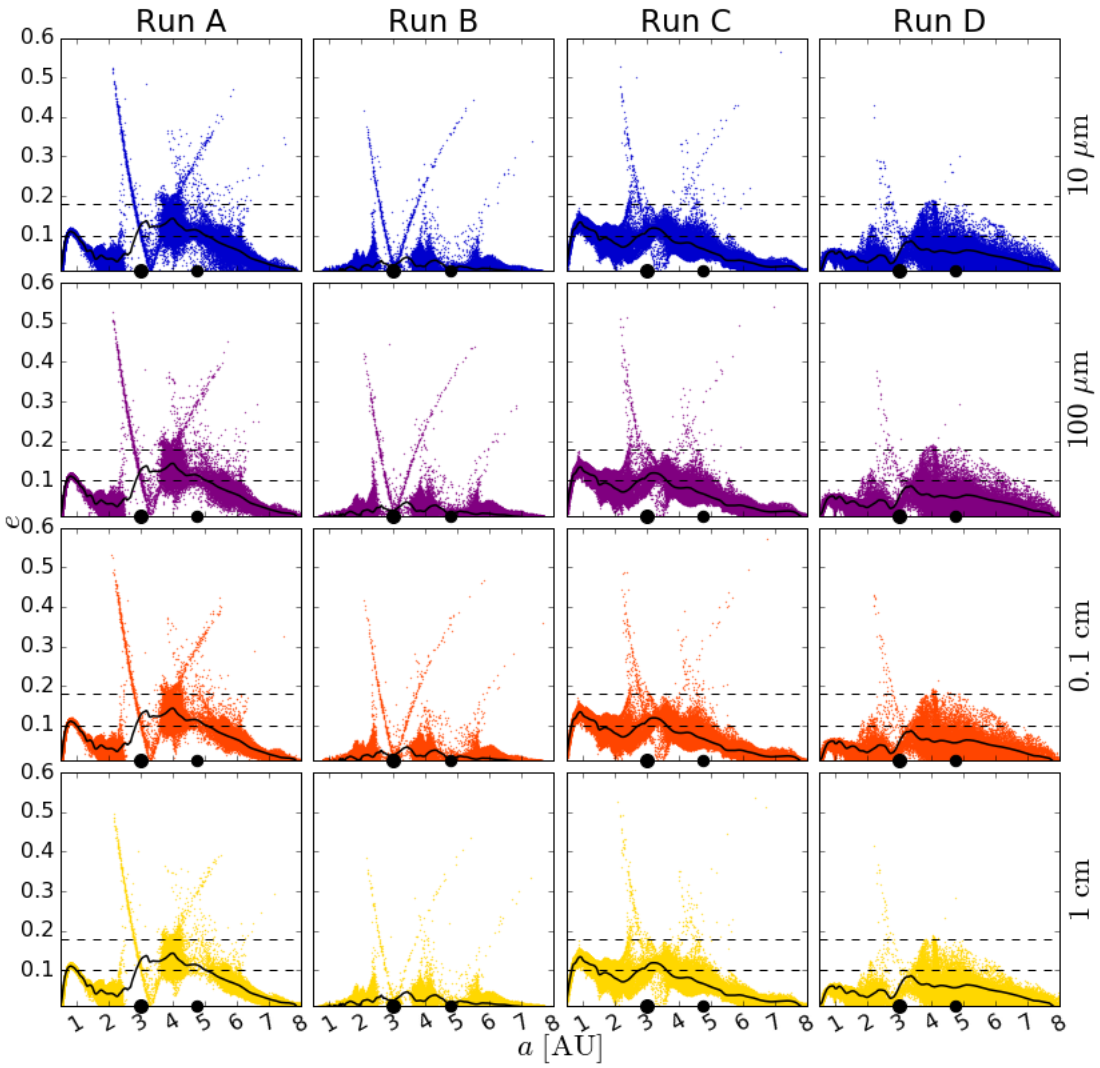

Figure 4.13: Dust eccentricity distribution as a function of the semi-major axis after 600 years for the different grain sizes and setups. The semi-major axes of the planets are represented by black dots, while their eccentricities are represented by horizontal dashed lines: in run B the eccentricities are null. The black line represents the eccentricity profile of the gas on the midplane. From *left* to *right*: runs A, B, C and D. From *top* to *bottom*: particles with radii of $10\ \mu\mathrm{m}$, $100\ \mu\mathrm{m}$, $0.1\ \mathrm{cm}$ and $1\ \mathrm{cm}$.

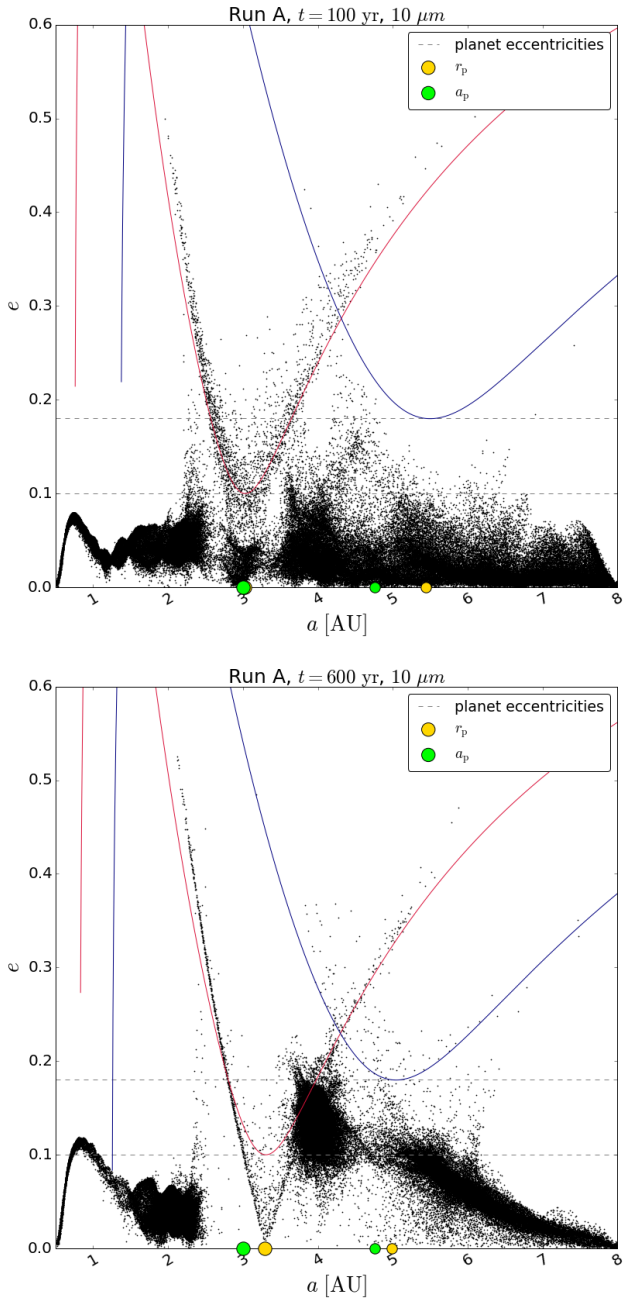

Figure 4.14: Example of the dust eccentricity distribution as a function of the semi-major axis in run A after 100 (*top*) and 600 (*bottom*) years for particles of 10 μm. The dashed lines indicate the eccentricities of the two planets (the less massive is the most eccentric); green dots indicate the semi-major axes of the planets; the yellow dots indicate the radii of the planets at the specific epoch; the blue and red lines represent the points at constant Tisserand parameter assuming that before being scattered the particles have the same semi-major axes and eccentricities as the corresponding planet.

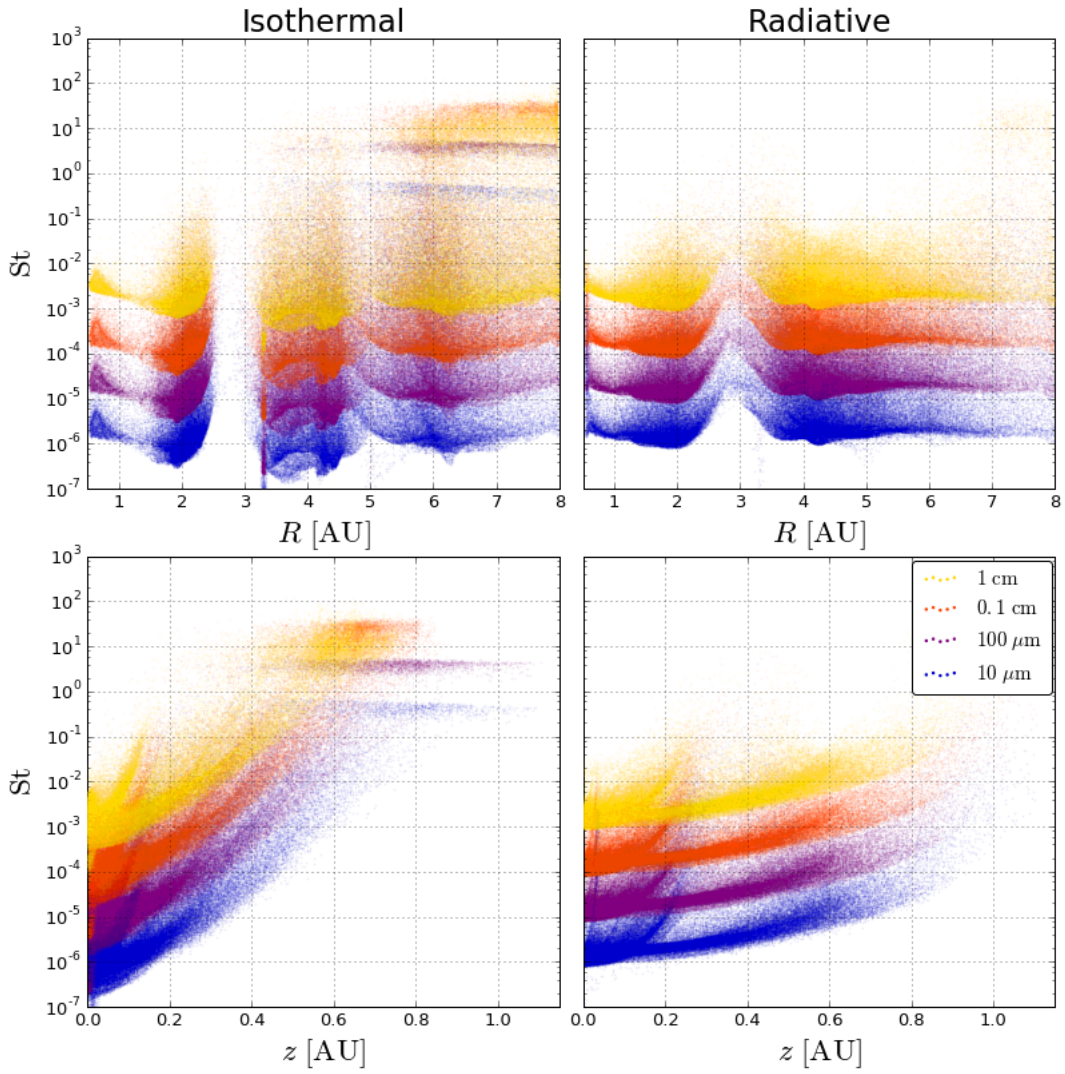

Figure 4.15: Stokes numbers for particles with radii of $10\ \mu\mathrm{m}$, $100\ \mu\mathrm{m}$, $0.1\ \mathrm{cm}$ and $1\ \mathrm{cm}$ at $t = 600\ \mathrm{yr}$ as a function of R and z. *Left* panels: run A; *right* panels: run D.

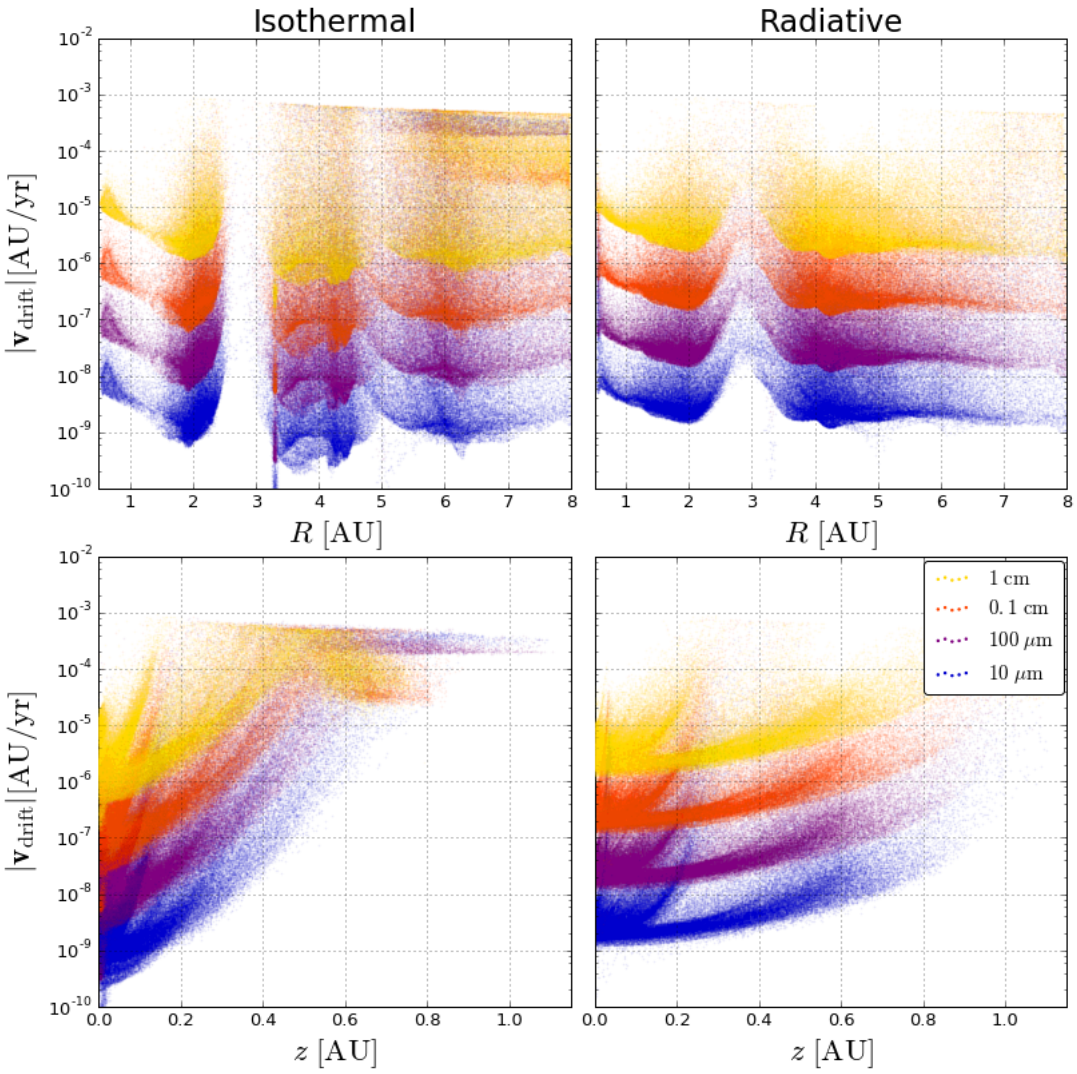

Figure 4.16: Theoretical drift velocities for particles with radii of $10\ \mu\mathrm{m}$, $100\ \mu\mathrm{m}$, $0.1\ \mathrm{cm}$ and $1\ \mathrm{cm}$ at $t\ =\ 600\ \mathrm{yr}$ as a function of R and z. *Left* panels: run A; *right* panels: run D.

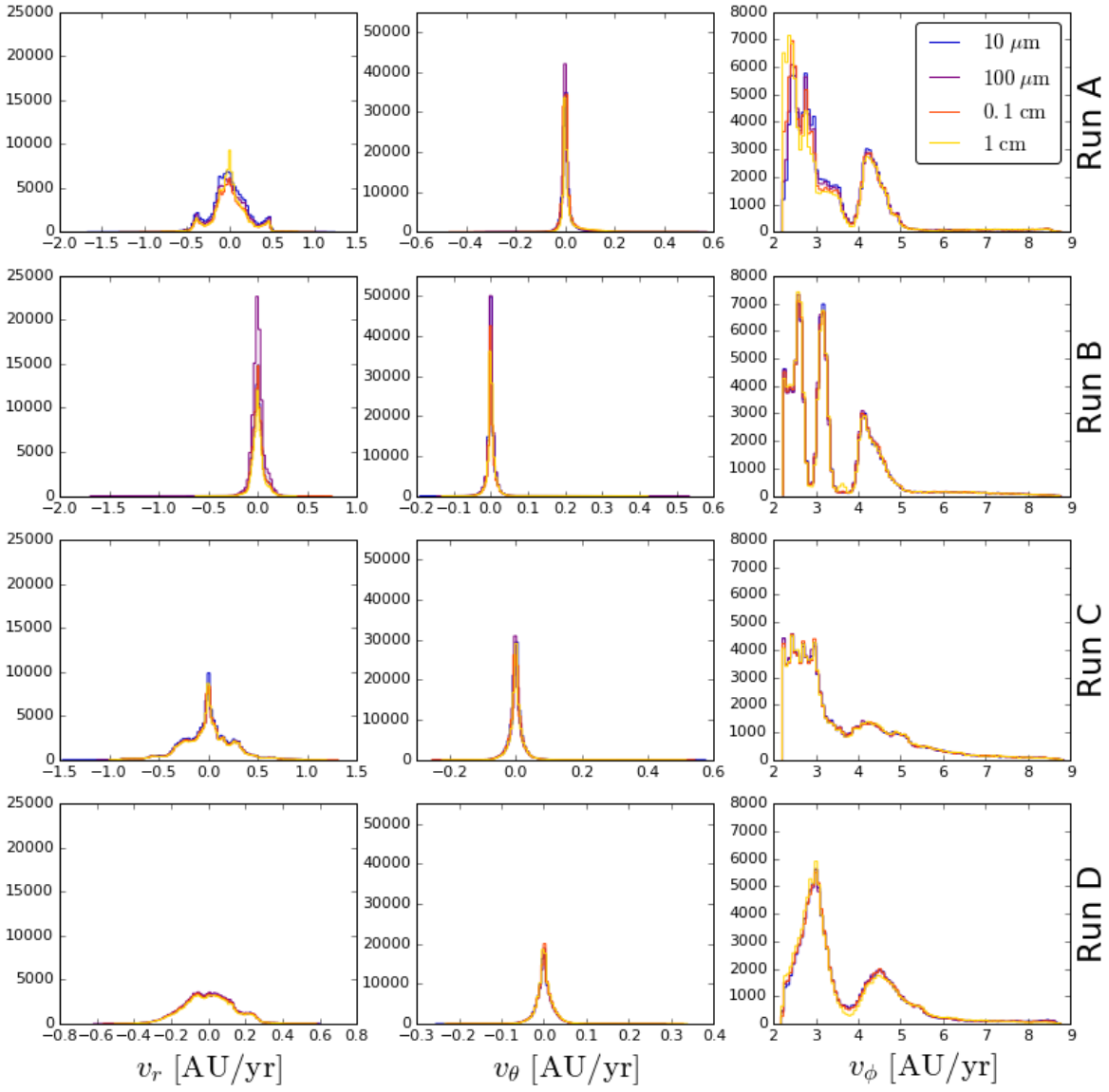

Figure 4.17: Histograms of the dust velocity distribution after 600 years for the four simulations and four grain sizes. The total number of particles for each dimension is 10^5, divided into 100 bins. From *left* to *right*: v_r, v_θ and v_ϕ. From *top* to *bottom*: runs A, B, C and D.

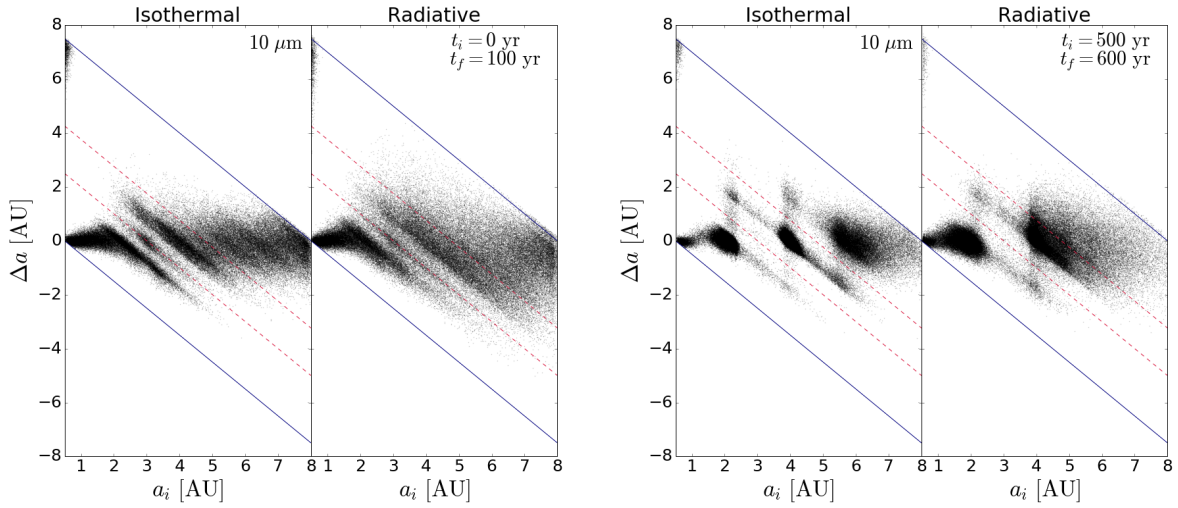

Figure 4.18: Variation of the semi-major axis of the dust particles (here, as an example, the ones with $10\ \mu\mathrm{m}$ radius) as a function of the initial semi-major axis for runs A and D: from the beginning to 100 years on the *left* and from 500 to 600 years on the *right*. The boundaries of the disc are indicated with a blue continuous line, while the positions of the planets are indicated with red dashed lines. The particles with initial a very close to the star that escape the domain are re-inserted from the outer disc to maintain the total number of particles.

which results in a settling time equal to

$$t_{\mathrm{settle}} = \frac{z}{v_{\mathrm{settle}}} = \frac{1}{\mathrm{St}\Omega_{\mathrm{K}}}. \tag{4.17}$$

However, the effect of the turbulence in discs is to counteract the tendency of dust particles to settle towards the midplane and it leads to a vertical spreading of the particles instead. The predicted settling times obtained with 4.17 for the dust particles at 600 years are represented in Figure 4.19 for the isothermal and radiative runs. Since the distribution depends on the Stokes number, the features of the plot are justified by the same reasons of Figure 4.15: particles in low-density zones have higher settling velocities and thus settle more rapidly. However the system is not in a steady state yet and the random motions (Figure 4.17) still prevail over the settling speed. Nonetheless, it is possible to gather a hint of the settling of the biggest particles at high z (Figure 4.20).

4.2.5 Captured Dust

If the star-planet-particle were an isolated three-body system, every dust particle falling into the Hill sphere (Equation 1.74) of a planet would not be able to leave and would be considered captured by the planet's gravitational field. However, there are several factors that prevent this system from being

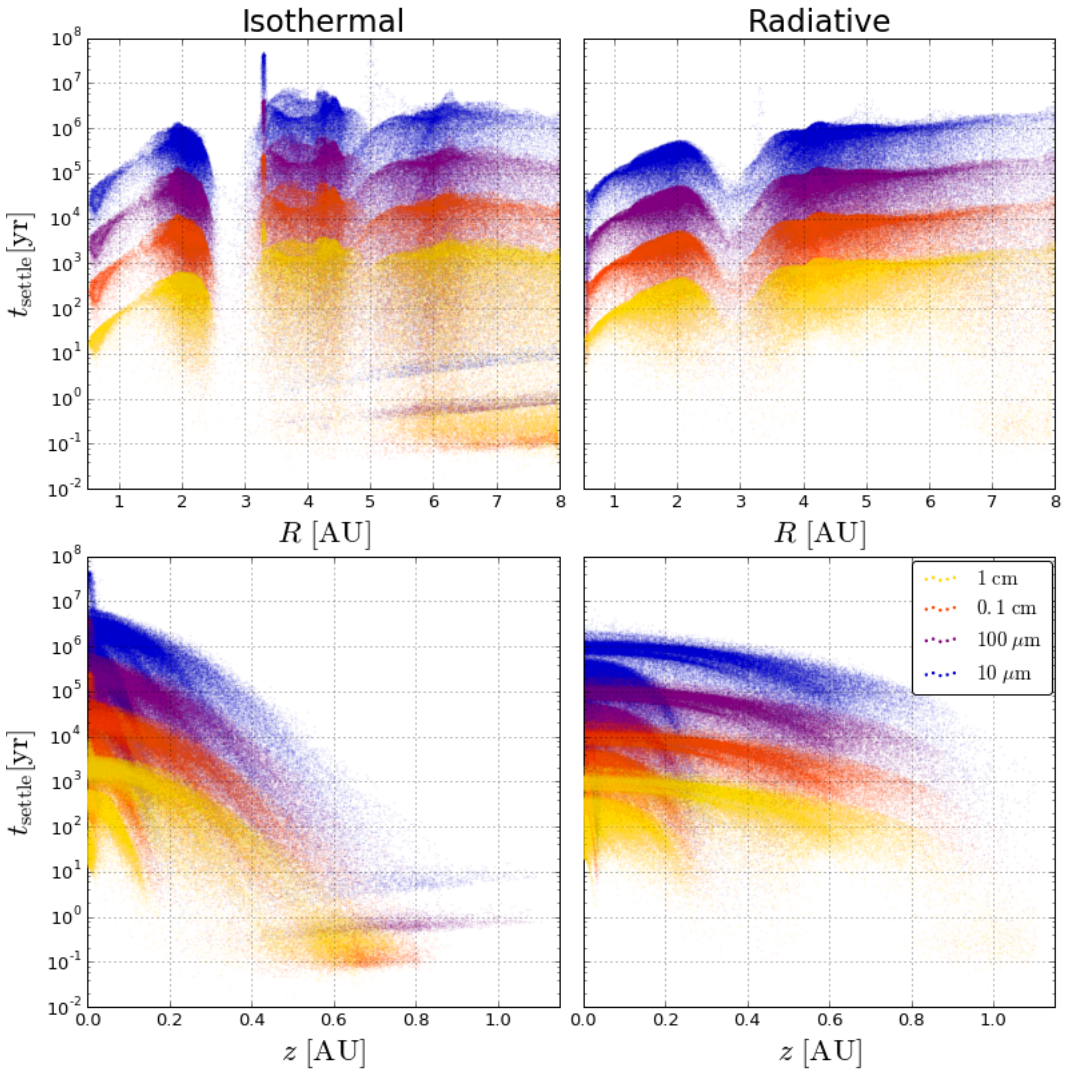

Figure 4.19: Theoretical settling times for particles with radii of $10\ \mu\mathrm{m}$, $100\ \mu\mathrm{m}$, $0.1\ \mathrm{cm}$ and $1\ \mathrm{cm}$ at $t = 600\ \mathrm{yr}$ as a function of R and z. *Left* panels: run A; *right* panels: run D.

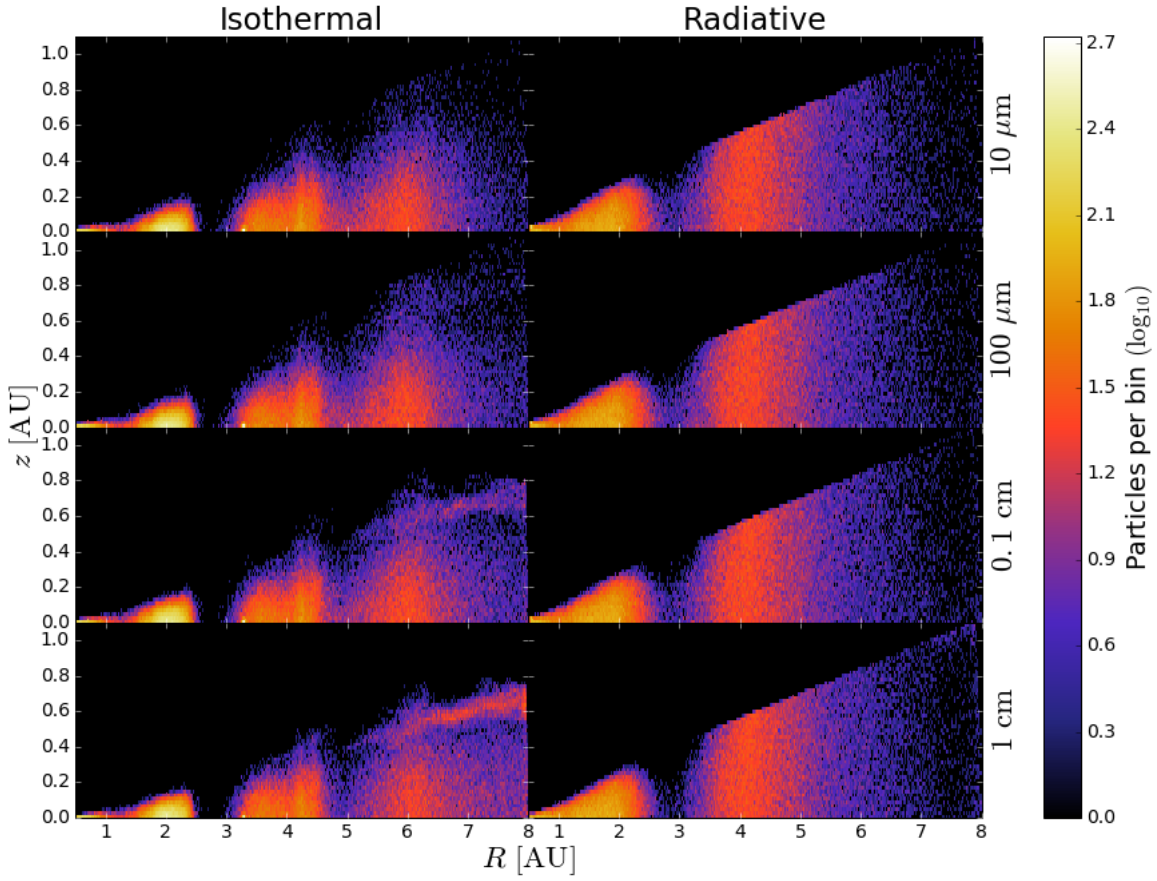

Figure 4.20: Vertical dust distribution of the dust particles after 600 years for the different grain sizes for the isothermal and radiative setups as a function of R and z. Each bin corresponds to 0.02 AU. From *Top* to *bottom*: particles with radii of 10 μm, 100 μm, 0.1 cm and 1 cm. *Left* panels: run A; *right* panels: run D.

Table 4.1: Number of 'captured' particles after 600 years, listed in radius-increasing order: 10 μm, 100 μm, 0.1 cm and 1 cm.

	Planet 1	*Planet 2*
Isothermal	1392	82
	1285	68
	1197	46
	894	26
Radiative	58	13
	50	19
	64	12
	37	13

treated as the restricted planar circular three-body problem described in Section 1.4.2. The main deviations are the presence of a second planet with non-negligible mass and the drag force exerted by the gas (see Ormel and Klahr 2010). In Figure 4.21 I show the dust distribution around the planets and highlight the particles inside their Hill sphere after 600 years for the isothermal and radiative runs (Table 4.1). The global trend suggests that smaller particles are more easily captured: this is in agreement with the fact that larger particles 'stream' more easily, being less coupled to the gas, thus moving at larger drift speed. Furthermore, the gas crossing the planet location supplies the Hill sphere with the particles which are most coupled to it.
This calculations only aim to give an idea of the relative abundance of captured particles as a function of the planet mass, the dust size and the choice of an isothermal or radiative setting, since it is a very rough estimate: the removal of particles after capture is not implemented in PLUTO, so an accurate approach should include the evaluation of the gravitational attraction by the planet compared to the drag (for smaller particles) or the kinetic energy (for larger particles), thus flagging the particles as accreted if they fulfill the criteria. However this was not possible with the time interval chosen between the outputs, since I would not have been able to oversee the required amount of time for a reliable estimate.

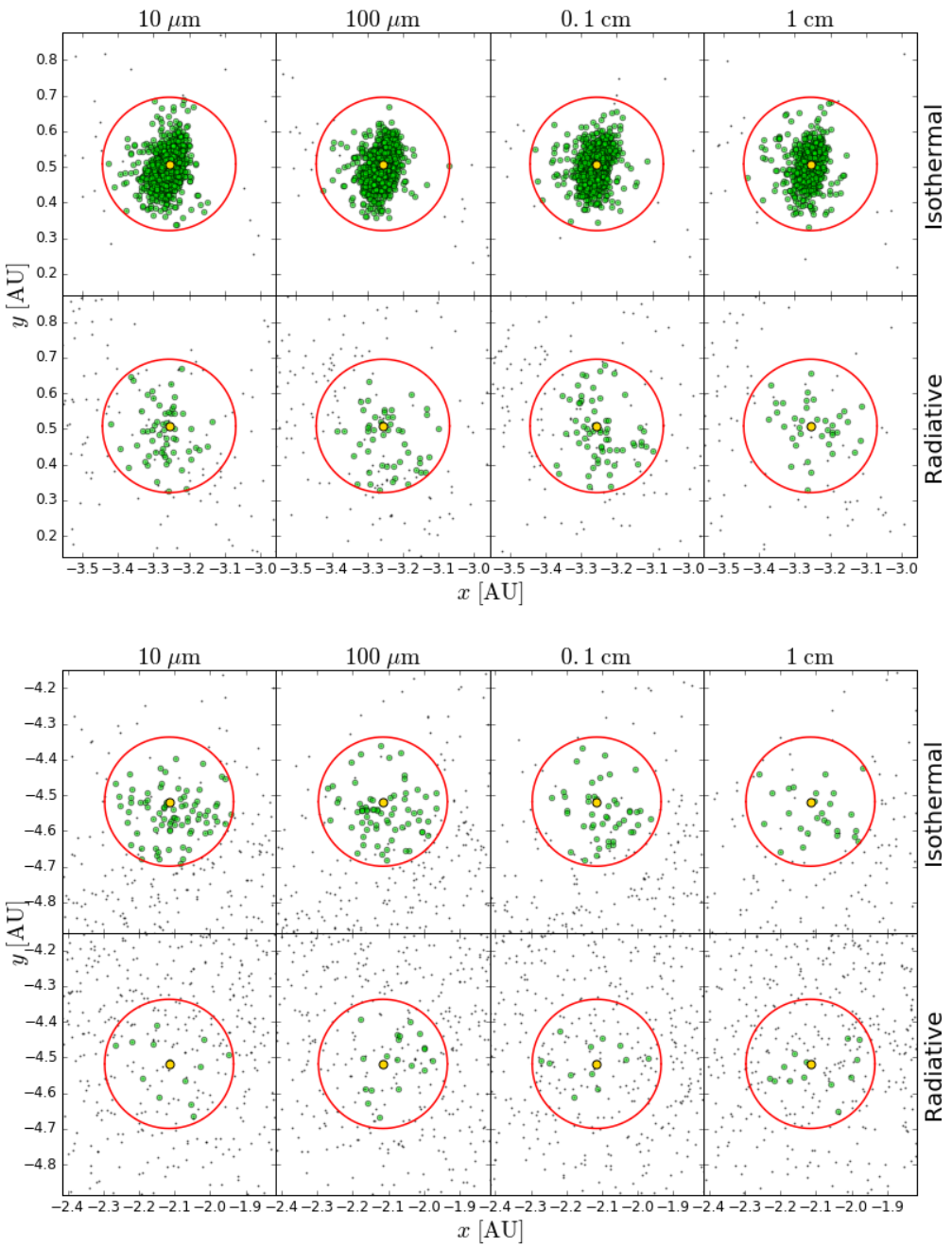

Figure 4.21: Zoom on the dust distribution on the $x - y$ plane in the proximity of the planets for the different grain sizes after 600 years for runs A and D. The planet is represented in yellow, the red circle indicates the volume delimited by the Hill sphere and the captured particles are plotted in green (if a particle is inside the circle but not colored, it means its z is too elevated to be part of the sphere). *Upper panels*: dust captured by planet 1 ($a = 3$ AU, $m = 0.001\,\mathrm{M}_\odot$, $R_{\mathrm{Hill},1} = 0.187$ AU). *Lower panels*: dust captured by planet 2 ($a = 4.76$ AU, $m = 0.000299\,\mathrm{M}_\odot$, $R_{\mathrm{Hill},2} = 0.181$ AU). From *left* to *right*: particles with radii of $10\ \mu$m, $100\ \mu$m, 0.1 cm and 1 cm.

5
Conclusions and Future Developments

5.1 Summary and Conclusions

During this thesis work I had the chance to study the early formation of gaps due to the presence of a couple of resonant planets, focusing on the dust distribution, in view of comparing my results to previous simulations, theory and observations. I performed four tridimensional hydrodynamic simulations characterised by different values of planet eccentricities, aspect ratio and equation of state, with the aim of looking for differences in their outcomes. Furthermore, I had the possibility to run one of the first radiative simulations including Lagrangian particles to mimic dust with PLUTO code, thus testing its effectiveness and validity.

The main conclusion I can infer is that the inclusion of radiation takes longer to put the disc into a stationary state, thus requiring more time to show characteristic features of PPDs like gaps and rings, as seen in ALMA and SPHERE observations: this must be taken into account when evaluating the constraints on the parameters describing the planets (e.g. mass and eccentricity) and the disc (e.g. scale height, viscosity and density profile). The results concerning the gas gap opening show good agreement with previous simulations (e.g. Varnière et al. 2004, Kanagawa et al. 2016) for the isothermal runs, while the radiative run shows features which better resemble an isothermal disc with greater aspect ratio: this is straightforward considering that scale height and thermal structure are strictly related due to the dependence of the sound speed on the temperature. Dust mostly follows the behaviour of the gas, since the two components are rather coupled: only bigger particles are slightly decoupled and would show noticeably different features given longer integration times, such as radial drift and vertical settling. Dust capture is more difficult in the radiative run, meaning further accretion by planets may be significantly slower without the isothermal approximation.

5.2 Comparison with Observations

A potential observational counterpart of my simulations can be found in the system HD 163296, detected by ALMA, which is thought to host two giant planets. Isella et al. 2016 studied both the distribution of dust and CO and identified two gaps at 100 AU and 160 AU around a $\sim$ 5 Myr old 2 $M_\odot$ star. Although these are unlikely to form a common gap due to their distance, the initial formation of gaps in my simulations resemble the one in Figure 5.1.

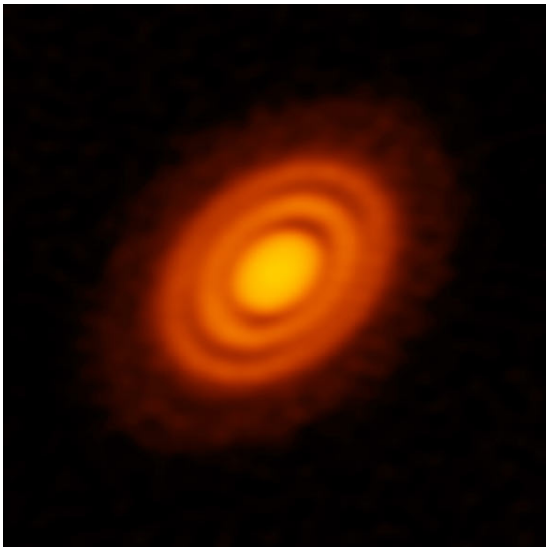

Figure 5.1: ALMA image of the protoplanetary disc surrounding the young star HD 163296 as seen in the dust continuum.

5.3 Future Developments

Future work include the extension in time and computational domain of these simulations, so that the formation of a common gap could actually be obtained. More parameters could be varied in order to have a larger set of simulations to compare, e.g. the α viscosity parameter, the surface density profile, the masses of the planets and the order of the resonance.

The main inaccuracy in my simulations was the choice of fixed orbits, which prevent the conservation of linear and angular momentum and do not include interaction with the gas component, the planets' mutual interaction nor migration: this was reasonable for such short timescales, but variations in the orbital parameters need to be considered for reliable results after $10^4 - 10^5$ years. A new module by Thun and Kley 2018 which allows to integrate planetary orbits has been recently implemented for PLUTO: I will soon be able to relaunch my simulations with this adaptation.

In order to have a solid comparison with observations, it is necessary to continue my work using a radiative transfer code, which allows to convert simulated values of density, temperature and opacity into column density and eventually flux. For instance, with a code like RADMC-3D developed by Dullemond et al. 2012 I would be able to compare synthetic observations of dusty PPDs to ALMA and SPHERE observations.

Furthermore, comparisons with SPH [*] codes, e.g. PHANTOM (Price et al. 2017), would show the advantages or limits of a grid code like PLUTO to model non-axisymmetric structures in PPDs.

[*] Smoothed-Particle Hydrodynamics

A
Hamiltonian Formulation

The following analysis is taken from Murray and Dermott 2000 and Malhotra 2012.

A.1 Two-Body Problem

This different mathematical approach is useful in the following discussion of the dynamics of resonance. We now use the variables

$$\mathrm{r} = r_x\mathrm{i} + r_y\mathrm{j} + r_z\mathrm{k} \text{ and } \mathrm{p} = p_x\mathrm{i} + p_y\mathrm{j} + p_z\mathrm{k}, \tag{A.1}$$

where r is the relative position vector and $\mathrm{p} = m_0m_1/(m_0 + m_1)\dot{\mathrm{r}}$ is the linear momentum of the system, i.e. the reference frame is centered in the center of mass, thus reducing the degrees of freedom from six to three.

We can write the vector equations of motion in the form

$$\dot{\mathrm{r}} = \nabla_{\mathrm{p}}\mathcal{H}_{\text{Kepler}} \text{ and } \dot{\mathrm{p}} = -\nabla_{\mathrm{r}}\mathcal{H}_{\text{Kepler}} \tag{A.2}$$

with

$$\nabla_{\mathrm{p}} = \mathrm{i}\frac{\partial}{\partial p_x} + \mathrm{j}\frac{\partial}{\partial p_y} + \mathrm{k}\frac{\partial}{\partial p_z}, \quad \nabla_{\mathrm{r}} = \mathrm{i}\frac{\partial}{\partial r_x} + \mathrm{j}\frac{\partial}{\partial r_y} + \mathrm{k}\frac{\partial}{\partial r_z} \tag{A.3}$$

and

$$\mathcal{H}_{\text{Kepler}} = \frac{p^2}{2\mu^*} - \frac{\mu\mu^*}{r} \tag{A.4}$$

is the *Hamiltonian* of the two-body problem, where $\mu^* = m_0m_1/(m_0 + m_1)$ is the *reduced mass* of the system. We now get

$$\begin{cases} \dot{\mathrm{r}} = \frac{\mathrm{p}}{\mu*} \\ \dot{\mathrm{p}} = -\frac{\mu\mu^*}{r^3}\mathrm{r} \end{cases} \tag{A.5}$$

where r and p form a conjugate set, while the orbital elements do not. So we need to find some functions of the orbital elements which can form conjugate sets.

Delaunay Variables

The three degrees of freedom can be described by three angular variables, one of which measures the motion of the planet in its elliptical orbit and the other two describe the orientation of the orbit in space. The orbital elements are related to the set of action-angle variables known as Delaunay variables: the coordinates and corresponding conjugate momenta are

$$\begin{cases} l = M \\ g = \omega \\ h = \Omega \end{cases} \qquad \begin{cases} L = \mu^* \sqrt{\mu a} \\ G = \mu^* \sqrt{\mu a(1-e^2)} \\ H = \mu^* \sqrt{\mu a(1-e^2)} \cos I \end{cases} \tag{A.6}$$

and the Hamiltonian is

$$\mathcal{H}_{\text{Kepler}} = -\frac{\mu^2 \mu^{*3}}{2L^2}. \tag{A.7}$$

Since $\mathcal{H}$ is only a function of L, g and h must be constants. The momenta are also constants since $L = L(a)$, G is the angular momentum and H is the vertical component of the angular momentum vector. The variation of l is:

$$\frac{\mathrm{d}l}{\mathrm{d}t} = \frac{\partial \mathcal{H}}{\partial L} = \frac{\mu^2 \mu^{*3}}{L^3} = \sqrt{\frac{\mu}{a^3}}. \tag{A.8}$$

Poincaré Variables

For the case of nearly co-planar and nearly circular orbits the Delaunay variables can be conveniently modified to obtain the Poincaré variables: the coordinates and corresponding conjugate momenta are

$$\begin{cases} \lambda = M + \omega + \Omega \\ \gamma = -\omega - \Omega \\ z = -\Omega \end{cases} \qquad \begin{cases} \Lambda = \mu^* \sqrt{\mu a} \\ \Gamma = \mu^* \sqrt{\mu a}(1 - \sqrt{1-e^2}) \\ Z = \mu^* \sqrt{\mu a(1-e^2)}(1 - \cos I) \end{cases} \tag{A.9}$$

and the Hamiltonian is

$$\mathcal{H}_{\text{Kepler}} = -\frac{\mu^2 \mu^{*3}}{2\Lambda^2}. \tag{A.10}$$

The following relationship holds between the two sets:

$$\Lambda\lambda + \Gamma\gamma + Zz = Ll + Gg + Hh \tag{A.11}$$

which is a *contact transformation*, i.e. it preserves the canonical nature of the equations and does not change the Hamiltonian.

A.2 N-Body Systems

For multiple planets around a star, the system can be described as a sum of two-body Keplerian Hamiltonians plus the potential energy of the planet-planet interactions. To do so, we must renounce the astrocentric approach and adopt a coordinate system in which we first use the coordinates of the centre of mass and then, successively, the coordinates of the first planet relative to the star, the coordinates of the second planet relative to the centre of mass of the star and the first planet, and so on. For a system of N planets orbiting a star, $\mathbf{r}_i (i = 0, 1, ..., N)$ denote the coordinates of the star and the N planets in an inertial reference frame and we define

$$\widetilde{\mathbf{r}}_0 = \frac{\sum_{j=0}^{N} m_j \mathbf{r}_j}{\sum_{j=0}^{N} m_j}, \quad \widetilde{\mathbf{r}}_i = \mathbf{r}_i - \mathbf{R}_{i-1}, \quad \text{with} \quad \mathbf{R}_i = \frac{\sum_{j=0}^{i} m_j \mathbf{r}_j}{\sum_{j=0}^{i} m_j} \tag{A.12}$$

and

$$\widetilde{\mathbf{p}}_i = \widetilde{m}_i \dot{\widetilde{\mathbf{r}}}_i, \quad \text{with} \quad \widetilde{m}_i = \frac{m_i \sum_{j=0}^{i-1} m_j}{\sum_{j=0}^{i} m_j}. \tag{A.13}$$

The final Hamiltonian is given by

$$\mathcal{H} = \sum_{i=1}^{N} \left[\frac{\widetilde{p}_i^2}{2\widetilde{m}_i} - \frac{G m_0 m_i}{\widetilde{r}_i} \right] - \sum_{0<i<j} \frac{G m_i m_j}{r_{ij}} + \sum_{i}^{N} \left[\frac{G m_0 m_i}{\widetilde{r}_i} - \frac{G m_0 m_i}{r_{i0}} \right] = \sum_{i=1}^{N} \mathcal{H}_{\text{Kepler}}^{(i)} + \mathcal{H}_{\text{interaction}}. \tag{A.14}$$

The Delaunay variables are no longer action-angle variables, but they provide a useful canonical set.

A.3 Mean Motion Resonance

The simplest case of a mean motion resonance can be studied considering the planar circular restricted three-body problem in which a single planet m_p orbits a star m_* in a circular orbit and a test particle m orbits the star with an orbital period close to a ratio of small integers with respect to the planet. In terms of the Poincaré variables:

$$\mathcal{H}(\lambda, \gamma, \Lambda, \Gamma, t) = -\frac{(G m_*)^2}{2\Lambda^2} + \mathcal{H}_\mathrm{p}. \tag{A.15}$$

Let us consider a first order mean motion resonance, i.e. $q = 1$. In order to reach a useful form of the Hamiltonian we must perform a series of changes in coordinates:

$$\begin{cases} \phi = (p+1)\lambda_\mathrm{p} - p\lambda + \gamma \\ \psi = \lambda - \lambda_\mathrm{p} \end{cases} \quad \begin{cases} \Phi = \Gamma \\ \Psi = \Lambda + p\Gamma \end{cases} \tag{A.16}$$

Close to the resonance, ψ is a fast variable so we can neglect the ψ-dependent terms and Ψ becomes a constant of the motion. We define

$$n_* = \frac{(Gm_*)^2}{\Psi^3}, \quad a_* = \frac{\Psi^2}{Gm_*} \tag{A.17}$$

which are the osculating mean motion and semi-mejor axis of the test particle when its eccentricity is zero and are constants of motion as well. We define

$$\beta = -\frac{3p^2 n_*}{2\Psi}, \quad \epsilon = -\frac{Gm_\mathrm{p}}{a_\mathrm{p}} \frac{f_\mathrm{p}}{\sqrt{\Psi}} \tag{A.18}$$

where f_p is a coefficient. Finally, we define a dimensionless canonical momentum R and a modified canonical coordinate θ as

$$R = \left| \frac{2\beta}{\epsilon} \right|^{2/3} \Phi, \quad \theta = \begin{cases} -\phi & \text{if } \epsilon > 0 \\ \pi - \phi & \text{if } \epsilon > 0. \end{cases} \tag{A.19}$$

The dimensionless Hamiltonian in the canonical variables (θ, R) is then given by

$$K = -3\Delta R + R^2 - 2\sqrt{2R}\cos\theta \tag{A.20}$$

where the dimensionless parameter Δ is a measure of the closeness to the exact resonance,

$$\Delta = \frac{(p+1)n_\mathrm{p} - pn_*}{s_\nu} \tag{A.21}$$

where n_* is the unperturbed mean motion and s_ν is a frequency scale equal to

$$s_\nu = \left| \frac{27\beta\epsilon^2}{4} \right|^{1/3}. \tag{A.22}$$

References

ALMA Partnership. The 2014 alma long baseline campaign: First results from high angular resolution observations toward the hl tau region. *The Astrophysical Journal Letters*, 808(1):L3, 2015.

Anders E. and Grevesse N. Abundances of the elements: Meteoric and solar. *Geochim.\ Cosmochim.\ Acta*, 53:197–214, 1989. ISSN 0016-7037.

Andrews S. M., Wilner D. J., Zhu Z., Birnstiel T., Carpenter J. M., Pérez L. M., Bai X.-N., Öberg K. I., Hughes A. M., Isella A., and Ricci L. Ringed Substructure and a Gap at 1 au in the Nearest Protoplanetary Disk. *The Astrophysical Journal Letters*, 820:L40, April 2016. doi: 10.3847/2041-8205/820/2/L40.

Armitage P. J. *Astrophysics of planet formation*. 2009. ISBN 9780511802225. doi: 10.1017/CBO9780511802225.

Armitage P. J. Physical processes in protoplanetary disks. 2015. ISSN 2045-2322. doi: 10.1038/srep13253.

Armitage P. J. and Rice W. K. Planetary migration. *A Decade of Extrasolar Planets around Normal Stars: Proceedings of the Space Telescope Science Institute Symposium, Held in Baltimore, Maryland May 2-5, 2005*, 9780521897846:66–83, 2005. doi: 10.1017/CBO9780511536304.008.

Bai X. N. and Stone J. M. Particle-gas Dynamics with Athena: Method and Convergence. *The Astrophysical Journal*, 190:297–310, October 2010. doi: 10.1088/0067-0049/190/2/297.

Balbus S. A. and Hawley J. F. A powerful local shear instability in weakly magnetized disks. I - Linear analysis. II - Nonlinear evolution. *The Astrophysical Journal*, 376:214–233, July 1991. doi: 10.1086/170270.

Birnstiel T., Dullemond C. P., and Brauer F. Dust retention in protoplanetary disks. *Astronomy & Astrophysics*, 503(1): L5–L8, 2009. ISSN 0004-6361. doi: 10.1051/0004-6361/200912452.

Birnstiel T., Klahr H., and Ercolano B. A simple model for the evolution of the dust population in protoplanetary disks. 148, 2012. ISSN 0004-6361. doi: 10.1051/0004-6361/201118136.

Birnstiel T., Fang M., and Johansen A. Dust Evolution and the Formation of Planetesimals. *Space Science Reviews*, 205 (1-4):41–75, 2016. ISSN 15729672. doi: 10.1007/s11214-016-0256-1.

Carrera D., Gorti U., Johansen A., and Davies M. B. Planetesimal formation by the streaming instability in a photoevaporating disk. *The Astrophysical Journal*, 839(1):16, 2017.

Chapman S. and Cowling T. G. *The mathematical theory of non-uniform gases. an account of the kinetic theory of viscosity, thermal conduction and diffusion in gases*. 1970.

Charpinet S., Fontaine G., Brassard P., Green E. M., Van Grootel V., Randall S. K., Silvotti R., Baran A. S., Østensen R. H., Kawaler S. D., and Telting J. H. A compact system of small planets around a former red-giant star. *Nature*, 480: 496–499, December 2011. doi: 10.1038/nature10631.

Chokshi A., Tielens A. G. G. M., and Hollenbach D. Dust coagulation. *The Astrophysical Journal*, 407:806–819, April 1993. doi: 10.1086/172562.

Cieza L. A., Casassus S., Tobin J., Bos S. P., Williams J. P., Perez S., Zhu Z., Caceres C., Canovas H., Dunham M. M., Hales A., Prieto J. L., Principe D. A., Schreiber M. R., Ruiz-Rodriguez D., and Zurlo A. Imaging the water snow-line during a protostellar outburst. *Nature*, 535:258–261, July 2016. doi: 10.1038/nature18612.

Courant R., Friedrichs K., and Lewy H. Über die partiellen Differenzengleichungen der mathematischen Physik. *Mathematische Annalen*, 100:32–74, 1928. doi: 10.1007/BF01448839.

D'Angelo G. and Marzari F. Outward migration of Jupiter and Saturn in evolved gaseous disks. *Astrophysical Journal*, 757(1), 2012. ISSN 15384357. doi: 10.1088/0004-637X/757/1/50.

Dipierro G., Price D., Laibe G., Hirsh K., Cerioli A., and Lodato G. On planet formation in HL Tau 1. 77(July):1–5, 2015. doi: 10.1093/mnrasl/slv105.

Duffell P. C. and MacFadyen A. I. Gap opening by extremely low-mass planets in a viscous disk. *Astrophysical Journal*, 769(1), 2013. ISSN 15384357. doi: 10.1088/0004-637X/769/1/41.

Dullemond C. P., Juhasz A., Pohl A., Sereshti F., Shetty R., Peters T., Commercon B., and Flock M. RADMC-3D: A multi-purpose radiative transfer tool. Astrophysics Source Code Library, February 2012.

Fouchet L., Gonzalez J.-F., and Maddison S. T. Planet gaps in the dust layer of 3D protoplanetary disks. I. Hydrodynamical simulations of T Tauri disks. *Astronomy & Astrophysics*, 518:A16, July 2010. doi: 10.1051/0004-6361/200913778.

Frank J. Accretion Power in Astrophysics, 1986. ISSN 00319228.

Garufi A., Benisty M., Stolker T., Pohl A., Quanz S. P., Dominik C., Ginski C., Thalmann C., Boekel R. V., Salter G., Sissa E., Menard F., and Milli J. Three Years of SPHERE : The Latest View of the Morphology and Evolution of Protoplanetary Discs. (September):32–37, 2017. doi: 10.18727/0722-6691/5036.

Goldreich P. and Ward W. R. The Formation of Planetesimals. *The Astrophysical Journal*, 183:1051–1062, August 1973. doi: 10.1086/152291.

Harten A., Lax P. D., and Van Leer B. On Upstream Differencing and Godunov-Type Schemes for Hyperbolic Conservation Laws. *SIAM Review*, 25:35–61, 1983. doi: 110.1137/1025002.

Helling C., Winters J. M., and Sedlmayr E. Circumstellar dust shells around long-period variables. VII. The role of molecular opacities. *Astronomy & Astrophysics*, 358:651–664, June 2000.

Henning T. and Stognienko R. Dust opacities for protoplanetary accretion disks: influence of dust aggregates. *Astronomy & Astrophysics*, 311:291–303, July 1996.

Isella A., Guidi G., Testi L., Liu S., Li H., Li S., Weaver E., Boehler Y., Carperter J., De Gregorio-Monsalvo I., Manara C. F., Natta A., Pérez L. M., Ricci L., Sargent A., Tazzari M., and Turner N. Ringed Structures of the HD 163296 Protoplanetary Disk Revealed by ALMA. *Physical Review Letters*, 117(25):1–8, 2016. ISSN 10797114. doi: 10.1103/PhysRevLett.117.251101.

Johansen A., Oishi J. S., Low M. M. M., Klahr H., Henning T., and Youdin A. Rapid planetesimal formation in turbulent circumstellar disks. *Nature*, 448(7157):1022–1025, 2007. ISSN 14764687. doi: 10.1038/nature06086.

Kanagawa K. D., Muto T., Tanaka H., Tanigawa T., Takeuchi T., Tsukagoshi T., and Momose M. Mass constraint for a planet in a protoplanetary disk from the gap width. *Publications of the Astronomical Society of Japan*, 68(3):1–7, 2016. ISSN 2053051X. doi: 10.1093/pasj/psw037.

Kataoka A., Tsukagoshi T., Momose M., Nagai H., Muto T., Dullemond C. P., Pohl A., Fukagawa M., Shibai H., Hanawa T., and Murakawa K. Submillimeter Polarization Observation of the Protoplanetary Disk around HD 142527. *Astrophysical Journal Letters*, 831:L12, November 2016. doi: 10.3847/2041-8205/831/2/L12.

Klahr H. and Kley W. 3D-radiation hydro simulations of disk-planet interactions. *Astronomy & Astrophysics*, 445(2): 747–758, 2006. ISSN 0004-6361. doi: 10.1051/0004-6361:20053238.

Kley W., Bitsch B., and Klahr H. Planet migration in three-dimensional radiative discs. *The Astrophysical Journal*, 506: 971–987, November 2009. doi: 10.1051/0004-6361/200912072.

Kolb S. M., Stute M., Kley W., and Mignone A. Radiation hydrodynamics integrated in the code PLUTO. 80:1–12, 2013. doi: 10.1051/0004-6361/201321499.

Korycansky D. G. and Pollack J. B. Numerical calculations of the linear response of a gaseous disk to a protoplanet. *Icarus*, 102:150–165, March 1993. doi: 10.1006/icar.1993.1039.

Larson R. B. Turbulence and star formation in molecular clouds. *Monthly Notices of the Royal Astronomical Society*, 194:809–826, March 1981. doi: 10.1093/mnras/194.4.809.

Malhotra R. Orbital resonances in planetary systems. *Encyclopedia of Life Support Systems - Celestial Mechanics*, 6 (September 2012):31, 2012.

Marzari F., Baruteau C., Scholl H., and Thebault P. Eccentricity of radiative disks in close binary-star systems. *Astronomy & Astrophysics*, 539:A98, 2012. ISSN 0004-6361. doi: 10.1051/0004-6361/201118075.

Marzari F., Picogna G., and D'Angelo G. Circumstellar dust distribution in systems with two planets in resonance. *The Astrophysical Journal*, 2018. [submitted].

Masset F. and Snellgrove M. Reversing type II migration: Resonance trapping of a lighter giant protoplanet. *Monthly Notices of the Royal Astronomical Society*, 320(4):0–4, 2001. ISSN 0035871l. doi: 10.1046/j.1365-8711.2001.04159.x.

Masset F. S. and Papaloizou J. C. B. Runaway Migration and the Formation of Hot Jupiters. *The Astrophysical Journal*, 588:494–508, May 2003. doi: 10.1086/373892.

Mathis J. S., Rumpl W., and Nordsieck K. H. The size distribution of interstellar grains. *The Astrophysical Journal*, pages 425–433, 1977.

Mayor M. and Queloz D. A Jupiter-mass companion to a solar-type star. *Nature*, 378:355–359, November 1995. doi: 10.1038/378355a0.

Mignone A. High-order conservative reconstruction schemes for finite volume methods in cylindrical and spherical coordinates. *Journal of Computational Physics*, 270:784–814, August 2014. doi: 10.1016/j.jcp.2014.04.001.

Mignone A., Bodo G., Massaglia S., Matsakos T., Tesileanu O., Zanni C., and Ferrari A. PLUTO: a Numerical Code for Computational Astrophysics. pages 1–37, 2007. ISSN 0067-0049. doi: 10.1086/513316.

Murray C. D. and Dermott S. F. *Solar System Dynamics*. February 2000.

Nakagawa Y., Sekiya M., and Hayashi C. Settling and growth of dust particles in a laminar phase of a low-mass solar nebula. *Icarus*, 67:375–390, September 1986. doi: 10.1016/0019-1035(86)90121-1.

Nelson R. P., Gressel O., and Umurhan O. M. Linear and non-linear evolution of the vertical shear instability in accretion discs. *Monthly Notices of the Royal Astronomical Society*, 435(3):2610–2632, 2013. ISSN 0035871l. doi: 10.1093/mnras/stt1475.

Ormel C. W. and Klahr H. H. The effect of gas drag on the growth of protoplanets – Analytical expressions for the accretion of small bodies in laminar disks. (14903), 2010. ISSN 1432-0746. doi: 10.1051/0004-6361/201014903.

Paardekooper S.-J. and Mellema G. Planets opening dust gaps in gas disks. *Astronomy & Astrophysics*, 425:L9–L12, October 2004. doi: 10.1051/0004-6361:200400053.

Pérez L. M., Carpenter J. M., Andrews S. M., Ricci L., Isella A., Linz H., Sargent A. I., Wilner D. J., Henning T., Deller A. T., Chandler C. J., Dullemond C. P., Lazio J., Menten K. M., Corder S. A., Storm S., Testi L., Tazzari M., Kwon W., Calvet N., Greaves J. S., Harris R. J., and Mundy L. G. Spiral density waves in a young protoplanetary disk. *Science*, 353: 1519–1521, September 2016. doi: 10.1126/science.aaf8296.

Picogna G. and Kley W. How do giant planetary cores shape the dust disk? HL Tauri system. *Astronomy & Astrophysics*, 584(February):A110, 2015. ISSN 0004-6361. doi: 10.1051/0004-6361/201526921.

Picogna G., Stoll M. H. R., and Kley W. Particle accretion onto planets in discs with hydrodynamic turbulence. 2018.

Pollack J. B., Hollenbach D., Beckwith S., Simonelli D. P., Roush T., and Fong W. Composition and radiative properties of grains in molecular clouds and accretion disks. *The Astrophysical Journal*, 421:615–639, February 1994. doi: 10.1086/173677.

Price D. J., Wurster J., Tricco T. S., Nixon C., Toupin S., Pettitt A., Chan C., Mentiplay D., Laibe G., Glover S., Dobbs C., Nealon R., Liptai D., Worpel H., Bonnerot C., Dipierro G., Ballabio G., Ragusa E., Federrath C., Iaconi R., Reichardt T., Forgan D., Hutchison M., Constantino T., Ayliffe B., Hirsh K., and Lodato G. Phantom: A smoothed particle hydrodynamics and magnetohydrodynamics code for astrophysics. *ArXiv e-prints*, February 2017.

Pringle J. E. Accretion discs in astrophysics. *Annual Review of Astronomy and Astrophysics*, 19:137–162, 1981. doi: 10.1146/annurev.aa.19.090181.001033.

Pringle J. E. and King A. R. *Astrophysical flows*. 2007.

Qi C., Öberg K. I., Andrews S. M., Wilner D. J., Bergin E. A., Hughes A. M., Hogherheijde M., and D'Alessio P. CHEMICAL IMAGING of the CO SNOW LINE in the HD 163296 DISK. *Astrophysical Journal*, 813(2):1–17, 2015. ISSN 15384357. doi: 10.1088/0004-637X/813/2/128.

Rein H., Papaloizou J. C. B., and Kley W. The dynamical origin of the multi-planetary system HD 45364. *The Astrophysical Journal*, 510:A4, January 2010. doi: 10.1051/0004-6361/200913208.

Safronov V. S. and Zvjagina E. V. Relative Sizes of the Largest Bodies during the Accumulation of Planets. *Icarus*, 10: 109–115, January 1969. doi: 10.1016/0019-1035(69)90013-X.

Semenov D., Henning T., Helling C., Ilgner M., and Sedlmayr E. Rosseland and Planck mean opacities for protoplanetary discs. *Astronomy & Astrophysics*, 410(2):611–621, 2003. ISSN 0004-6361. doi: 10.1051/0004-6361:20031279.

Semenov D., Favre C., Fedele D., Guilloteau S., Teague R., Henning T., Dutrey A., Chapillon E., Hersant F., and Piétu V. Chemistry in disks. XI. Sulfur-bearing species as tracers of protoplanetary disk physics and chemistry: the DM Tau case. *ArXiv e-prints*, June 2018.

Shakura N. I. and Sunyaev R. A. Black holes in binary systems. Observational appearance. *Astronomy & Astrophysics*, 24:337–355, 1973.

Stolker T., Dominik C., Avenhaus H., Min M., de Boer J., Ginski C., Schmid H. M., Juhasz A., Bazzon A., Waters L. B. F. M., Garufi A., Augereau J.-C., Benisty M., Boccaletti A., Henning T., Langlois M., Maire A.-L., Ménard F., Meyer M. R., Pinte C., Quanz S. P., Thalmann C., Beuzit J.-L., Carbillet M., Costille A., Dohlen K., Feldt M., Gisler D., Mouillet D., Pavlov A., Perret D., Petit C., Pragt J., Rochat S., Roelfsema R., Salasnich B., Soenke C., and Wildi F. Shadows cast on the transition disk of HD 135344B. Multiwavelength VLT/SPHERE polarimetric differential imaging. *The Astrophysical Journal*, 595:A113, November 2016. doi: 10.1051/0004-6361/201528039.

Stoll M. H. R., Picogna G., and Kley W. Anisotropic hydrodynamic turbulence in accretion disks. (1):1–5, 2017. ISSN 0004-6361. doi: 10.1051/0004-6361/201630226.

Stoll M. H. R. and Kley W. Vertical shear instability in accretion disc models with radiation transport. pages 1–12, 2014. ISSN 0004-6361. doi: 10.1051/0004-6361/201424114.

Syer D. and Clarke C. J. Satellites in discs: regulating the accretion luminosity. *Monthly Notices of the Royal Astronomical Society*, 277:758–766, December 1995. doi: 10.1093/mnras/277.3.758.

Takeuchi T. and Lin D. N. C. Radial Flow of Dust Particles in Accretion Disks. (1976), 2002. ISSN 0004-637X. doi: 10.1086/344437.

Tanaka H., Takeuchi T., and Ward W. R. Three-Dimensional Interaction between a Planet and an Isothermal Gaseous Disk. I. Corotation and Lindblad Torques and Planet Migration. *The Astrophysical Journal*, 565:1257–1274, February 2002. doi: 10.1086/324713.

Thun D. and Kley W. Migration of planets in circumbinary discs. *The Astrophysical Journal*, 616:A47, August 2018. doi: 10.1051/0004-6361/201832804.

Tisserand F. *Traité de mécanique céleste*. Number v. 4 in Traité de mécanique céleste. Gauthier-Villars, 1896.

Toomre A. On the gravitational stability of a disk of stars. *The Astrophysical Journal*, 139:1217–1238, May 1964. doi: 10.1086/147861.

Toro E. F., Spruce M., and Speares W. Restoration of the contact surface in the HLL-Riemann solver. *Shock Waves*, 4 (1):25–34, 1994. ISSN 09381287. doi: 10.1007/BF01414629.

Van Boekel R., Henning T., Menu J., de Boer J., Langlois M., Müller A., Avenhaus H., Boccaletti A., Schmid H. M., Thalmann C., Benisty M., Dominik C., Ginski C., Girard J. H., Gisler D., Lobo Gomes A., Menard F., Min M., Pavlov A., Pohl A., Quanz S. P., Rabou P., Roelfsema R., Sauvage J.-F., Teague R., Wildi F., and Zurlo A. Three Radial Gaps in the Disk of TW Hydrae Imaged with SPHERE. *The Astrophysical Journal*, 837:132, March 2017. doi: 10.3847/1538-4357/aa5d68.

Van der Marel N., Cazzoletti P., Pinilla P., and Garufi A. Vortices and Spirals in the HD135344B Transition Disk. *The Astrophysical Journal*, 832:178, December 2016. doi: 10.3847/0004-637X/832/2/178.

Varnière P., Quillen A. C., and Frank A. The Evolution of Protoplanetary Disk Edges. *The Astrophysical Journal*, 612: 1152–1162, September 2004. doi: 10.1086/422542.

Walsh K. J., Morbidelli A., Raymond S. N., O'Brien D. P., and Mandell A. M. A low mass for Mars from Jupiter's early gas-driven migration. *Nature*, 475(7355):206–209, 2011. ISSN 00280836. doi: 10.1038/nature10201.

Weidenschilling S. J. Aerodynamics of solid bodies in the solar nebula. *Monthly Notices of the Royal Astronomical Society*, 180:57–70, July 1977. doi: 10.1093/mnras/180.1.57.

Weidenschilling S. J. Dust to planetesimals - Settling and coagulation in the solar nebula. *Icarus*, 44:172–189, October 1980. doi: 10.1016/0019-1035(80)90064-0.

Windmark F., Birnstiel T., Ormel C. W., and Dullemond C. P. Breaking through: The effects of a velocity distribution on barriers to dust growth. *The Astrophysical Journal*, 544:L16, August 2012. doi: 10.1051/0004-6361/201220004.

Woitke P. and Helling C. Dust in brown dwarfs. II. The coupled problem of dust formation and sedimentation. *The Astrophysical Journal*, 399:297–313, February 2003. doi: 10.1051/0004-6361:20021734.

Wright J. T., Fakhouri O., Marcy G. W., Han E., Feng Y., Johnson J. A., Howard A. W., Fischer D. A., Valenti J. A., Anderson J., and Piskunov N. The Exoplanet Orbit Database. *Publications of the Astronomical Society of the Pacific*, 123:412, April 2011. doi: 10.1086/659427.

Yang C., Johansen A., and Carrera D. Concentrating small particles in protoplanetary disks through the streaming instability. 3:1–16, 2016. ISSN 0004-6361. doi: 10.1051/0004-6361/201630106.

Youdin A. N. and Goodman J. Streaming Instabilities in Protoplanetary Disks. *The Astrophysical Journal*, 620(1): 459–469, 2005. ISSN 0004-637X. doi: 10.1086/426895.

Youdin A. N. and Lithwick Y. Particle stirring in turbulent gas disks: Including orbital oscillations. *Icarus*, 192(2): 588–604, 2007. ISSN 00191035. doi: 10.1016/j.icarus.2007.07.012.

Youdin A. N. and Shu F. H. Planetesimal Formation by Gravitational Instability. *The Astrophysical Journal*, 580: 494–505, November 2002. doi: 10.1086/343109.

Zhu Z., Stone J. M., Rafikov R. R., and Bai X.-n. Particle Concentration at Planet-induced Gap Edges and Vortices. I. Inviscid Three-dimensional Hydro Disks. *The Astrophysical Journal*, 785:122, April 2014. doi: 10.1088/0004-637X/785/2/122.